SPECTROSCOPIC AND NONLINEAR OPTICAL CHARACTERISATION OF ALPHA SUBSTITUTED BINUCLEAR PHTHALOCYANINES

A thesis submitted in fulfilment of the requirement for the degree of

MASTER OF SCIENCE

of

RHODES UNIVERSITY

by

GRACE NOMTHANDAZO NGUBENI

February 2016

DEDICATION TO

Abba Father

My Extraordinary Parents

Vusumuzi Philemon Ngubeni

&

Goodness Thokozile Ngubeni

My Siblings

Busisiwe Huma & Ngoako Huma

(Zoe & Zion)

Nkosinathi Peter Ngubeni & Charlotte Ngubeni

(Thando & Musa)

Thokozani Ngubeni and Lerato Ngubeni

Joy Simphiwe Ngubeni

Ngiyabonga maNkomo amahle ☺

ACKNOWLEDGEMENTS

I would like to acknowledge God the Father, God the Son & God the Holy Spirit for carrying and guiding me through. Ebenezer ~ thus far the Lord has helped me.

To Dr S. Khene, it has been a great journey studying under your supervision over years. The wealth of knowledge you have imparted to me is truly priceless. Thank you for introducing me to the adventures of research and believing in me.

To lab S26 (where my journey began), F2 and F3, thank you for being like a family always there to listen, assist and share in the highs and lows research. Your contribution towards my life has been amazing. To Dr J. Britton and Dr J. Mack thank you for assisting and contributing towards my research, I really appreciate it. To the Rhodes Volleyballers 2014/2015, thank you all for the friendship/sportsmanship shared. To the culprits, the time spent with you all has been memorable.

To the Ngubeni/Huma families, thank you for being my pillars of strength. For your constant encouragement and support in many ways imaginable. I count myself blessed to be part of such an incredible and God-fearing family. To my family and friends at large (from all nations), thank you for cheering me on and being part of the journey. Words cannot begin to express my gratitude towards you all.

I would like to thank PPS, TATA Africa (Women in Science Awards) and the National Research Fund (NRF) for their financial support during my postgraduate studies. Thank you for investing in me. Lastly, to all the pursuers of knowledge, let us continue pursuing knowledge and pass on the baton to the next generation of thinkers. It can only get better when great minds unite for a better tomorrow.

*"**Isaiah 40:31** – but those who hope in the Lord will renew their strength. They will soar on wings like eagles; they will run and not grow weary, they will walk and not be faint."*

ABSTRACT

In a world that is fast moving towards the extensive use of modern technology, the need to develop material that will satisfy the demands of modern technologies such as in communication and protection of optical sensors is essential.

The spectroscopic and nonlinear optical properties of the positional isomers of metal free 4α-(4-*tert*-butylphenoxy) phthalocyanine are presented in this thesis. Second order nonlinear polarizability (β), imaginary hyperpolarizability (Im(γ)) and imaginary susceptibility (Im[$\chi^{(3)}$]) values were determined for the four positional isomers. The measured β values of the four isomers displayed the following trend, C_{4h} ($34.0 \times 10^{-5}\, m\, MW^{-1}$) > D_{2h} ($28.8 \times 10^{-5}\, m\, MW^{-1}$) > C_{2v} ($22.8 \times 10^{-5}\, m\, MW^{-1}$) > C_s ($13.7 \times 10^{-5}\, m\, MW^{-1}$).

This thesis also reports the *z*-scan technique employed to comparatively study the second order nonlinear optical (NLO) properties of alpha substituted nickel and metal free 4-*tert*-butylphenoxy binuclear phthalocyanine namely, biphenyl bridged bis-4-*tert*-butylphenoxy phthalocyanine and naphthalene bridged bis-4-*tert*-butylphenoxy phthalocyanine. This work shows that the presence of H-aggregation in binuclear phthalocyanines of metal free and nickel bis-4-*tert*-butylphenoxy phthalocyanine does not have a significant effect on second order nonlinear absorption coefficient ($\boldsymbol{\beta}$) as compared to monomeric Pcs. Density functional theory (DFT) calculations of dipolar/octupolar contribution were performed, in order to explain experimentally determined $\boldsymbol{\beta}$ values. Spectroscopic and photophysical properties of the synthesised compounds have been determined using a range of different spectroscopic techniques, including magnetic circular dichroism (MCD), time correlated single photon count (TCSPC) and ultraviolet visible (UV/vis) absorption spectroscopy.

The main focus of this thesis is to study the properties of phthalocyanine and binuclear phthalocyanine complexes for application as possible nonlinear optical material.

TABLE OF CONTENTS

Contents

DEDICATION TO i

ACKNOWLEDGEMENTS ii

ABSTRACT iii

TABLE OF CONTENTS iv

LIST OF ABBREVIATIONS viii

LIST OF SYMBOLS x

LIST OF FIGURES xi

LIST OF SCHEMES xv

LIST OF TABLES xvii

1. Introduction 2

1.1. History of Phthalocyanines 2

1.2. Structure and applications of Phthalocyanines 2

1.3. General synthesis of Phthalocyanines 4

1.3.1. Synthesis of non-peripheral substituted Phthalocyanines 5

1.4. Electronic absorption spectra of Phthalocyanines 7

1.4.1. Aggregation of Phthalocyanines 10

1.5. Binuclear Phthalocyanines 13

1.5.1. General synthesis of Binuclear Phthalocyanines 14

1.5.2. Spectroscopic properties of Binuclear Phthalocyanines 16

1.6. Nonlinear Optical properties 18

1.6.1. Phthalocyanines nonlinear optical properties 24

1.6.2. Binuclear Phthalocyanines Nonlinear Optical Properties 27

1.7. Instrumentation/Spectroscopic Characterisation 32

1.7.1. Magnetic Circular Dichroism 32

1.7.2. Time Correlated Single Photon Count (TCSPC) 35

1.7.2.1. Fluorescence 35

1.8. Z-scan 38

1.8.1. Measuring Nonlinear Optical Properties 38

1.8.2. Theoretical background for Z-scan application 40

1.9. Theoretical/Computer Modelling 43

1.9.1. Density Functional Theory and Time Dependent Density Functional Theory calculations 43

1.9.2. Dipolar vs. Octupolar 44

1.10. Aims of Thesis 47

2. Experimental 50

2.1 Materials 50

2.2 Equipment/Instrumentation 51

2.3. Synthesis 53

2.3.1. Synthesis of phthalonitriles 53

2.3.1.1. Synthesis of 3-nitrophthalonitrile (5) 53

2.3.1.2. Synthesis of 3-(4-tert-butylphenoxy) phthalonitrile (7) 54

2.3.1.3. Synthesis of bisorthodinitrile (10) 54

2.3.1.4. Synthesis of 3-[4-[4-(2,3-dicyanophenoxy)phenyl]phenoxy]phthalonitrile (12a') 55

2.3.1.5. Synthesis of 3-[7-(3,4-dicyanophenoxy)-2-naphthyl]oxy]phthalonitrile (12b')

55

2.3.2. Synthesis of phthalocyanines and binuclear phthalocyanines 56

2.3.2.1. Preparation of 3,(4-tert-butylphenoxy)phthalocyanine (14a) 56

2.3.2.2. Preparation of (2,3-dicyanophenoxy)phenyl]phenoxy] binuclear phthalocyanine (15a) 57

2.3.2.3. Preparation of (2,3-dicyanophenoxy)phenyl]phenoxy]nickel binuclear phthalocyanine (15b) 57

2.3.2.4. Preparation of (3,4-dicyanophenoxy)-2-naphthyl] binuclear phthalocyanine (15c) 58

2.3.2.5. Preparation of (3,4-dicyanophenoxy)-2-naphthyl] nickel binuclear phthalocyanine (15d) 58

PUBLICATIONS 60

3. Results and Discussion 62

3.1. Phthalonitriles 62

3.1.1. Synthesis and characterisation of phthalonitrile complexes 62

3.1.2. Bisphthalodinitriles 64

3.2. Synthesis and spectroscopic characterisation of phthalocyanines and binuclear phthalocyanines 67

3.2.1. Attempt to synthesise binuclear phthalocyanine 67

3.2.2. Binuclear phthalocyanines 69

3.3. Electronic absorption and MCD spectroscopy 72

3.3.1. Phthalocyanines 72

3.3.2. Binuclear phthalocyanines 78

3.4. Absorption, fluorescence & excitation 85

3.4.1. Phthalocyanines 85

3.4.2. Binuclear phthalocyanines 88

3.5. Solid state absorption and UPS spectra of phthalocyanines 93

3.6. Experimental and computational nonlinear optical properties 96

3.6.1. Z-scan properties of phthatlocyanines 96

3.6.2. Z-scan properties of binuclear phthalocyanines 100

3.7. Density functional theory calculations for binuclear phthalocyanines 104

4. Conclusions 109

4.1. General conclusions 109

5. References 111

6. Appendix 121

LIST OF ABBREVIATIONS

Abs	-	Absorbance
BiPc	-	Binuclear phthalocyanine
Biph-BiPc	-	Biphenyl binuclear phthalocyanine
Biph-NiBiPc	-	Biphenyl nickel binuclear phthalocyanine
$CDCl_3$	-	Deuterated chloroform
DBU	-	1, 8-diazabicyclo[5.4.0]undec-7-ene
DCM	-	Dichloromethane
DFT	-	Density Functional Theory
DMAE	-	*N,N*-dimethylaminoethanol
DMF	-	*N, N*-dimethylformamide
Em	-	Emission
Exc	-	Excitation
H_2BiPc	-	Metal-free binuclear phthalocyanine
H_2Pc	-	Metal-free phthalocyanine
HOMO	-	Highest occupied molecular orbital
IC	-	Internal conversion
IP	-	Ionisation potential
IR	-	Infrared

ISC	-	Intersystem crossing
ITO	-	Indium tin oxide
LUMO	-	Lowest unoccupied molecular orbital
M	-	Metal
MCD	-	Magnetic circular dichroism
MO	-	Molecular orbital
MPc	-	Metallophthalocyanine
MS	-	Mass spectrometry
Naph-BiPc	-	Naphthyl binuclear phthalocyanine
Naph-NiBiPc	-	Naphthyl nickel binuclear phthalocyanine
NLO	-	Nonlinear optical
Pc	-	Phthalocyanine
Q_{vib}	-	Vibronic band of the Q band
TCSPC	-	Time correlated single photon count
TDDFT	-	Time-dependent density functional theory
THF	-	Tetrahydrofuran
UPS	-	Ultraviolet photoemission spectroscopy
UV/vis	-	Ultraviolet visible
V_m	-	Molecular volume

LIST OF SYMBOLS

m M/W	-	Metre megawatts
α	-	Non-peripheral position
β	-	Peripheral position
		Second order nonlinear polarizability
		Nonlinear absorption coefficient
β_{HRS}	-	Hyper-Rayleigh scattering nonlinear absorption coefficient
β_{λ}	-	Dynamic hyperpolarizability
Im(γ)	-	Imaginary hyperpolarizability
Im[$\chi^{(3)}$]	-	Imaginary susceptibility
τ	-	Fluorescence lifetime
ϕ	-	Anisotropy rotational correlation time
k	-	Boltzman constant
η	-	Viscosity
V	-	Molecular volume
T	-	Absolute temperature
λ_{ex}	-	Excitation wavelength

LIST OF FIGURES

Figure 1.1: General structure of Phthalocyanine. 3

Figure 1.2: General structures of tetra- and octa- substituted non-peripheral phthalocyanines. .. 5

Figure 1.3: Four positional isomers from 1,(4)-tetrasubstituted MPcs [18]. 6

Figure 1.4: Typical UV/vis spectra of free-base α (red) and β (blue) substituted phthalocyanines. 8

Figure 1.5: UV/vis spectra of zinc phthalocyanine [21]. 10

Figure 1.6: General structure of binuclear phthalocyanine (A-linker/bridge; R-substituent). ... 13

Figure 1.7: UV/vis of metal-free (5b) and zinc (6b) binuclear phthalocyanine [37]. 16

Figure 1.8: One-photon (left) and two-photon (right) absorption energy level diagram [44]. ... 23

Figure 1.9: Structural representation showing angles (θ and ϕ) between two Pc units linked through a bridge. 28

Figure 1.10: MCD mechanism illustrating A, B and C term respectively with the lcp and rcp represented by the dashed lines [100]. 34

Figure 1.11: Electronic absorption and magnetic circular dichroism (MCD) of MgBiPc [101]. 34

Figure 1.12: Excitation (solid line) and emission (dotted line) spectra illustrating a typical stokes shift [103]. 36

Figure 1.13: Typical diagram of a Z-scan setup [45]. 39

Figure 1.14: Typical z-scan spectra illustrating single and double valley curves [110]. 39

Figure 1.15: (a) Harmonic light intensity as a function of the polarization angle Ψ by polar representation, (b) Evolution of depolarisation ratio (ρ) as well as the octupolar [ϕ ($\beta_{J=3}$)] and dipolar [ϕ ($\beta_{J=1}$)] contributions to the second-order NLO response as a function of anisotropy factor [55] 44

Figure 1.16: The synthesised 3-(4-tert-butylphenoxy) phthalocyanine isomers. 47

Figure 1.17: The synthesised Biphenyl and Naphthyl linked binuclear phthalocyanines. 47

Figure 3.1: IR spectrum of Bisorthodinitrile (10) 65

Figure 3.2: Infrared spectra of bisphthalodinitriles. 66

Figure 3.3: Colour changes for the C_s (A), C_{4h} (B), D_{2h} (C) and C_{2v} (D) isomers in DCM. 68

Figure 3.4: The four positional isomers of 1, 8(or 11), 15(or18), 22(or25)-tetrasubstituted phthalocyanines. 68

Figure 3.5: Infrared spectra of phthalocyanine isomers. 69

Figure 3.6: Colour changes observed for (1A) Biph–H_2BiPc, (1B) Biph–NiBiPc, (2A) Naph–H_2BiPc and (2B) Naph–NiBiPc in THF. 71

Figure 3.7: Infrared spectra of binuclear phthalocyanines. 71

Figure 3.8: Optimised structures of 4α-(4-tert-butylphenoxy) phthalocyanine positional isomers with C_s (A), C_{4h} (B), D_{2h} (C), and C_{2v} (D) symmetry substitution patterns. 72

Figure 3.9: UV/vis absorption and MCD spectra of the 4α-(4-tert-butylphenoxy) phthalocyanine positional isomers measured in DCM. The calculated bands for the four positional isomers of the $H_2(OH)_4$Pc model compound are plotted against a secondary axis with red diamonds used to highlight the Q, B1 and B2 bands. 74

Figure 3.10: Nodal patterns (TOP) of the four frontier π–MOs of zinc tetraazaporphyrin (ZnTAP) with the angular nodal planes highlighted to describe the ML = ±4 and ±5 nodal patterns, and the nodal patterns of C_{4h} isomer of the $H_2(OH)_4$Pc model compound at an isosurface value of 0.04 a.u. Michl [131-135] introduced a, s, -a and -s nomenclature to describe the four frontier π–MOs based on whether there is a nodal plane (a and -a) or an antinode (s and -s) on the y-axis. Once the alignment of the angular nodal planes has been clearly defined the effect of different structural perturbations can be readily conceptualized on a qualitative basis through a consideration of the relative size of the MO coefficients on each atom on the perimeter. The MO energies (BOTTOM) of the four positional isomers

of the $H_2(OH)_4Pc$ model compound. The a, s, -a and -s MOs of Michl's perimeter model [131-135] are highlighted in gray. σ–MOs associated primarily with the aza-nitrogen lone pairs are offset to the right. Occupied MOs are denoted with small black diamonds. The HOMO–LUMO gap values are plotted against a secondary axis. 76

Figure 3.11: Optimised isomeric structures of Biph-H_2BiPc (A) and Biph-NiBiPc (B) with OH groups at the B3LYP level of theory with SDD basis set. 78

Figure 3.12: MCD and UV/vis spectra of Biphy-H_2BiPc-1 (E), Biphy-H_2BiPc-2 (F), Biphy-NiBiPc-1 (G), Biphy-NiBiPc-2 (H), Naph-H_2BiPc-1 (I), Naph-H_2BiPc-2 (J), Naph-NiBiPc-1 (K) and Naph-NiBiPc-2 (L) in THF. 81

Figure 3.13: The MO energies modelled as C_{4h} symmetry structures of Naph-H_2BiPc (A), Naph-NiBiPc (B), Biph-H_2BiPc (C), Biph-NiBiPc (D), H_2Pc (E) and NiPc (D). The HOMO-LUMO gap values are plotted against a secondary axis with the difference indicated. The eight BiPc MO's and four Pc MO's of Michl's perimeter model are highlighted in grey letters with small black diamonds. Michl [123-127] introduced a, s, -a and -s nomenclature to describe the four frontier π-MOs based on whether there is a nodal plane (a and -a) or an antinode (s and -s) on the y-axis. The effect of different structural perturbations can be readily understood by first defining the nodal planes and by considering the relative size of the MO coefficients on each atom in the perimeter. 83

Figure 3.14: UV/vis absorption, excitation and fluorescence emission spectra of isomers C_s (A), C_{4h} (B), D_{2h} (C) and C_{2v} (D) ($\lambda_{exc.}$= 620 nm). 85

Figure 3.15: Fluorescence decay curve for the C_s isomer in DCM with residuals (λ_{ex} = 670 nm). 86

Figure 3.16: UV/vis absorption, excitation and fluorescence emission spectra of binuclear phthalocyanine mixture of isomers for Biphenyl compounds E and F including Naphthyl compounds I and J ($\lambda_{exc.}$= 670 nm). 88

Figure 3.17: Fluorescence decay curve for the Biphenyl isomer in THF with residuals ($\lambda_{exc.}$ = 670 nm). 89

Figure 3.18: Time resolved emission spectra of (A) Biphy-H_2BiPc-1, (B) Naph-H_2BiPc-1, (C) Biphy-H_2BiPc-2 and (D) Naph-H_2BiPc-2 in THF. 90

Figure 3.19: UV/vis absorption spectra for C_s (black line), C_{4h} (red line), D_{2h} (dotted line), and C_{2v} (blue line) against an ITO background scan. 93

Figure 3.20: (a) Onset of the secondary electron cut-off and (b) valence band UPS spectra for C_s-H_2Pc (black line), C_{4h}-H_2Pc (red line), D_{2h}-H_2Pc (dotted line) and (4) C_{2v}-H_2Pc (blue line) system on bare ITO. 94

Figure 3.21: Schematic energy level diagram for the (A) C_s-H_2Pc, (B) C_{4h}-H_2Pc, (C) D_{2h}-H_2Pc and (D) C_{2v}-H_2Pc system on bare ITO. 95

Figure 3.22: Z-scan (a-d) and nonlinear fit (a′-d′) curves ($q_0(Z_s)$) for (a) C_s-H_2Pc, (b) C_{4h}-H_2Pc, (c) D_{2h}-H_2Pc and (d) C_{2v}-H_2Pc. All experiments were conducted in DCM solution. 98

Figure 3.23: Z-scan and nonlinear fit curves for Biph-H_2BiPc-1 (e, e'), Biph-NiBiPc-1 (f, f'), Naph-H_2BiPc-1 (i, i') and Naph-NiBiPc-1 (j, j') in THF solution. 101

Figure 3.24: Front (A) and side (B) view of naphthalene bridged nickel bis-4-hydroxy binuclear phthalocyanine. 105

Figure 6.1: MS of Biph-H_2BiPc, Biph-NiBiPc, Naph-H_2BiPc, Naph-NiBiPc, H_2Pc and NiPc. 121

Figure 6.3: Optimised isomeric structures of Naph-H_2BiPc (A) and Naph-NiBiPc (B) with OH groups. 124

Figure 6.4: Nodal patterns of Biph-NiBiPc, Naph-H_2BiPc and Naph-NiBiPc 127

Figure 6.2: Z-scan and nonlinear fit curves for Biph-H_2BiPc-2 (g, g'), Biph-NiBiPc-2 (h, h') Naph-H_2BiPc-2 (k, k') and Naph-NiBiPc-2 NiBiPc (l, l') in THF solution. 128

LIST OF SCHEMES

Scheme 1.1: First synthesis of a phthalocyanine molecule. 2

Scheme 1.2: The general synthesis of a phthalocyanine complex. 5

Scheme 1.3: Gouterman's four-orbital linear model [9]. 7

Scheme 1.4: An orbital energy diagram of mono-MPc and Pc [20]. 9

Scheme 1.5: Face-to-face, slipped cofacial and head-to-tail aggregates [26]. 11

Scheme 1.6: A qualitative orbital energy diagram for exciton coupling for monomer and dimer [26]. 12

Scheme 1.7: Mechanism of Binuclear Phthalocyanine Formation. (R – Group: any substituent, Q – any linker). 15

Scheme 1.8: A qualitative orbital energy diagram for exciton coupling [20] 17

Scheme 1.9: A schematic of a five-level RSA process. S_i and T_i represent singlet and triplet levels respectively. Solid arrows imply excitation from photon absorption and arrows with curvy midsection represent relaxations [17, 69]. 20

Scheme 1.10: Four level model for RSA, sequential two-photon absorption [70]. 21

Scheme 1.11: Jablonski Diagram [104]. 35

Scheme 3.1: Preparation of 3-nitrophthalonitrile (5). 62

Scheme 3.2: Preparation of 3-(4-tert-butylphenoxy) phthalonitrile (7). 63

Scheme 3.3: Preparation of Bisorthodinitrile (10). 64

Scheme 3.4: Preparation of 3-[4-[4-(2,3-dicyanophenoxy)phenyl]phenoxy]phthalonitrile (12a') and 3-[7-(3,4-dicyanophenoxy)-2-naphthyl]oxy]phthalonitrile (12b') respectively. 65

Scheme 3.5: Preparation of 3,(4-tert-butylphenoxy)phthalocyanine (14). 67

Scheme 3.6: Preparation of mono-Pc, H_2BiPc and Nickel Biphenyl (15a and 15b) and Naphthyl (15c and 15d) binuclear phthalocyanine complexes respectively. 70

Scheme 3.7: Harmonic light intensity as a function of the polarisation angle ψ by polar representation of Biphy-H_2BiPc-2 (C_{2v}:C_{2v}) (A), Biphy-H_2BiPc-1 (D_{2h}:D_{2h}) (B), Biphy-H_2BiPc-1 (C_{4h}:C_{4h}) (C), unsubstituted Biphy-H_2BiPc (D) and Biphy-H_2BiPc-1 (C_s:C_s) (E). 106

Scheme 6.1: Harmonic light intensity as a function of the polarization angle ψ by polar representation of the Biph-NiBiPcs. 129

Scheme 6.2: Harmonic light intensity as a function of the polarization angle ψ by polar representation of the Naph-H_2BiPc. 130

Scheme 6.3: Harmonic light intensity as a function of the polarization angle ψ by polar representation of the Naph-NiBiPcs. 131

LIST OF TABLES

Table 1.1: Known structural modifications of tetra-substituted Phthalocyanines 25

Table 1.2: Known peripherally substituted structures of BiPcs and Bis-Pcs 29

Table 3.1: Q band maxima in the absorption (Abs.), fluorescence excitation (Exc.) and emission (Em.) spectra, fluorescence lifetime (t), anisotropy rotational correlation time (Φ) values and molecular volumes (V_m) in DCM. 87

Table 3.2: Q band maxima in the absorption (Abs), and fluorescence excitation (Exc) and emission (Em) spectra, fluorescence lifetime (τ) and anisotropy rotational correlation time (Φ) values and molecular volumes (V_m) in THF and DCM. 91

Table 3.3: Experimental and theoretical Z-scan results for second order nonlinear polarizability, β. DFT calculated with the B3LYP functional and 6-31G(d) basis sets. 99

Table 3.4: Z-scan results for third order nonlinear hyperpolarizability, γ, and imaginary susceptibility, $Im[\chi^{(3)}]$. 99

Table 3.5: Experimental and theoretical z-scan results for second-order nonlinear polarizability, β, in THF. DFT calculated values at B3LYP functional and SDD basis set. 102

Table 3.6: Possible combinations of binuclear phthalocyanine isomers. 104

Table 6.1: TD-DFT spectra of the B3LYP optimized geometries of the four positional isomers of the $H_2(OH)_4Pc$ model compound calculated with the B3LYP functional and 6-31G(d) basis sets. 122

Table 6.2: TD-DFT spectra of the B3LYP optimized geometries of the model BiPc complexes calculated with the B3LYP functional and SDD basis sets. 125

Chapter 1

Introduction

1. Introduction

1.1. History of Phthalocyanines

The interest around macrocyclic compounds with metal-centres has increased over the past decades. A class of such macrocyclic compounds are phthalocyanines (Pcs) which were discovered through sheer serendipity at the Grangemouth plant of Scottish dyes Ltd (in 1907) by Braun and Tcherniac [1]. Pcs which are blue-green in colour, were the main product of an industrial preparation of two starting materials namely phthalamide and ortho-cyanobenzamide in acetone **(Scheme 1.1)** [1, 2]. However, since this product resulted through serendipity, not much attention was given to it until Linstead (in 1928) took interest in the compound.

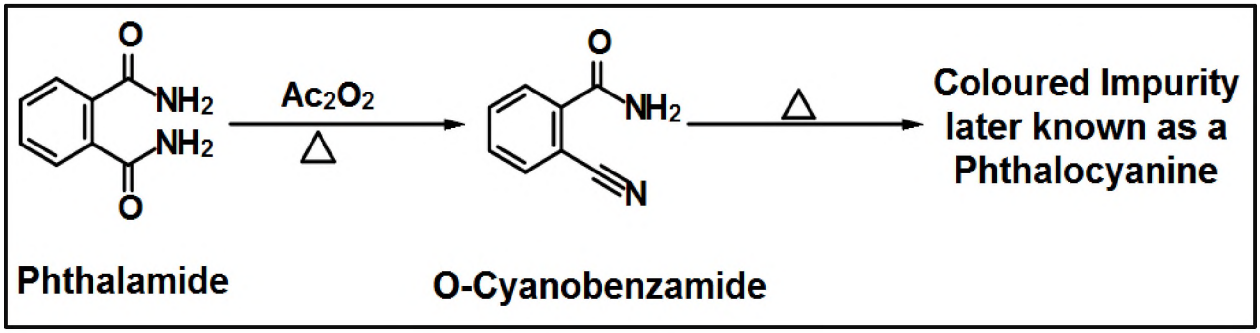

Scheme 1.1: First synthesis of a phthalocyanine molecule.

1.2. Structure and applications of Phthalocyanines

The Pc structure was named and carefully studied by Linstead using three particular techniques, mass determination, elemental analysis and oxidative degradation [3]. Other views hold that it was Dandridge (in 1928) who also discovered and named the Pc [4]. The name was derived from the Greek words “naphtha” meaning rock oil and “cyanine” meaning blue. Later, Linstead used a variety of analytical techniques to provide conclusive evidence on the structure of the phthalocyanine [5, 6]. Robertson further confirmed the Pc structure using x-ray crystallography which revealed the planar geometry of the Pc [7].

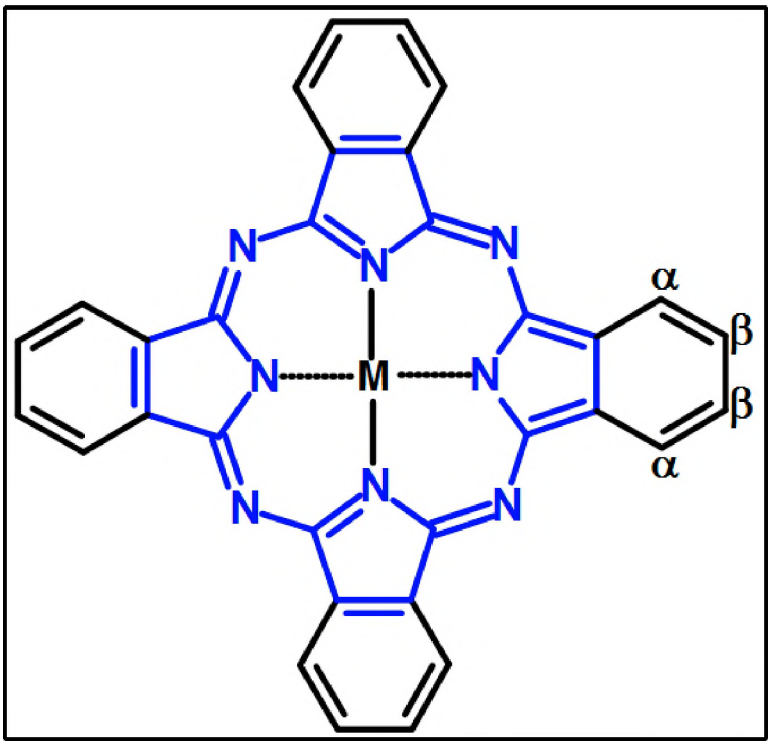

Figure 1.1: General structure of Phthalocyanine.

Phthalocyanines are heteroaromatic 18 π-electron compounds which have high chemical and physical properties as well as interesting optical properties [8]. Pcs consist of four isoindole units that are linked together by the *aza* nitrogen atoms. The inner aromatic ring **(Figure 1.1)** is responsible for the observed intense blue-green colour due to the π-π* transition in the visible region [9]. The four benzene rings on the outer most part of the Pc causes solubility and aggregation problems. However, substituting these outer benzene rings with functional groups on the peripheral (β) or non-peripheral (α) position **(Figure 1.1)** greatly improves solubility and avoids major aggregation in organic solvents [9].

One of the simplest analytical techniques used to characterise Pcs is ultra-violet visible (UV/vis) spectroscopy. The effect of β or α substitution, with electron withdrawing or donating groups, can be easily observed with UV/vis spectroscopy. Electron donating functional groups at the non-peripheral position will cause a greater bathochromic (red) shift of the main absorption band compared to β substituted functional groups. Electron withdrawing groups

such as NO_2 are meta-directing and make the aromatic ring to be deactivated due to the partially positive nitrogen atom. Substitution with suitable functional groups such as long alkyl chains, aryl, carboxylic acid, thiol and hydroxyl groups among others, have been observed to increase the intensity of the mean absorption band as well as altering the electrochemical and physical properties of Pcs [9].

Pcs intense blue-green colour makes them very attractive in the industry [10]. Pcs have been used as colorants in dyes, paints (for cars), dyestuff, [11, 12] plastics, pigments and colour photography [10] and in optical recording devices such as rewritable compact disc (RW-CD) ROM's. In recent years, they have been used as chemical sensors, organic conductors, catalysts, liquid crystal displays, in electro-chromism and laser dyes [12] for photodynamic therapy (PDT) [10] and nonlinear optical modulating devices [13]. The semi-conducting, conducting, high linear and nonlinear optical properties of most Pcs and their analogues are of particular interest for electronic and photonic devices [12].

1.3. General synthesis of Phthalocyanines

The general synthesis of Pcs is achieved through cyclotetramerisation reactions using different precursor/s **(Scheme 1.2)**. Phthalonitriles are the most preferred for research purposes because they offer easy and clean reactions with high purity products which often require minimal purification steps where necessary. Furthermore, using the phthalic anhydride route is relatively cheaper and is often used for large scale productions of metallophthalocyanines (MPcs). In addition, phthalic anhydride can be used as a precursor to synthesise phthalonitriles. For a successful synthesis of a Pc various factors such as the choice of the precursor/s, metal salt, solvent, temperature, base and catalyst need to be considered [14].

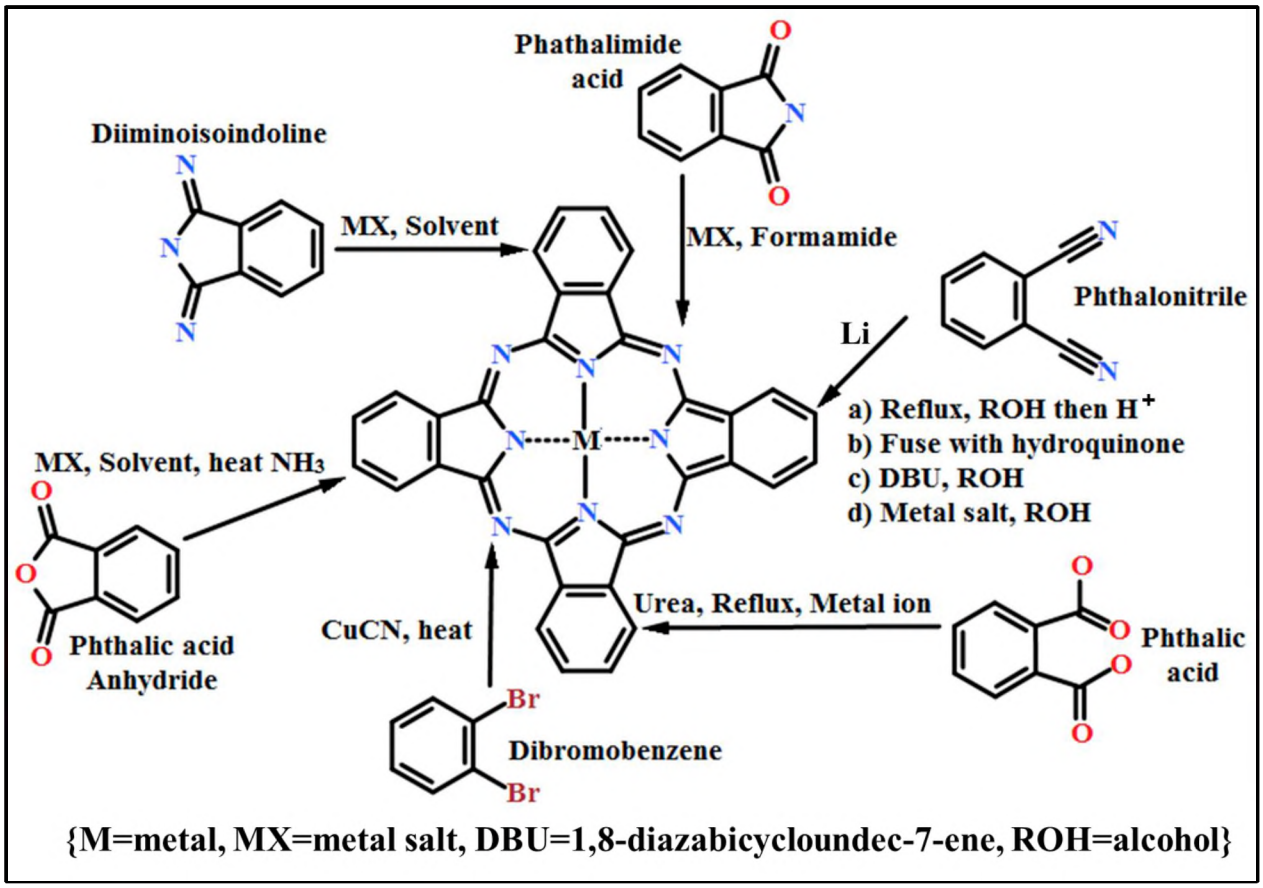

Scheme 1.2: The general synthesis of a phthalocyanine complex.

1.3.1. Synthesis of non-peripheral substituted Phthalocyanines

Phthalocyanine molecules have been synthesised for decades and can vary based on the precursors used which may have various substituents. There are two types of non-peripherally (α) substituted phthalocyanines i.e. tetra- and octa-substituted **(Figure 1.2)**.

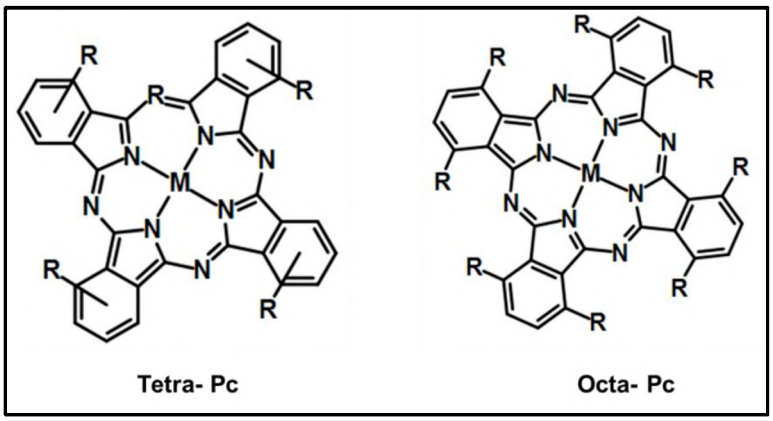

Figure 1.2: General structures of tetra- and octa- substituted non-peripheral phthalocyanines.

The tetra-substituted analogues when synthesised through mixed condensation results in the formation of four positional isomers while only one octa-substituted Pc is formed. The condensation method using an appropriately substituted precursor (usually phthalonitrile) is a commonly used method. This method enables the ability to control the formation of specifically substituted products permitted through phthalonitrile substitution at either α- or β-position. Monosubstitution at the α-position leads to four isomers of (C_{4h}) 1,8,15,22-, (C_{2v}) 1,11,18,22- (D_{2h}) 1,11,15,25- and (C_s) 1,8,18,22-tetrasubstituted symmetry **(Figure 1.3)**. The separation of the four isomers is known to be tedious and by column chromatography is usually highly challenging, but bulky substituents can be introduced to facilitate their chromatographic separation. Separation of the four isomers through high performance liquid chromatography (HPLC) has been reported where a statistical mixture of 12.5% C_{4h}, 12.5% D_{2h}, 25.0% C_{2v} and 50% C_s is obtained [15, 16]. Less symmetrical isomers have shown to have a higher dipole moment that is derived from the more unsymmetrical arrangement of the substituents in the periphery of the ring [15, 16]. Substitution at the non-peripheral α-positions is known to have a greater effect on the energies of the four frontier π-MOs of the phthalocyanine π-system [17].

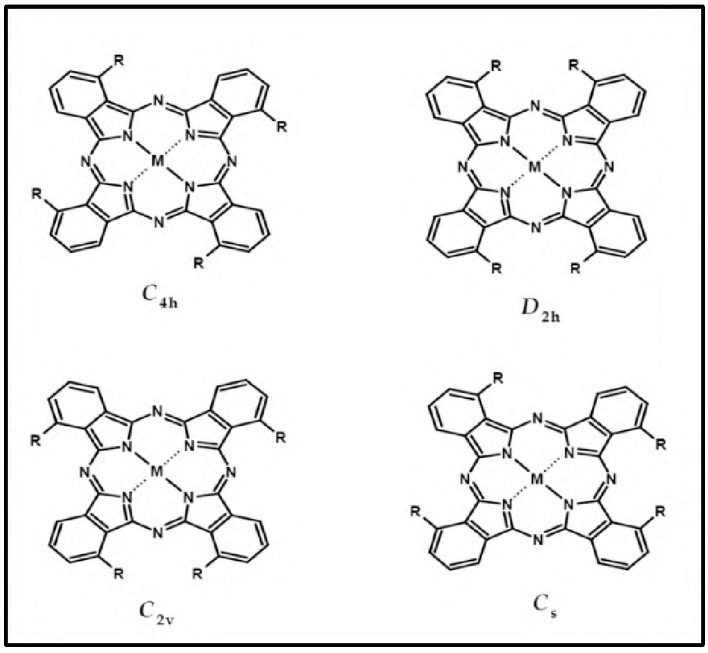

Figure 1.3: Four positional isomers from 1,(4)-tetrasubstituted MPcs [18].

The substituents at either the non-peripheral and peripheral positions (referred to throughout as the α- and β-positions, respectively) of each fused benzene ring can be orientated in two directions with respect to the rest of the ligand. The substitution patterns in this study have been labeled as D_{2h}, C_{4h}, C_{2v} and C_s throughout to aid comparison with D_{4h} symmetry of metalated complexes [17]. However, it should be noted that the free base phthalocyanine in this study have lower symmetry than this due to the absence of a four-fold axis of symmetry. Non-peripherally substituted Pcs have lower aggregation tendencies and their linear absorption band, in the higher wavelength region, is highly red-shifted when compared to β substituted complexes. The importance of red-shifting may result in the reduction of interferences due to linear absorption of materials [19].

1.4. Electronic absorption spectra of Phthalocyanines

The general absorption electronic spectra of Pcs are as a result of the electronic transitions between the highest occupied molecular orbital (HOMO) and lowest unoccupied molecular orbital (LUMO) **(Scheme 1.3)**.

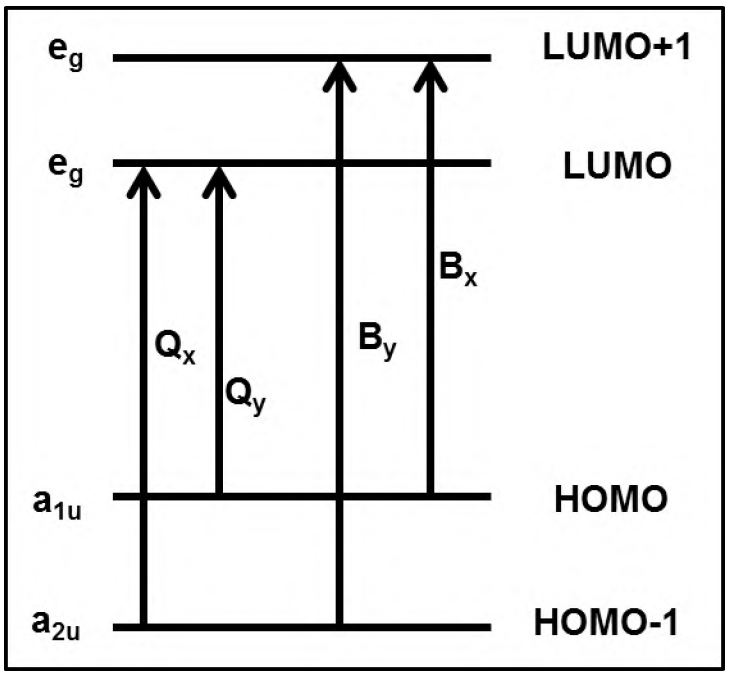

Scheme 1.3: Gouterman's four-orbital linear model [9].

The typical UV/vis spectrum shown in **Figure 1.4** illustrates the formation of two major absorption bands that are due to π–π* transitions referred to as the **Soret** band (also known as the **B band**) at 300–450 nm and **Q band** at 650–720 nm.

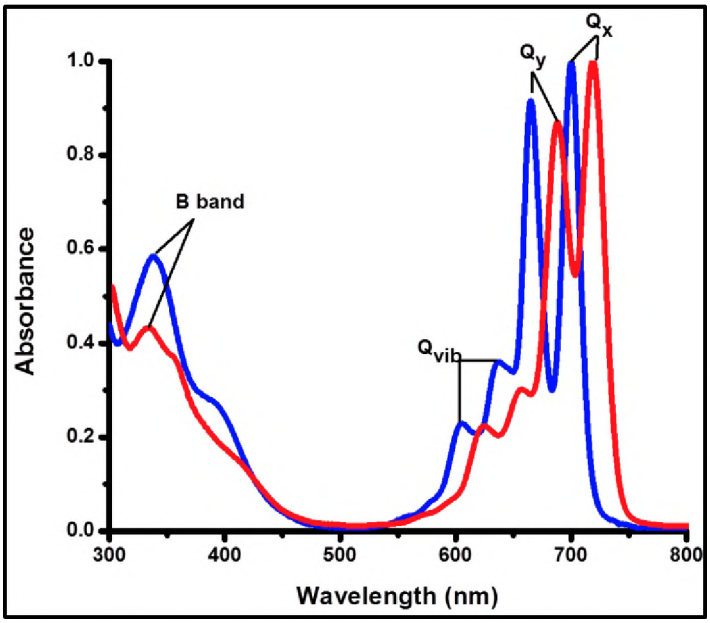

Figure 1.4: Typical UV/vis spectra of free-base α (red) and β (blue) substituted phthalocyanines.

For metal-free Pcs, the Q band appears as two intense peaks which results from $a_{1u} \rightarrow e_g$ and $a_{2u} \rightarrow e_g$ transition **(Scheme 1.4)** [20]. Metal-free Pcs have D_{2h} symmetry (as mentioned before) which results in the observation of the split Q band referred to as Q_y and Q_x **(**see **Figure 1.4)**. The observed split Q band arise from splitting the e_g energy level **(**see **Scheme 1.3)**.

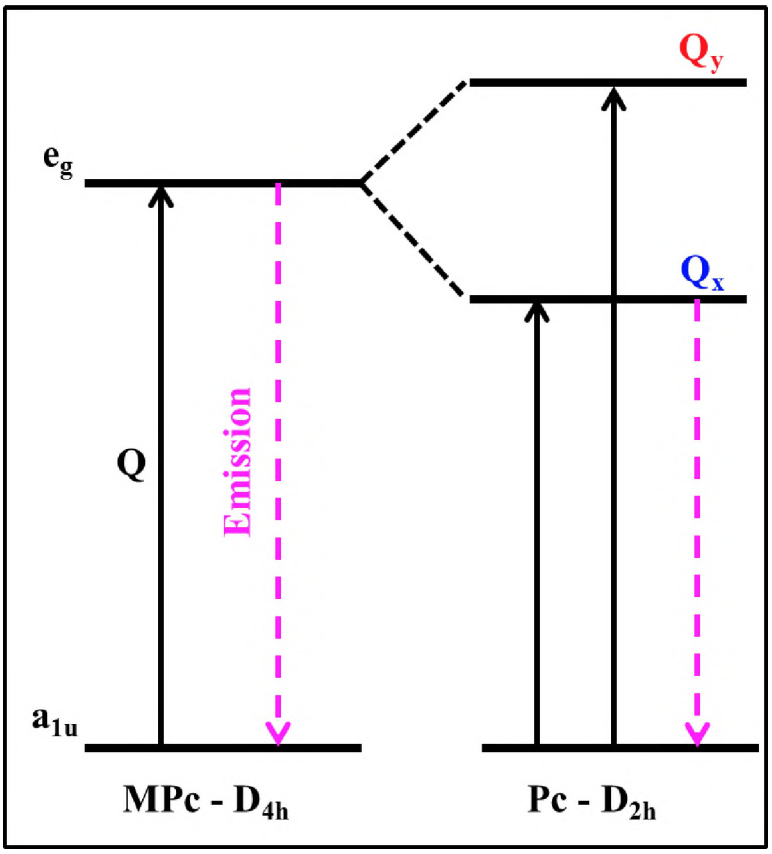

Scheme 1.4: An orbital energy diagram of mono-MPc and Pc [20].

In addition, the Q band has two weaker vibrational bands at higher energy of the main absorption peak termed vibronic bands (Q_{vib}). The **B band** appears as a less intense peak at the lower wavelength. It arises due to $a_{2u} \rightarrow e_g$ and $a_{1u} \rightarrow e_g$ transitions. **Figure 1.5** shows a typical UV/vis spectrum of a metalated Pc (MPc) which appears as a single Q band. The single Q band is observed due to the doubly degenerate e_g orbitals **(Scheme 1.4)**. The presence of a central metal increases the symmetry from D_{2h} to D_{4h}. MPcs are generally blue-shifted relative to the metal-free Pc [20].

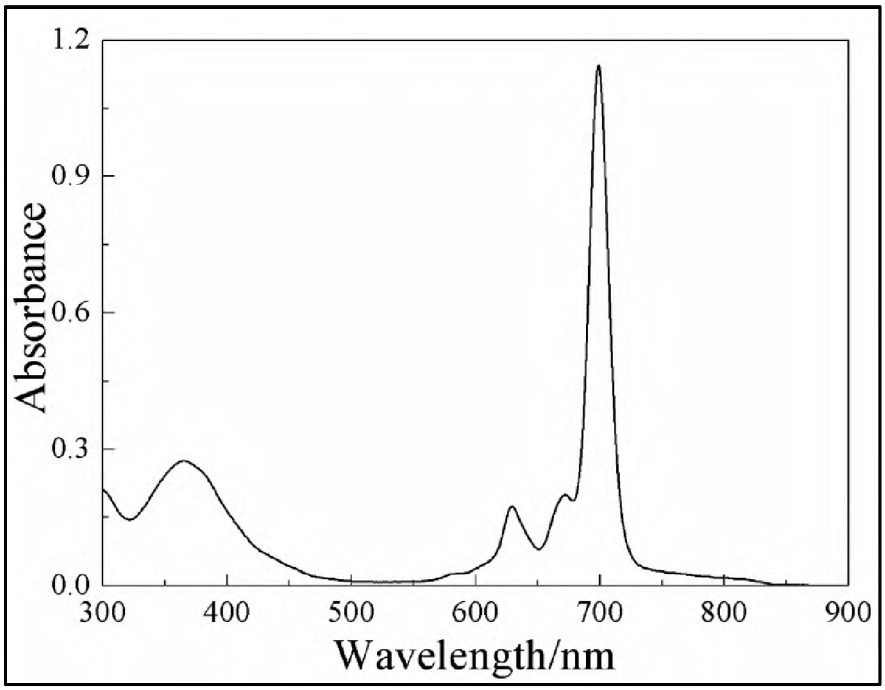

Figure 1.5: UV/vis spectra of zinc phthalocyanine [21].

1.4.1. Aggregation of Phthalocyanines

Generally metal-free Pcs do not exhibit aggregation (self-association) in common organic solvents however, this may be different for high concentration of the Pc [20, 22]. This is most evident in the drastic change in absorption spectra, which was discovered by Jelly and Scheibe in 1936 [23, 24].

The molecular orientation of the Pc can result in different types of aggregation patterns namely, H-aggregates, J-aggregates [25] and intermediate aggregates **(Scheme 1.5)** [26]. H-aggregates are ideally non-fluorescent in nature [27]. This behaviour limits the use of H-aggregate chromophores because they are not useful in designing display devices and sensors [25, 27]. On the other hand, J-aggregates are known to have a sharp (i.e. intense and narrow) main absorption band, red-shifted with respect to the monomer and have a strong photoluminescence with almost zero stokes shift [27-29]. J-aggregates have high oscillator strength of their electronic excitations in nonlinear optical properties [30]. Aggregation occurs as a result of π–π stacking between molecules, which results in a shifted absorption band with

respect to the Q band respectively [25]. The π–π stacking is governed by van der Waals' attractive forces between Pc rings where the interaction is between two or more electronic states [20, 22]. Aggregation can significantly affect the optical properties of Pcs in solution (organic or aqueous) and films [20, 22]. The interaction between electronic states of Pcs alters the properties of the ground and excited states.

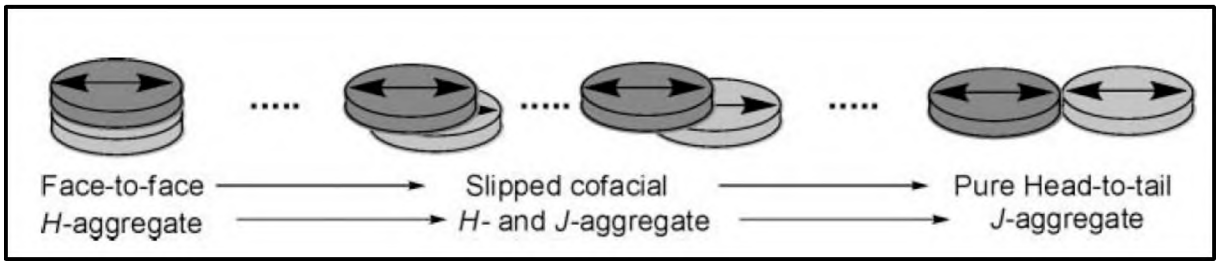

Scheme 1.5: Face-to-face, slipped cofacial and head-to-tail aggregates [26].

Scheme 1.6 shows the splitting of energies due to different aggregation patterns. Small distances between two Pc rings results in the interaction of excited states such that two new exciton splitting energy levels (E′ and E″) are produced **(see Scheme 1.6)**. Excitation to the lower energy state (E′) in the Face-to-face orientation is forbidden. Similarly, the excitation to the higher energy state in the Head-to-tail orientation is also forbidden. The forbidden transitions are represented by dashed arrows. The Oblique orientation shows that all transitions are allowed. The splitting of the two energies is dependent on the following properties: the intensity of the Pc transition moments, the separation of the two molecules and their relative orientation to each other.

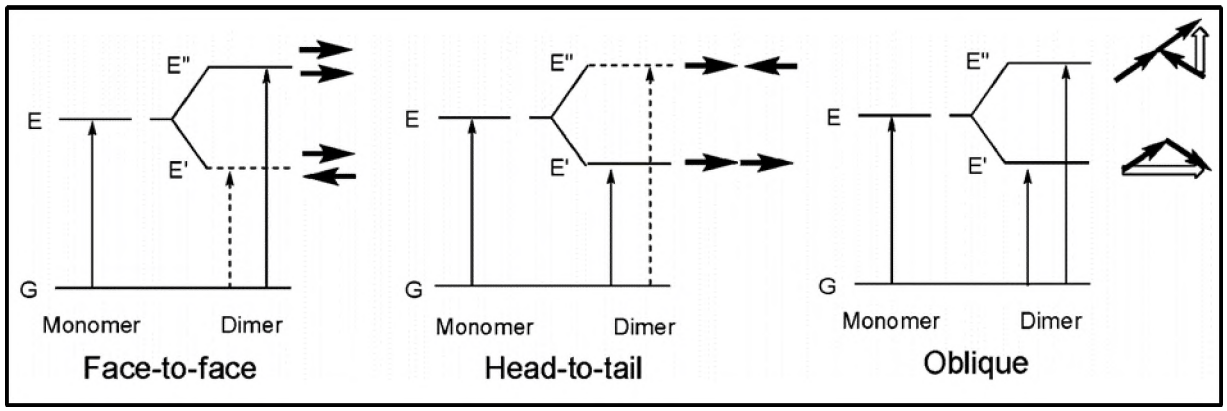

Scheme 1.6: A qualitative orbital energy diagram for exciton coupling for monomer and dimer [26].

Two types of dipoles are observed from **Scheme 1.6** namely, out of phase (E′) and in phase (E″). When the dipoles are out of phase, the lowering of energy, and zero transition moment together with the forbidden transition to E′ is observed which results in a blue-shifted absorption spectrum [26, 31, 32]. When the dipoles are in phase, the raising of energy, zero transition dipole and forbidden transition to E″ is observed which results in a red-shifted absorption spectrum [26, 31, 32]. The reduction in the degree of freedom compared to liquid state is observed in solid-state, therefore the transition moment may not equal zero [32]. Therefore in solid state, allowed transitions for both E′ and E″ can be observed. This is the reason for the observation of blue and red shifts as a split Q band, this is called Davydov splitting **(**see Oblique in **Scheme 1.6)**. Davydov splitting is defined as the splitting of bands in the electronic or vibrational spectra of crystals due to the presence of more than one equivalent molecular entity in the unit cell [32].

1.5. Binuclear Phthalocyanines

Binuclear phthalocyanine (BiPc) complexes are two phthalocyanine molecules joint by various types of linkers (eg. benzene, naphthalene ring, etc) and have two metal centres **(Figure 1.6)**. The linker is known to increase the stability of BiPcs. One BiPc is twice as effective compared to a single Pc. BiPcs exhibit twice the stability, versatility and process-ability features [33].

BiPcs have been used as photosensitizers for photodynamic therapy (PDT), electronics [8], photonics, optoelectronics, and optical limiting devices for protection of the eye, sensor protection from energetic light pulses [34], nonlinear optical modulating devices, and building blocks for making doubly-linked stacked conducting metallo-macrocyclic polymers [35].

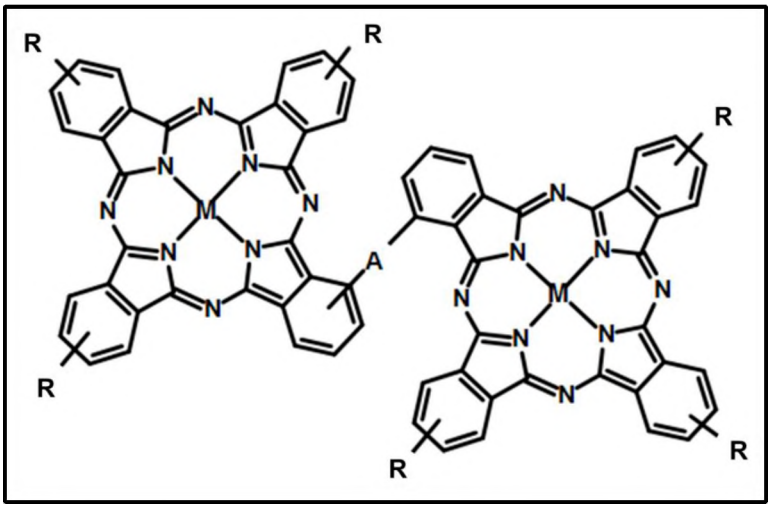

Figure 1.6: General structure of binuclear phthalocyanine (**A**-linker/bridge; **R**-substituent).

Due to the linker/bridge between the two macrocycles, the BiPc has been observed to have various conformations such as planar, co-facial and clamshell [36]. The planar and co-facial BiPc conformations are known to exhibit effective catalytic reactions where four electron reduction of oxygen to water has been achieved [36, 37]. Clamshell-type BiPc conformation have shown to have an affinity for bi-functional organic molecules (e.g. bis-dithiolene complex) during the analytical recognition process [8, 38]. The extensive π-conjugation in BiPcs contributes to aggregation. Two desirable properties offered by BiPcs as nonlinear

optical materials are a strong red (bathochromic) shift of the Q band and the enlargement of the highly transparent window between Q and B-bands [34].

1.5.1. General synthesis of Binuclear Phthalocyanines

Similarly to mono-Pcs, the synthesis of BiPcs can be carried out by condensation of bis-1,3-diiminoisoindolines in *N,N*-dimethylaminoethanol (DMAE) under reflux. The main product is a symmetrical mono-Pc while the desired BiPc is only about 13% [38]. Another synthetic route is to use bisphthalodinitriles in which BiPcs are obtained in 1-8% yields [38]. The bisphthalodinitriles synthetic route is referred to as statistical condensation method. The statistical condensation method involves a reaction of the bisphthalodinitrile and phthalonitrile of interest in a statistical ratio. The problem with this method, is that BiPcs are obtained in small amounts with respect to normal Pc formed during the reaction process. Separation of the BiPc from the monomeric species is a difficult part of the process. There are various methods employed for separation, such as pure solvents that can move faster or slower with respect to monomeric/normal Pc. A mixture of 2-methoxyethanol and toluene in various ratios has been previously used as a good eluent [39].

Scheme 1.7 shows a mechanism followed by a statistical condensation reaction, with starting materials in a ratio of 1:6 or 1:20. This method depends on relative reactivity of the starting bisphthalonitrile and phthalonitrile. The reactivity can also be improved by reducing the nitrile groups to secondary amines by bubbling ammonia gas in methanol in the presence of sodium methoxide [40]. The presence of sodium methoxide facilitates formation of diiminoisoindoline [40]. The diiminoisoindoline is highly reactive and can be used as a precursor for the synthesis of phthalocyanine analogues.

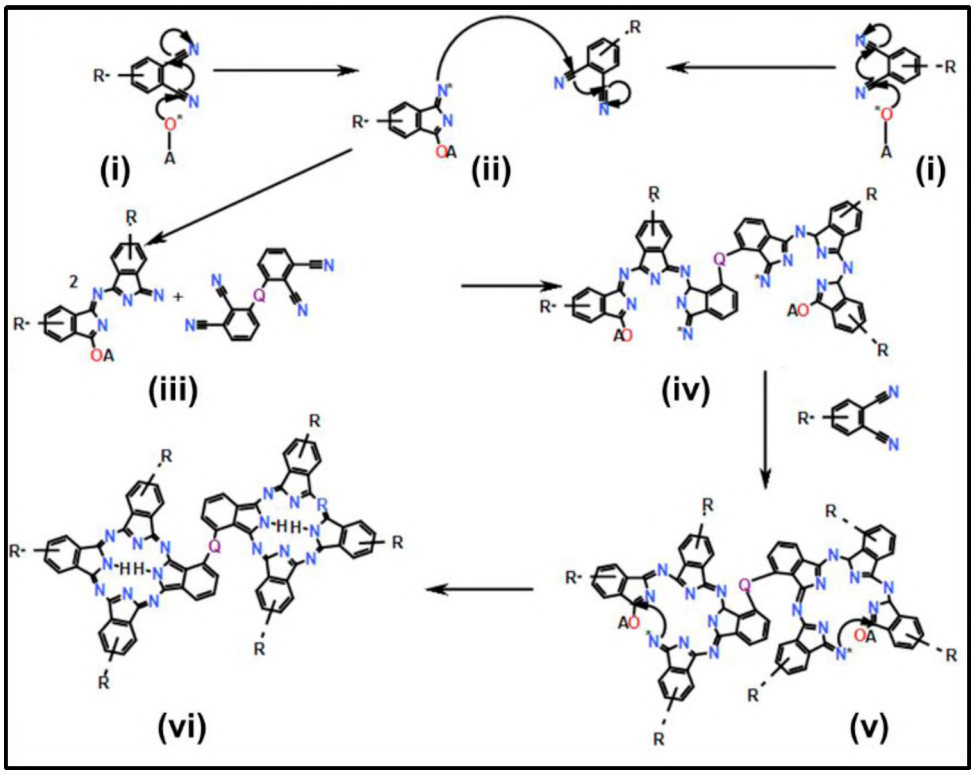

Scheme 1.7: Mechanism of Binuclear Phthalocyanine Formation. (**R** – Group: any substituent, **Q** – any linker).

The suggested mechanism for the formation of BiPc in **Scheme 1.7** is adopted from Baumann *et al.* [41]. In the presence of 1-octanol and lithium (which serves as a lithium alkoxide) a nucleophilic attack of the alkoxide ion **(i)** on the phthalonitrile takes place to form the monomeric alkoxyiminoisoindolenine intermediate **(ii)** [41]. This intermediate reacts with the linker to form the dimeric intermediate **(iii)**. This is followed by a subsequent reaction with another phthalonitrile molecule (R-group) to give the trimeric indolenine intermediate **(iv)** on either side of the linker. This intermediate **(iv)** further reacts with yet another phthalonitrile molecule to give **(v)**. Ring closure then occurs, involving the second nucleophilic attack of the reaction, on the aryl ether by the imide group followed by the subsequent loss of the ether as an aldehyde (i.e. the oxidation product) [42]. A hydrogen ion is released in the process which is taken up by excessive alkoxide ions in the reaction mixture. This synthetic process occurs at

extremely high temperatures and can result in an isomeric mixture that may be difficult to separate [43].

1.5.2. Spectroscopic properties of Binuclear Phthalocyanines

The extent of conjugation/coupling determines the electronic absorption spectra signature of BiPcs [20, 34]. According to Dodsworth *et al.* [20], a fully uncoupled BiPc complex will display an electronic spectrum that may look identical with that of a mono-Pc complex. In general coupling can be expected to occur: a) through space in a closed co-facial clamshell, b) through space between two halves if a BiPc in a partially open or a fully open conformation, or c) via conjugation through an unsaturated bridge [20]. In addition, depending on the nature of the bridge/linker, BiPcs can exist in dynamic equilibrium between various conformations [20, 34]. There are infinite numbers of conformations that can occur in solution. **Figure 1.7** shows commonly observed electronic absorption spectra of BiPcs. The spectra show broad and moderately intense major bands. The broadness is suggested to be an indication of the diverse number of conformers in solution [20, 34, 37]. Dodsworth *et al.* [20], observed that if there is a shift in absorption to higher energy relative to the monomer, it is an indication of coupling [20].

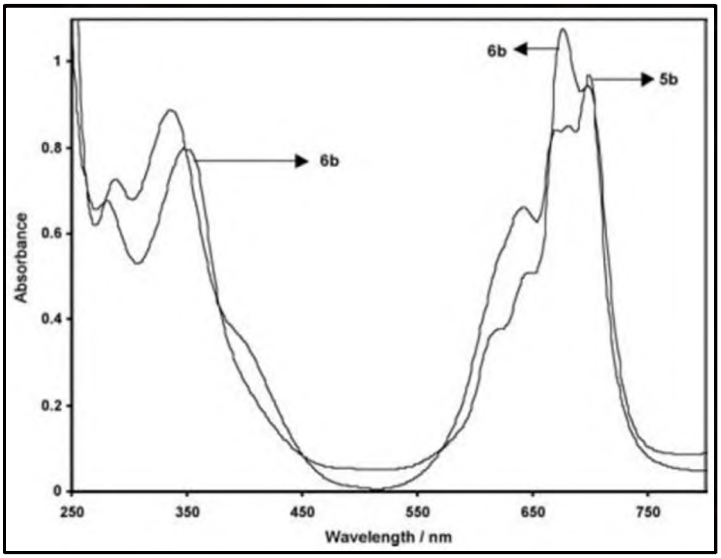

Figure 1.7: UV/vis of metal-free **(5b)** and zinc **(6b)** binuclear phthalocyanine [37].

Scheme 1.8 shows a qualitative orbital energy diagram for exciton coupling for MPc, Pc and BiPc [20]. The two major bands observed for BiPcs are similar to that of mono-Pcs however, the Q bands consist of twice the number of Q_x and Q_y which are superimposed **(Scheme 1.8)**. Hence only two bands are observed in the Q band region of the electronic absorption spectrum.

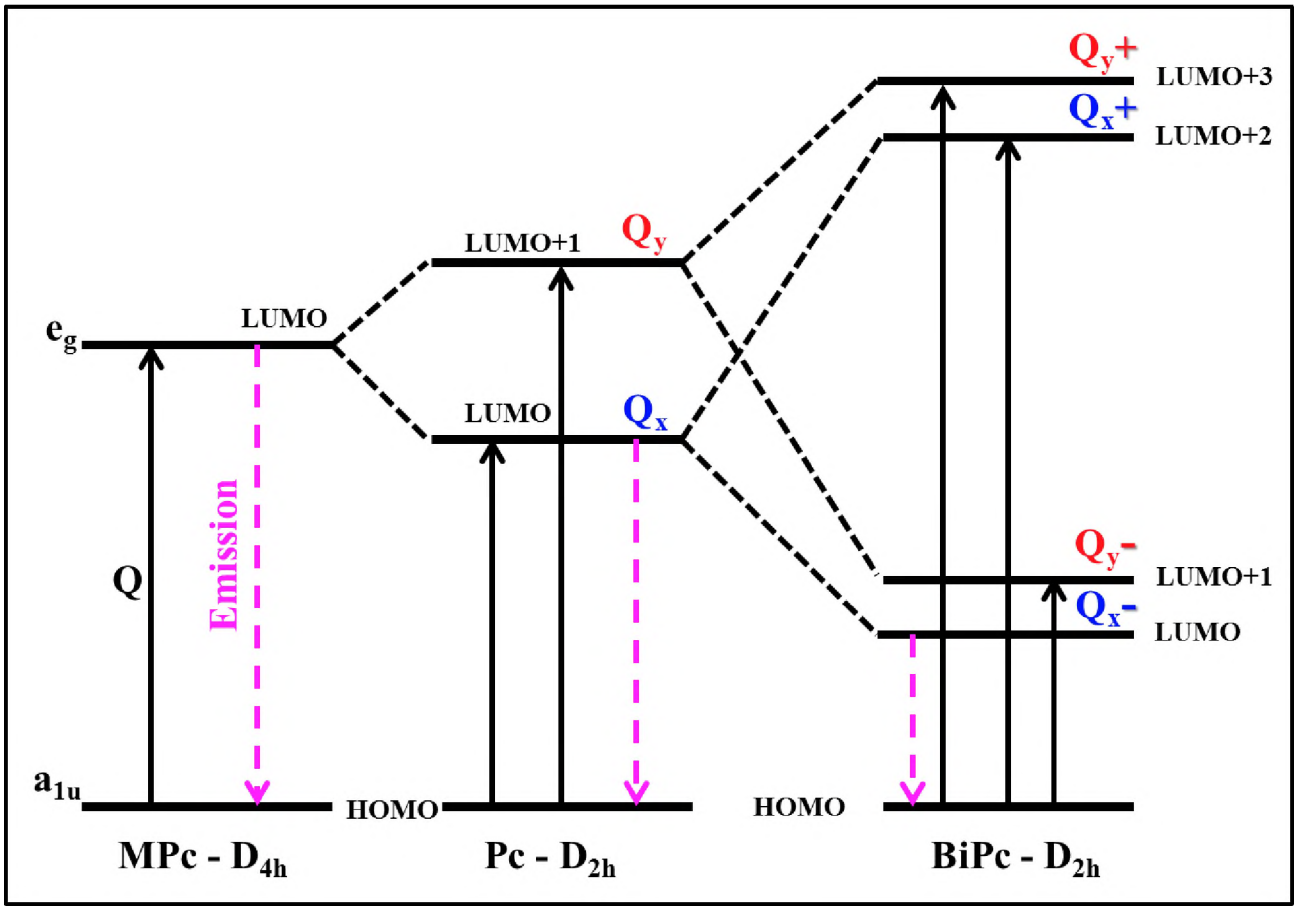

Scheme 1.8: A qualitative orbital energy diagram for exciton coupling [20]

As mentioned above, aggregation is a phenomenon which is due to the strong coupling between the molecules that causes either a red or blue shift in the absorption band of the aggregate [37]. Aggregation is usually depicted as a coplanar association of rings progressing from a monomer to a dimer and higher order complexes which in turn affect the shape of the Q band [25]. Aggregation is dependent on concentration, the nature of the solvent, the nature of the substituents, complex metal ions and temperature [25]. Both the metal-free and zinc binuclear phthalocyanine show aggregation bands **(Figure 1.7)**. From the possible aggregation

patterns/orientations it can be noted that J-aggregates are desirable in nonlinear optics because they are both fluorescent and have triplet state photo-activity [29].

1.6. Nonlinear Optical properties

Nonlinear optics is a study that is concerned with the understanding of the behaviour of light matter interactions when the materials response is a nonlinear function of the applied electromagnetic field [44]. The invention of the laser (1960s) was an advance in technology and as a result introduced the study of materials with nonlinear optical (NLO) properties. A laser has high intensity light which has the ability to damage optical sensors e.g. human eye, range finders and night vision equipment [45]. Hence, research has looked into studying materials to help protect these sensors from the dangers of laser light. In 1875, a Scottish physicist John Kerr was the first person to observe the change in the refractive index of organic liquids and glass in the presence of an electric field [44]. This phenomenon birthed the study of Nonlinear Optics.

The study of nonlinear optical (NLO) properties is to predict the values of nonlinear absorption coefficient (β) and imaginary susceptibility (γ) for various chemical structures [33]. Nonlinear absorption is a process where two photons are absorbed simultaneously. The predicted values establish the basis for the optimisation of the microscopic NLO performance [33]. The first material that was discovered to have nonlinear optical (NLO) activity were inorganic crystals such as lithium niobate ($LiNbO_3$) and potassium dihydrogen phosphate (KH_2PO_4) [33]. These crystals displayed low NLO responses, processing them into thin films and incorporating them into micro-optoelectronic devices [33] posed a serious problem. P-electron organic material were potential candidates for NLO material however, π-electron conjugated systems received more attention because they possessed more advantages [46-48]. These include having larger optical nonlinearity and faster optical response [49]. Higher bandwidth, lower driving voltage, more flexible device design and lower processing cost are the additional advantages that π -

electron material display [50, 51]. Therefore, organic material with second-order NLO properties have been investigated over the past two decades and are useful in applications such as optical data processing, information storage, electro-optical and optical sensors which can be easily processed and integrated into optical devices [7, 52-59]. Research has shown that developing molecules that exhibit large and rapid nonlinearities to incident pulsed laser light, can be fine-tuned by rational modification of the molecular structure [60-62].

The structural prerequisites for developing efficient NLO requires the material to possess a network of highly delocalised π-electron system which would infer high polarizability and fast charge redistribution upon rapidly varying electromagnetic fields such as laser radiation [7, 8, 63]. Pcs and BiPcs have become the most studied NLO organic materials and their structural conformations contribute to the β values observed. Pcs and BiPcs have shown to display large third-order optical nonlinearities which arise from the highly delocalised two dimensional heteroaromatic 18-π electron system [62, 64-66]. In addition, chemical and thermal stability of Pcs and BiPcs makes them attractive for use as NLO material. NLO materials (also known as optical limiters) need to have the following criteria i.e. transmit light of low intensities while absorbing harmful high intensity light.

Nonlinear optical materials rely on the nonlinear absorption coefficient (β) value because it measures the materials third order optical nonlinearity. Third-order nonlinearity arises from expanding the nonlinear susceptibility to third-order in the electric field [67]. There are three electric fields: E_0, E_2 and E_3 each oscillating at ω_0, ω_2 and ω_3 respectively. Depending on the medium, third harmonic can be considered as being generated by three fundamental photons, which require phase-matching. Alternatively, the third harmonic can be generated by a single incident photon interacting with the harmonic (a different kind of phase-matching) [67]. There are two types of nonlinear absorption namely saturable and multi-photon absorption. The former occurs when the incident intensity is high enough that the ground state population is

depleted and the population of the upper and lower states equalizes [67]. The latter, multi-photon absorption, increases with intensity. It is often referred to as Reverse saturable absorption (RSA). This optical nonlinearity decreases the transmission of light as molecules undergo absorption, which causes the molecules to transition to higher levels.

RSA is a multi-step process which can be illustrated by **Scheme 1.9** and **Scheme 1.10**. The steps involved include excited state absorption (ESA) from the singlet ground state to the first excited triplet state through the first excited singlet state [68, 69]. **Scheme 1.9** shows RSA in a Pc system where the electronic states of the vibrational levels have been ignored. An initial excitation occurs from S_0 to S_1, accompanied by the population of the first excited singlet state S_1. Within the pulse width of the laser, electrons are subsequently excited from S_1 to S_2. S_1 may also undergo intersystem crossing (ISC), with a time constant τ_{ISC}, to the first excited triplet state T_1. Subsequently, excitations and relaxation to and from T_2 occurs. A cyclic exchange of the population of electrons occurs between S_1 and T_1, as the lifetime of T_1 (τ_{ph}) is very long when compared to τ_{ISC} [68, 69].

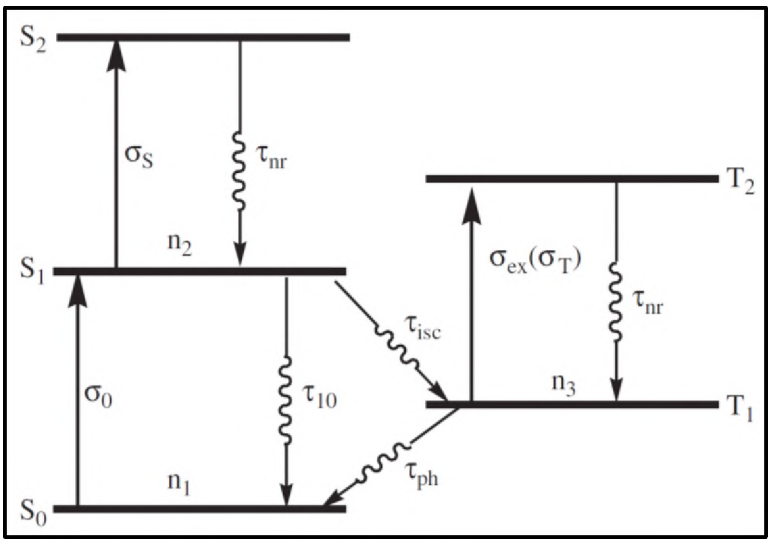

Scheme 1.9: A schematic of a five-level RSA process. S_i and T_i represent singlet and triplet levels respectively. Solid arrows imply excitation from photon absorption and arrows with curvy midsection represent relaxations [17, 69].

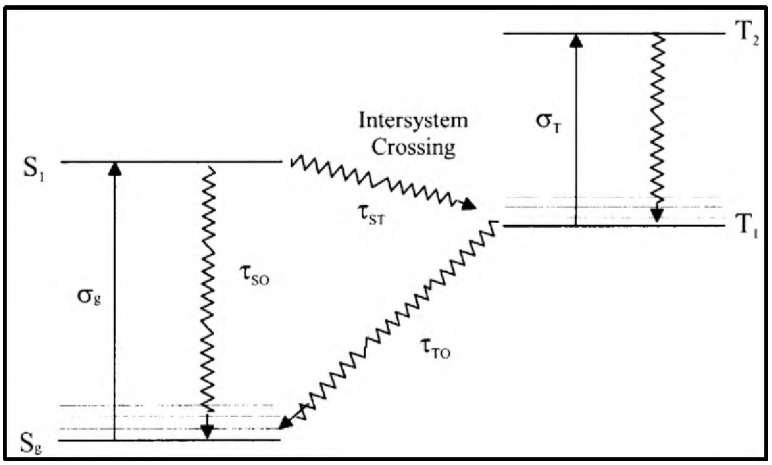

Scheme 1.10: Four level model for RSA, sequential two-photon absorption [70].

Pcs and BiPcs have been studied as NLO material because of the presence of strong nonlinear absorption coefficient (β) which originates from triplet-triplet (T_1–T_2) and intersystem crossing (ISC) **(Scheme 1.10)** [70, 71]. The T_1–T_2 absorption is responsible for the decrease in the transmitted light after laser light causes two-photon absorption and ISC to the triplet state [71]. As OL, Pcs and BiPcs have been observed to have reverse saturable absorption, which effectively limits the output of energy of incident light [71].

The propagation equation shown below **(Equation 1)** governs the extinction of incident beam

$$\frac{\partial I}{\partial z} = -\alpha_{NL} I = -\left(\sigma_0 N_1 + \sigma_S N_2 + \sigma_T N_3\right) I \qquad (1)$$

where α_{NL} (which approximates to nonlinear absorption coefficient) is composed of the ground state absorption $\sigma_0 N_1$, the first excited singlet state absorption $\sigma_S N_2$ and the first excited triplet state absorption $\sigma_T N_3$. N and σ refer to the population and absorption cross section of specific energy levels. The four-level **(Scheme 1.9)** and five-level model **(Scheme 1.10)** reproduces the RSA effects and highlights the crucial role that the ESA plays in the overall absorption coefficient [69].

In addition, light-matter interactions are usually considered within the framework of the Lorentz model [45, 72]. In this model, the electrons are considered to be bound to the atom in a harmonic potential. This is equivalent to expressing the polarization of the material as a result of an electric field **(Equation 2)** as:

$$P\ E\ = \epsilon_0\ \chi^{(1)} E \qquad (2)$$

where the dielectric displacement polarization *P(E)* is the dipole moment per unit volume, $\epsilon_0$is the permittivity of free space, $\chi^{(1)}$is the linear susceptibility of the material and E is the electric field. This accounts accurately for all linear phenomena occurring during light-matter interactions. This however, does not explain the nonlinear phenomena observed when high intensity light interacts with matter. To explain this, it is necessary to consider the electron to be bound in a mere generalised potential namely an anharmonic potential which is approximated by a harmonic potential at low energies [45, 46].

The well-known Beer's law is applicable when considering linear absorption specifically. This is depicted by **Equation 3**:

$$I\ z\ = I_0 e^{-\alpha\ \omega\ z} \qquad (3)$$

where I_0 is the incident light, $\alpha(\omega)$is the linear absorption coefficient, *z* being the propagation depth in the absorbing medium and finally $I\ z$ as the intensity at depth *z*.

Beer's law is merely the solution of the differential **Equation 4** that describes how light intensity decreases with propagation depth in a medium for the case where α is a constant [45].

$$\frac{\partial I}{\partial z} = -\alpha\ \omega\ I \qquad (4)$$

If nonlinear (multi-photon) effects are to be included then this differential equation must be extended to include higher order intensities **(Equation 5)**

$$\frac{\partial I}{\partial z} = -\alpha\ \omega\ I - \beta\ \omega\ I^2 - \gamma\ \omega\ I^3 - O(I^4) \quad (5)$$

where $\beta\ \omega$ = two photon absorption coefficient

$\gamma\ \omega$ = three photon absorption coefficient

$O(I^4)$ = four- and higher photon absorption coefficients

In this thesis, the material used displays negligible linear absorption and is dominated by two-photon process **(Figure 1.8)**. A photon is excited if its energy matches the difference in energies between the 2 states. The two-photon absorption results when each of the energy (E_2-E_1)/2 are sequentially absorbed [44].

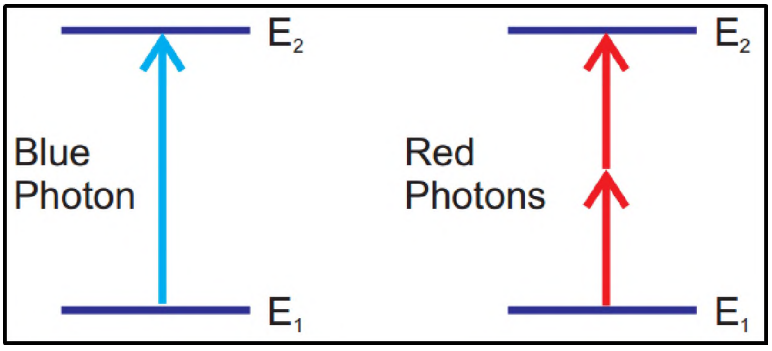

Figure 1.8: One-photon (left) and two-photon (right) absorption energy level diagram [44].

Therefore, the other terms in the above equation have been disregarded thus only $\frac{\partial I}{\partial z} = -\beta\ \omega\ I^2$ is considered. However, this equation needs to be solved and thus the following separation of variables is applied **(Equation 6)**

$$I\ z\ = \frac{I_0}{1+\beta I_0 z} \quad (6)$$

where β, is the nonlinear absorption coefficient as mentioned before and z is the distance travelled by light in the sample [44].

An alternative method that can be used to study β, is Hyper-Rayleigh scattering (HRS). HRS is a nonlinear incoherent light scattering process that measures the hyperpolarizability β of molecules in solution [73]. It is a highly sensitive to symmetry technique [74]. Moreover it is an improved technique from the electric-field-induced second harmonic generation (EFISH) [75]. It can be performed in liquid phase without the need to apply an aligning electric field. Hyperpolarizability β value for charged chromophores and non-dipolar chromophores which have been dissolved in isotropic media can be determined. In addition, HRS has been successfully applied to study nonlinear optical properties of molecules [76], protein [77] and colloidal nanoparticles [78]. Octupolar chromophores are desirable because the second harmonic response is independent of the polarization of the incident light because of their highly isotropic property in comparison to dipolar chromophores [53]Additionally, the requirements of an octupolar molecule is to be non-centrosymmetric and a depolarization ratio (ρ) of $0 \geq 1 \leq 1.5$ [55, 74]. The symmetry observed in most octupoles is either D_{3h} or T_d however, D_2 and D_{2d} symmetry have also be observed to have strong NLO response [74].

1.6.1. Phthalocyanines nonlinear optical properties

Table 1.1 below shows a sample of know tetra-substituted Pcs that have been studied over the past years. Part A represent alpha-substituted Pcs with a substituent connected by an oxygen group, where only a few compounds have been investigated for their β, Im [$\chi^{(3)}$] and γ properties. Part B represent beta-substituted Pcs with various substituents and their NLO properties. Very few alpha tetra-substituted Pcs have been investigated for their NLO properties compared to beta- and/or octa-substituted Pcs.

Table 1.1: Known structural modifications of tetra-substituted Phthalocyanines

Part A

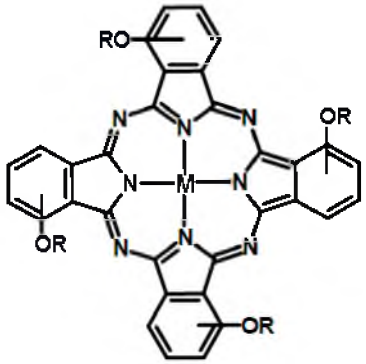

R-Groups	**Metal (M)**	**β (cm/MW^{-1})**	**Im [$\chi^{(3)}$] $\times10^{-11}$ (esu)**	**χ $\times10^{-27}$ (esu)**	**Source**
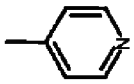	Lead (Pb)	130000	4.58	1.62	[19]
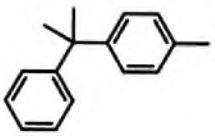	H_2	-			[22]
a) 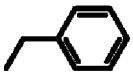 b) 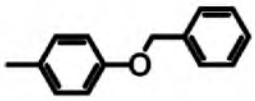 c) 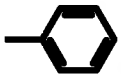 d) 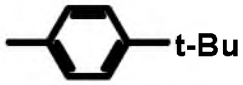	Titanium (Ti) (IV)	-			[79]

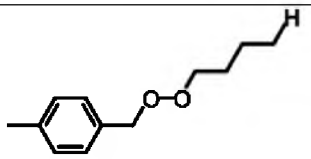	Zinc (Zn)	-			[80]
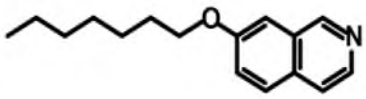	Zinc (Zn) Cobalt (Co)	-			[81]
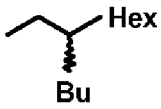	Zinc (Zn) Copper (Cu) Nickel (Ni) Cobalt (Co)				[82]
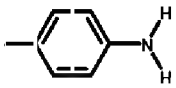	Indium (III) Chloride ($InCl_3$)	190000 (DMF)	6.25	2.93	[83]
		221600 (DMSO)	7.80	3.90	
Part B 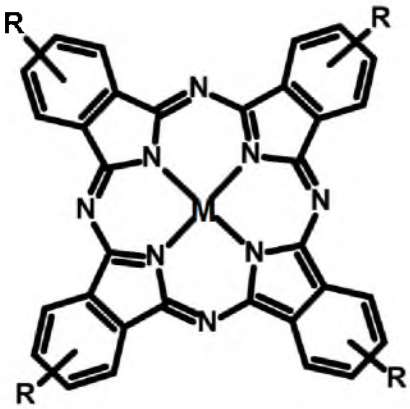					
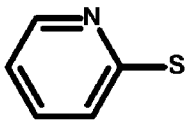	H_2	300000	7.04	1.99	[84]

	Zinc Zn (II)	372000	8.73	2.47	
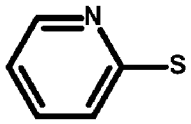	Indium (III) Chloride ($InCl_3$)	432000	1.97	5.58	[84]
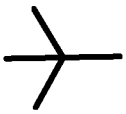		310000	-	-	[85]

In most studies, the NLO properties of tetra-substituted phthalocyanines have been studied as a mixture of possible positional isomers [86].

It has been reported that the second order NLO factor has symmetry restrictions [87], and is zero in centrosymmetric systems, whereas the third order NLO factor has no symmetry restrictions and can take place in any material possessing a highly polarizable delocalized π-system [88]. The optimization of the second order nonlinear absorption coefficient (β) has a direct impact on the macroscopic second order NLO response [89].

1.6.2. Binuclear Phthalocyanines Nonlinear Optical Properties

BiPcs offer higher or improved response coefficient and shorter response time. This is due to the structural fine-tuning that can be achieved by BiPcs i.e. the insertion of two metals in the metal centres (which lie slightly above the ring), the use of various substituents and the variation in lengths of the bridge/linker. The introduction of various bridges/linkers causes the rigidity or flexibility of the molecule and may result in more red-shifting of the Q-band as a

result of continuous π-conjugation. There have been reports of wavelength tuning of organic compounds to extend the RSA band [90].

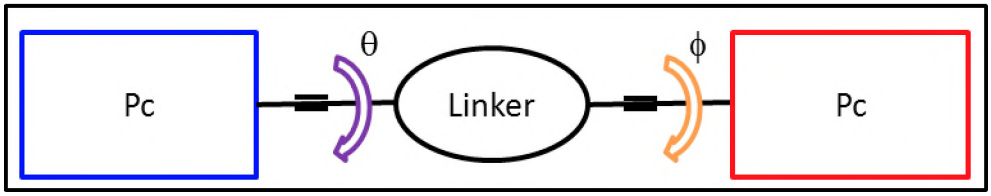

Figure 1.9: Structural representation showing angles (θ and ϕ) between two Pc units linked through a bridge.

Dynamic hyperpolarizability (β_λ), wavelength of the incident light, values of dimers have shown to depend sensitively on molecular structure [74]. **Figure 1.9** shows an adopted structure from Duncan *et al.* [74] which has specific angles used to calculate the β_λ values from HRS technique. This symmetry requires the molecule of interest to have $\boldsymbol{\theta \approx -\phi}$ **and** $\boldsymbol{\theta = -\phi = 45°}$ respectively, where these angles correspond to the torsional relationships between two Pc units. Symmetry of the molecule is essential in determining the octupolar/dipolar contributions of a chromophore. Chromophores which are more octupolar are desirable in NLO applications. NLO octupoles with either D_{3h} or T_d symmetry have been studied for NLO properties. These molecules are derived from cubic Td structure either by projection along a C_3 axis which gives rise to D_{3h} or D_3 symmetry, leading to D_{3h}, D_3, T_d and D_{2d} symmetry [91]. D_2 and D_{2d} symmetry have recently been discovered to have potential NLO response [74].

Table 1.2 below shows a sample of known tetra-substituted BiPcs that have been studied over the past years. Similar to **Table 1.1**, part A represents alpha-substituted BiPcs with substituents connected by an oxygen group. Part B represents Bis-Pcs with various substituents and their observed β coefficients.

Table 1.2: Known peripherally substituted structures of BiPcs and Bis-Pcs

Part A

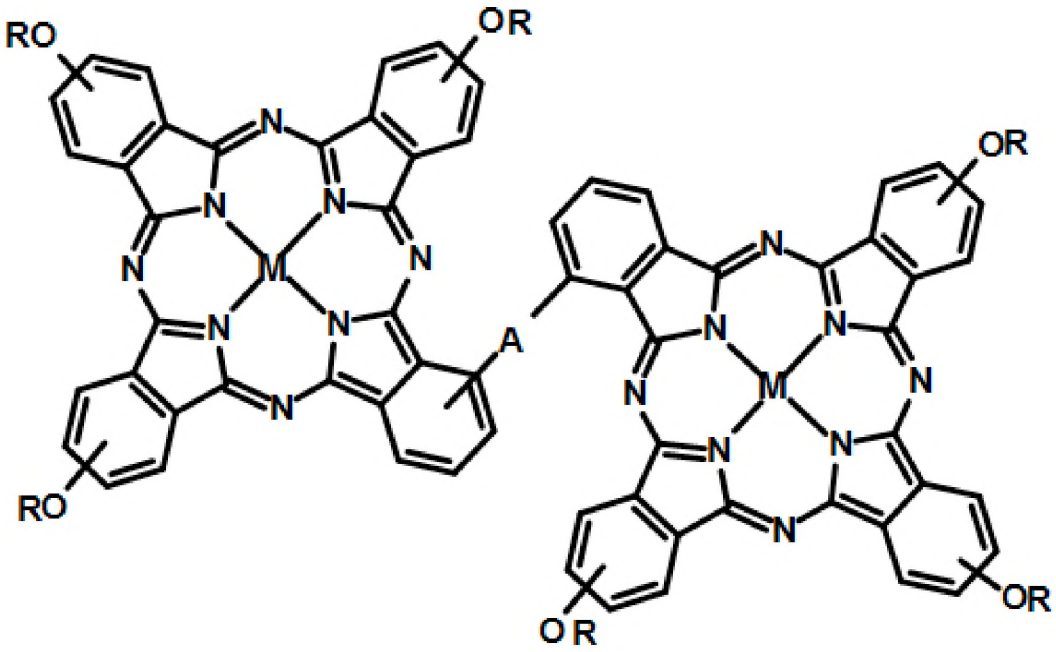

A-Linker	R-Groups	Metal	β (cm/MW^{-1})	Source
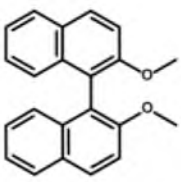	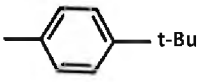	H_2	-	[92]
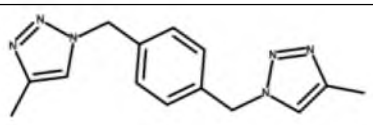	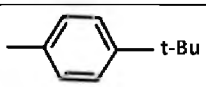	Zinc (Zn)	-	[92] [93]

Part B

Bisphthalocyanines

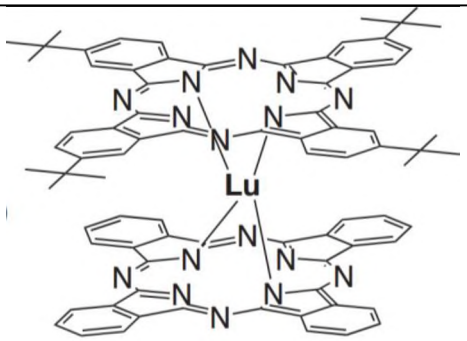	Lutetium (Lu)	5.56×10^{-10}	[94]
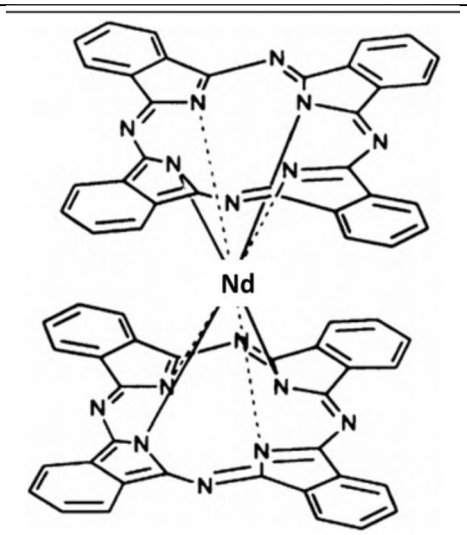	Neodymium (Nd)	420000	[95]
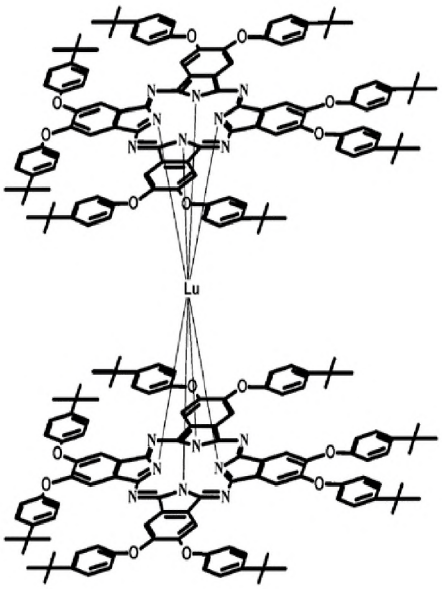	Lutetium (Lu)	a) 4.52×10^{-5} b) 9.23×10^{-6}	[96]

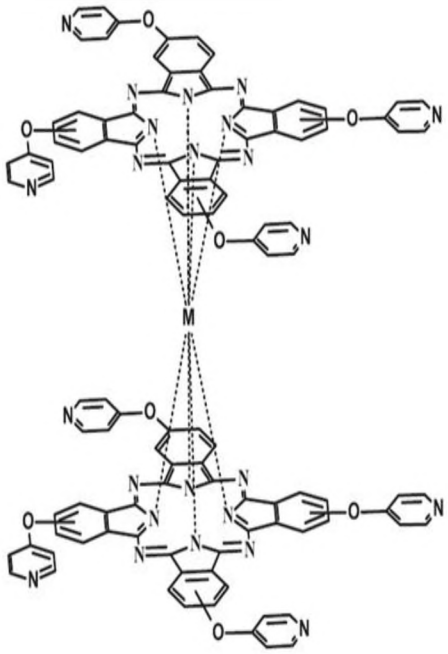	Lanthanum (La) Ytterbium (Yb)	1.12×10^{-6}	[97]

1.7. Instrumentation/Spectroscopic Characterisation

1.7.1. Magnetic Circular Dichroism

Magnetic Circular Dichroism (MCD) is a technique that can be used to assign spectra of porphyrinoids [98, 99]. Porphyrinoids include materials such as porphyrins, phthalocyanines, corroles and porphyrazines [98]. The mechanism of interest is understood when looking at the heteroaromatic nature of porphyrinoids ligands. The redox and spin states of the central metal, including the redox state of the π-system and the spectral band polarisation is the specific type of information that can be provided by the MCD technique. The dependence of MCD on the analysis of molecular orbital (MO) theory is a challenge because valence bond theory was more prevalent in organic and inorganic chemistry and was thus used extensively in porphyrinoid research [98]. In addition, valence bond theory is only used for visualising the framework of bonding and reactivity [98, 99]. On the other hand, MO theory is used for various aromatic properties which include benzene rings and heteroaromatic π-systems among others [98]. Therefore, MO theory accounts for a wide range of aromatic properties, it is more applicable to use than valence bond theory. The theoretical bases of MCD are the 5 electronic quantum numbers that is, principal quantum number (n), angular/orbital quantum number (l), magnetic quantum number (m_l), spin quantum number (s) and spin angular momentum (m_s). This is because the bases of the magnetic dipole moments associated with the orbital and spin motion of electrons is a result of the interaction of the electronic states with an applied magnetic field [98]. Between spin and orbital angular momentum the electron spin has been found to be more efficient in terms of producing a magnetic moment.

MCD is based on the absorption of circularly polarised light and subsequent formation of the excited state. MCD technique is distinct from NMR and EPR which are based on resonance between spin states [98]. MCD complements UV/vis spectroscopy by separating the Q_x and Q_y absorption bands. Q_x will absorb right-handed circularly polarised (rcp) light and Q_y left-handed

circularly polarised (lcp) light. The applied magnetic field lifts the degeneracy of the orbital and spin states that are in the same or opposite direction as the applied magnetic field. Circular dichroism (CD) spectroscopy is formed by the differential absorbance of lcp and rcp light. The difference in the intensity of lcp and rcp light is measured by MCD spectroscopy [98-100] where the selection rule for rcp is Δm= -1 and for lcp it is Δm= +1. Intensity of the total MCD can be represented by **Equation 7**:

$$I \sim A_1 \frac{-\partial f\ E}{\partial E} + B_0 + \frac{C_0}{kT} f\ E \qquad (7)$$

where E represents the energy coordinate in cm^{-1}, *f* refers to the normalized band shape function (normally assumed to be a Gaussian shaped curve). **Equation 7** takes into account the rigid-shift, Born-Oppenheimer and Franck-Condon approximations [95, 98].

The intensity of the MCD spectra is dependent on the coupling of the ground and excited states through the electric and magnetic dipole moments [101, 102]. From **Equation (7)** the letters A, B and C represent the contributions to the MCD spectra. These contributions are such that the *A* term **(Figure 1.10a)** depicts excited states and is independent of temperature. Moreover, it indicates the presence of a magnetic field which splits the excited states due to the Zeeman Effect. The *B* Term **(Figure 1.10b)** will arise from the mixing of closely related states that a linked by a magnetic dipole transition moment which can be positive or negative and is also independent of temperature. Furthermore, the *C* term **(Figure 1.10c)** depicts the orbital degenerate ground states which are highly dependent on temperature. Therefore, various complexes will either depict the *A* or *B* or *C* term depending on the type of symmetry they possess. Complexes with a lower symmetry than D_{4h} are known to give rise to the *B* term type of intensity [101,102]. For MPc complexes that adopt highly symmetrical and asymmetrical structures, the *A* term mechanism is likely to be observed as a result of accidental degeneracy of the split states.

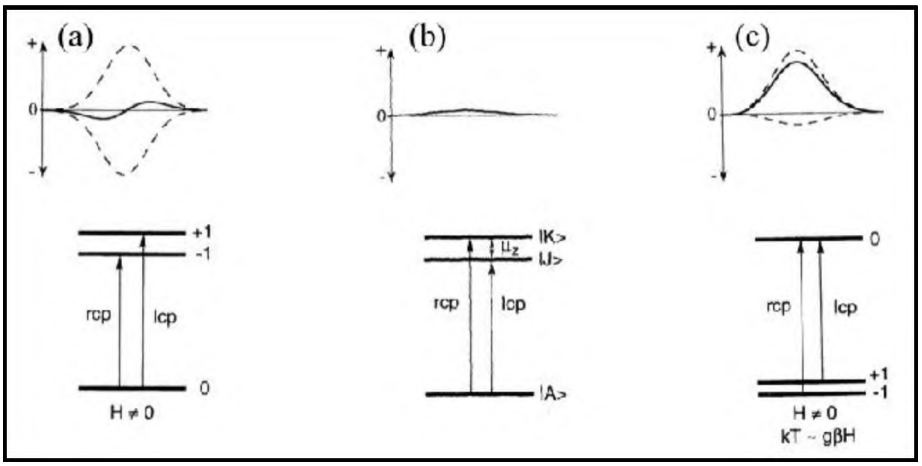

Figure 1.10: MCD mechanism illustrating *A*, *B* and *C* term respectively with the lcp and rcp represented by the dashed lines [100].

In **Figure 1.10a** and **Figure 1.11c**, the +1 and -1 represent the lcp and rcp respectively. In **Figure 1.10b** |A> represents the ground state, |J> is the excited state and |K> is the intermediate state. **Figure 1.11** shows a typical MCD and UV/vis spectra of Mg BiPc which shows a *B* term as an example.

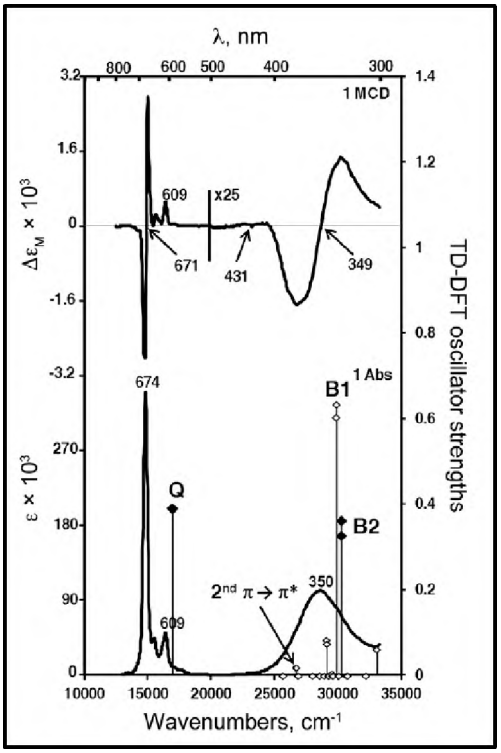

Figure 1.11: Electronic absorption and magnetic circular dichroism (MCD) of MgBiPc [101].

1.7.2. Time Correlated Single Photon Count (TCSPC)

1.7.2.1. Fluorescence

Fluorescence is one of the two processes of luminescence (the other process is phosphorescence). The Jablonski diagram **(Scheme 1.11)**, named after the father of fluorescence (i.e. Professor Alexander Jablonski) illustrates various energy levels in a phosphorescent molecule [103, 104]. Fluorescence is a radiative process which occurs from the singlet (S_1) excited state to the ground (S_0) state **(Scheme 1.9)** at ~10^{-8}s. Fluorescence typically occurs from aromatic molecules and its spectral data are generally presented as emission spectra [103].The emission spectra is dependent upon the chemical structure of the fluorophore and the nature of the media it has been dissolved in. Individual vibrational energy also contributes to the emission spectra [103].

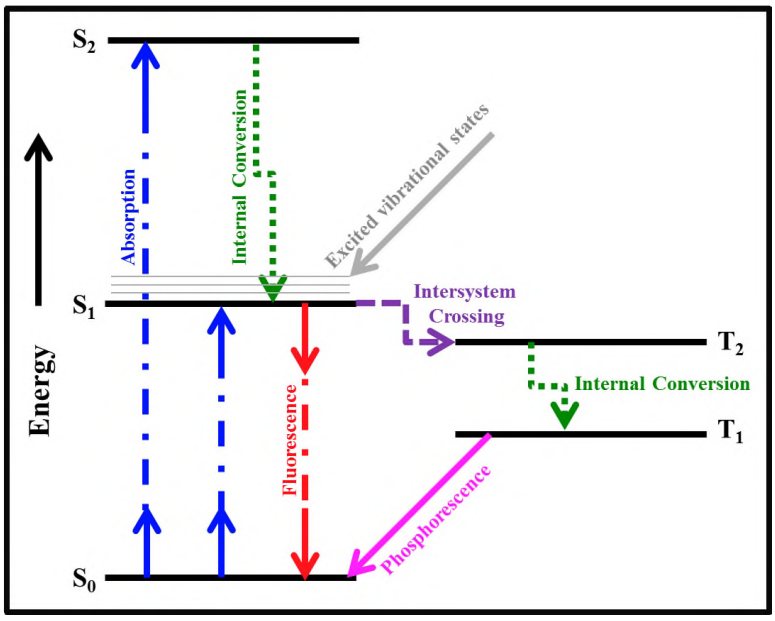

Scheme 1.11: Jablonski Diagram [104].

The emission spectrum is observed at lower energy or longer wavelength, when compared to absorption and excitation spectra. Kasha's rule indicates that the same emission spectrum is independent of the excitation wavelength [103]. Emission occurs strictly from the lowest singlet (S_1) state. Emission from the second (S_2) is not observed instead radiationless internal

conversion process takes place **(Scheme 1.11)**. The phenomenon of fluorescence is observed with the Stokes shift **(Figure 1.12)**. This is the difference between the maxima of the absorption and emission spectra which is approximately 10 nm. Stokes shift is usually observed when there is a lack of change in the environment surrounding the molecule. In this thesis Time Correlated Single Photon Count (TCSPC) technique is used to measure the emission and excitation spectra. **Figure 1.12** shows a typical excitation and emission spectra of an unmetalated Pc.

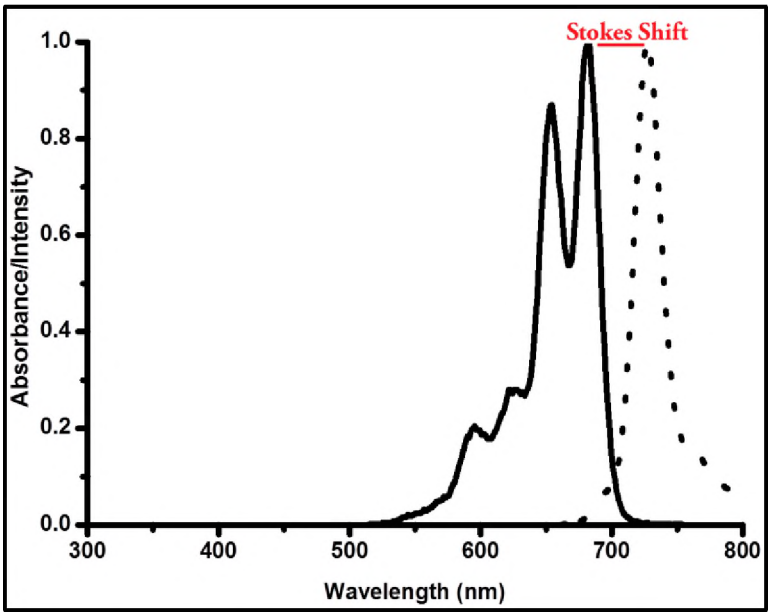

Figure 1.12: Excitation (solid line) and emission (dotted line) spectra illustrating a typical stokes shift [103].

TCSPC is also used to determine the fluorescence lifetime (τ) and fluorescence anisotropy (r) of a fluorophore, among various other energy processes. Fluorescence lifetime is defined as the average time between the fluorophores excitation and return to the ground state [103]. There are two types of fluorescence measurements namely, steady-state and time-resolved. The commonly used measurement is steady-state. Whereby the sample is illuminated with a continuous beam of light followed by subsequent recording of intensity and emission spectra. Time-resolved measurements have been commonly used to determine only lifetime decays in

phthalocyanine research. However, in this study the TCPSC technique is also used to measure rotational correlation times. Rotational correlation time (ϕ) of the molecule can be used to determine the size and shape of the molecule [103]. The rotational correlation time measurements are dependent on the viscosity of the solvent. The smaller the molecule, the faster it will rotate in solution. Conversely to steady-state, this measurement is performed by exposing the sample to a pulse of light, where the pulse width is typically shorter than the decay time of the sample [103]. Both measurements are achieved at the nanosecond timescale. TCSPC technique is becoming widely used because it has high sensitivity, dynamic range, data accuracy and precision [103].

Time-resolved emission spectra (TRES) is the emission spectra that represents the discrete times following excitation [105]. TRES can be used to separate emission spectra of two or more species in solution [106]. The multiple species can be as a result of different orientations and packing of the molecules. The spectra can be qualitative and/or quantitative and is plotted from TCSPC traces.

1.8. *Z*-scan

1.8.1. Measuring Nonlinear Optical Properties

Z-scan is a convenient and fast experimental method used to assess materials for NLO properties [107]. There are two properties to consider whether a material is an optical limiter or not [45], that is the material's nonlinear absorption coefficient and the nonlinear index of refraction [45] as descibed earlier. The *Z-scan* technique measures both the nonlinear index refraction (η) and the nonlinear absorption coefficient (β). *Z-scan* is a method that is highly senstive to all NLO mechanisms that give rise to change in the refractive index and/or absorption coefficient [108]. Slow nonlinearities such as population redistribution from linear absorption, reorientation of anisotropic molecules such as in CS_2, thermal refraction and electrostriction including higher order effects, are properties which can be studied by that *Z-scan* technique [108]. To distinguish between the two measurements an aperture is added or removed from the front of the probe detector **(Figure 1.13)**. When the aperture is added, the nonlinear index refraction is measured. Conversely, when the aperture is removed, the nonlinear absorption coefficient is measured. These measurements are of the total transmittance through the sample as a function of incident laser intensity while the sample is gradually moved through the focus of a lens (along the *z*-axis). There are different orders of susceptibilities [$\chi^{(n)}$] that govern the different processes that occur when the laser interacts with the sample [61]. These are $\chi^{(1)}$ for two-wave interactions, $\chi^{(2)}$ for three-waves, $\chi^{(3)}$ for four-waves, etc. They describe the waves which enter and leave the mediums respectively where energy, momentum and angular momentum are conserved during the interactions. However, $\chi^{(3)}$ describes a nonlinear process where the exiting and incident wave are of the same frequency [61]. The intricate details of this procedure were described by Sheik-Bahae *et al.*,[109]. For the purpose of this study the imaginary component of the third order susceptibility (Im [$\chi^{(3)}$]) and the hyperpolarizability (γ) will be determined.

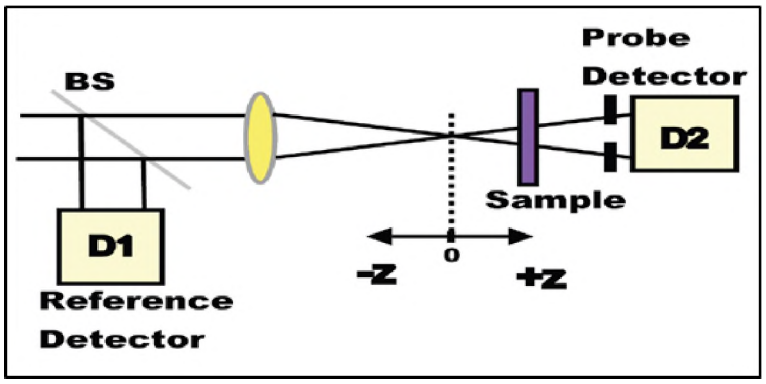

Figure 1.13: Typical diagram of a *Z-scan* setup [45].

Figure 1.14 shows a combination of the common spectrum observed for *z*-scan measurements of nonlinear material. A single valley curve in **Figure 1.14** shows a typical transmittance signal for NLO material. A double valley curve spectra **(Figure 1.14)** shown by triangles and black dots are not commonly observed. The single valley curve is as a result of the excited state absorption of the nonlinear material being large compared to the ground state absorption which is known as reverse saturable absorption (RSA).

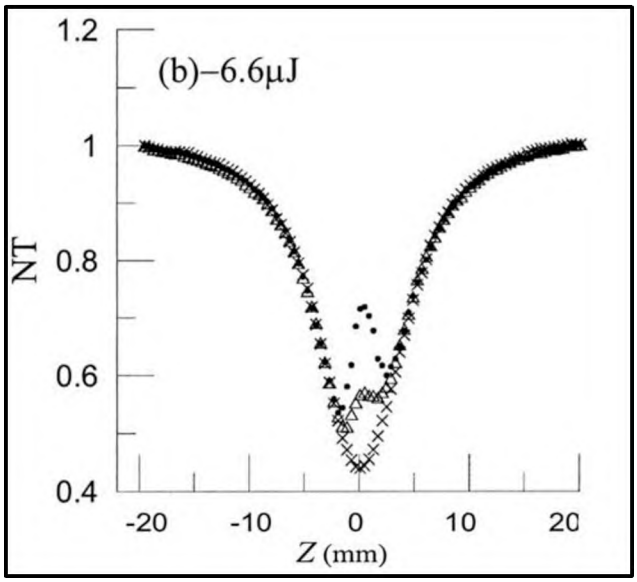

Figure 1.14: Typical *z*-scan spectra illustrating single and double valley curves [110].

The double valley curve was observed by Chang *et al.* [110] for a chloroaluminium phthalocyanine. The double valley curve was explained to be due to solute molecules being

pushed from the laser beam center towards the boundary and subsequent diffusion of molecules back into their ground state where there is a probability of getting re-excited [107].

1.8.2. Theoretical background for *Z*-scan application

The experimental second order NLO parameter is determined by measuring the normalised transmittance from an open aperture *z*-scan experiment. The normalised transmittance is given by **Equation 8** [111, 112]:

$$T_n\ z_s = \frac{1}{Aq_0\ Z_s} \int_{-\infty}^{+\infty} \ln[1 + q_0\ z_s\ f(\tau)]d\tau \quad (8)$$

where $f(\tau)$ is a function of time describing the temporal profile of the pulse for Gaussian pulses and has the form $f\ \tau = e^{(-\tau^2)}$. A is a normalization constant equal to $\int_{-\infty}^{+\infty} f\ \tau\ d\tau$ and $q_0(z_s)$ is a parameter characterizing the strength of the nonlinearity. When a circular Gaussian beam is used, q_0 is represented by **Equation 9** [113, 114]:

$$q_0\ z_s = \frac{2\beta P_0 L_{eff}}{\pi w^2(z_s)} \quad (9)$$

where β is the nonlinear absorption coefficient of the material, P_0 is the peak power of the pulses and the L_{eff} the effective propagation length in the material, given by the relation:

$$L_{eff} = \frac{1-e^{-(\alpha L)}}{\alpha} \quad (10)$$

where L is the sample length (or the thickness of the sample respectively) and α is the linear absorption coefficient. α is determined using **Equation 11**:

$$\alpha = \frac{h\nu}{N}\beta \quad (11)$$

where N corresponds to the number of active species per unit volume, h is Planck's constant and ν the frequency of a laser excitation. The parameter $w(z_s)$ (in **Equation 9**) is the beam

width at the sample plane defined as the distance from the beam centre to the point where the intensity reduces to $1/e^2$ of its axis value. $w(z_s)$ and is defined by **Equation 12** [111]:

$$w\ z_s = w_0 \sqrt{1 + \frac{z_s - z_0}{z_R}^2} \quad (12)$$

where w_0 is the beam width at the focal point and z_0 is the location of the beam focus. The parameter z_R is the Rayleigh length, defined by **Equation 13**:

$$z_R = \frac{\pi w_0^2}{\lambda} \quad (13)$$

where λ is the beam wavelength. **Equations (8)-(13)** are used to determine the nonlinear absorption coefficient (β) from experimentally measured transmittance. Tsigaridas et al. [111] produced an analytical formula, which is provided as **Equation 14:**

$$q_0\ z_s = \begin{cases} a_0 + a_1 T_n\ z_s + a_2 T_n^2\ z_s + a_3 T_n^3\ z_s & \text{for } T_n\ z_s \leq 0.75 \\ c_0 + c_1\ T_n\ z_s\ ^{c_2} & \text{for } T_n\ z_s \geq 0.75 \end{cases} \quad (14)$$

where the coefficients a_0, a_1, a_2, a_3, c_0, c_1, c_2 for Gaussian pulses are given as 15.66, -37.45, 30.76, -8.97, -2.301, 2.156, -1.563, respectively [111]. **Equation 14** provides the $q_0\ z_s$ values directly from the normalized transmittance $T_n(z_s)$. The authors demonstrated that their technique enables the straightforward determination of β and is very robust to the presence of signal noise [111]. The absorption coefficient (β), as well as the beam parameters Z_0 and Z_R can be determined from the $q_0(z_s)$ values obtained from **Equation 14**. Substituting **Equation 12** into **Equation 8**, $q_0\ z_s$ is then defined by **Equation 15**:

$$q_0\ z_s = \frac{Q_0}{1+(z_s - z_0)^2/z_R^2} \quad (15)$$

where:

$$Q_0 = \frac{2\beta P_0 L_{eff}}{\pi w_0^2} = \frac{2\beta P_0 L_{eff}}{\lambda z_R} \quad (16)$$

Equation 14 gives a Gaussian plot with Q_0 as the maximum value at the beam waist ($z_s = z_0$). The full width at half maximum (FWHM) of the $q_0(z_s)$ is equal to $2z_R$. The peak value and the FWHM of the plot provides the values for Q_0 and Z_R. **Equation 17** is then used to calculate the nonlinear absorption coefficient (β).

$$\beta = \frac{\lambda z_R Q_0}{2P_0 L_{eff}} \quad (17)$$

The imaginary component of the third order optical susceptibility $Im[\chi^{(3)}]$ is directly proportional to β via **Equation 18** [115]:

$$Im[\chi^{(3)}] = \frac{(n^2 \varepsilon_0 c \lambda \beta)}{(2\pi)} \quad (18)$$

in which c and n, respectively, are the speed of light in a vacuum and the linear refractive index of the system. ε_0 is the permittivity of free space and λ is the wavelength of the laser light. At a molecular level, there is a direct correlation of $Im[\chi^{(3)}]$ with the hyperpolarizability, γ, which provides the nonlinear absorption per mole of the sample via the relationship shown by **Equation 19** [116, 117]:

$$\gamma = \frac{Im[\chi^{(3)}]}{N^* f^4} \quad (19)$$

where $N^* = C_{mol} N_A$ (with C_{mol} being the concentration in mol) and f represents Lorenz local field factor and is given by **Equation 20**:

$$f = \frac{n^2 + 2}{3} \quad (20)$$

1.9. Theoretical/Computer Modelling

1.9.1. Density Functional Theory and Time Dependent Density Functional Theory calculations

Density functional theory (DFT) has proven to be an extremely reliable and useful computational technique for the study of aromatic compounds such as porphyrins, phthalocyanines and their derivatives [68]. It constitutes a valid tool which complements the previous computational approaches adopted for the study of such aromatic compounds [68]. The first static hyperpolarizability (β_{ijk}) of a 3×3×3 matrix with 10 components is calculated by performing DFT calculations according to literature methods [118]. The magnitude of the effective hyperpolarizability is determined from β_{ijk} using **Equation 21** [118] which is the first method used for calculating β values.

$$\beta_{eff} = \left(\beta_{xxx} + \beta_{xyy} + \beta_{xzz} \right)^2 + \left(\beta_{yyy} + \beta_{yzz} + \beta_{yxx} \right)^2 + \left(\beta_{zzz} + \beta_{zxx} + \beta_{zyy} \right)^2 \Big)^{1/2} \quad (21)$$

Since the β_{ijk} values that are provided by the Gaussian 03 software are reported in Debye, $Å^2$, the calculated β_{eff} values are converted to electrostatic units (esu), ($1Å^2 = 1 \times 10^{-30}$ esu).

In this work the electronic structures of Pcs and BiPcs have been calculated using DFT methods in order to investigate a combined analysis of the optical spectral data. The method applied in DFT is Becke three-parameter Lee-Yang-Parr (B3LYP) using the basis set 6-31G (d)/SDD which is a commonly used hybrid function for optimization. The results of the DFT calculations are used to characterise the physical properties of the Pcs and BiPcs.

1.9.2. Dipolar vs. Octupolar

DFT can be used to calculate the dipolar and/or octupolar contributions **(Figure 1.15a)** and the anisotropy parameter **(Figure 1.15b)** of each molecule. DFT calculation of hyper-Rayleigh Scattering (HRS) response coefficient (β_{HRS}) was carried out in order to calculate the first static hyperpolarizability, following literature method [54-59]. The advantage of this method is that octupolar and dipolar second order NLO contributions are theoretically separated. The values of both dipolar ($\beta_{J=1}$) and octupolar ($\beta_{J=3}$) are known to be significantly influenced by the number of electrons in the system [54]. Due to symmetry constraints there is no permanent dipole moment for octupolar molecules [58], hence octupolar molecules present an isotropic β tensor.

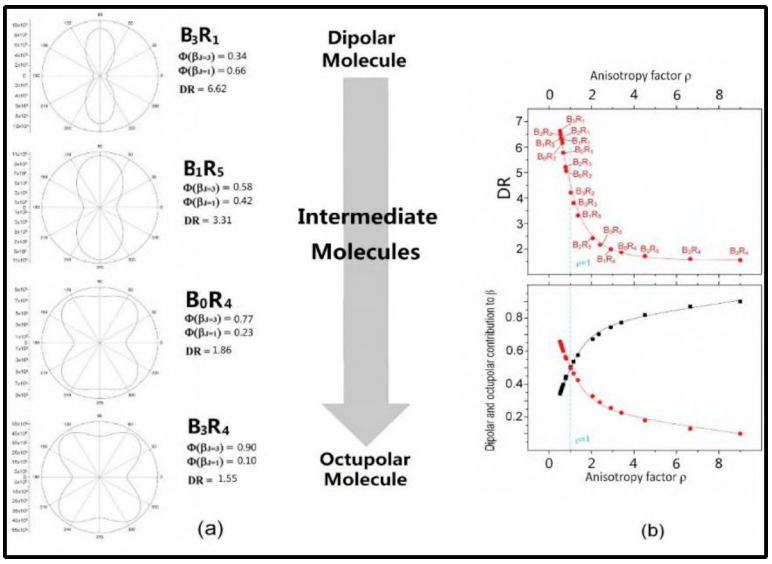

Figure 1.15: (a) Harmonic light intensity as a function of the polarization angle Ψ by polar representation, (b) Evolution of depolarisation ratio (ρ) as well as the octupolar [ϕ ($\beta_{J=3}$)] and dipolar [ϕ ($\beta_{J=1}$)] contributions to the second-order NLO response as a function of anisotropy factor [55]

It is to be noted that the equations presented below are only valid in the off-resonance region. The following equations were used to calculate the (β_{HRS}) response and to determine the

polarization angle by polar representation. In **Equation 22**, β_{ZZZ}^2 and β_{ZXX}^2 are the orientation average of the molecular β tensor components. Simulation of the plots was achieved by the DFT calculations. This is the second method used to calculate the β values.

$$\beta_{HRS}\ -2\omega;\ \omega,\omega\ =\ \beta_{ZZZ}{}^2\ +\ \beta_{ZXX}{}^2\ \ ^1{}_2 \qquad (22)$$

where $\beta_{ZZZ}{}^2$ and $\beta_{ZXX}{}^2$ are the orientational average of the molecular β tensor components, which can be calculated using the following equations:

$$\beta_{ZZZ}{}^2\ =\frac{1}{7}\ \ {}^{x,y,z}_{\zeta}\beta_{\zeta\zeta\zeta}{}^2+\frac{6}{35}\ \ {}^{x,y,z}_{\zeta\neq\eta}\beta_{\zeta\zeta\zeta}\beta_{\zeta\eta\eta}+\frac{9}{35}\ \ {}^{x,y,z}_{\zeta\neq\eta}\beta_{\eta\zeta\zeta}{}^2+\frac{3}{35}\ \ {}^{x,y,z}_{\zeta\neq\eta\neq\xi}\beta_{\eta\zeta\zeta}\beta_{\eta\xi\xi}+$$

$$\frac{2}{35}\ \ {}^{x,y,z}_{\zeta\neq\eta\neq\xi}\beta_{\zeta\eta\xi}{}^2 \qquad (23a)$$

$$\beta_{ZXX}{}^2\ =\frac{1}{35}\ \ {}^{x,y,z}_{\zeta}\beta_{\zeta\zeta\zeta}{}^2-\frac{2}{105}\ \ {}^{x,y,z}_{\zeta\neq\eta}\beta_{\zeta\zeta\zeta}\beta_{\zeta\eta\eta}+\frac{11}{105}\ \ {}^{x,y,z}_{\zeta\neq\eta}\beta_{\eta\zeta\zeta}{}^2-\frac{1}{105}\ \ {}^{x,y,z}_{\zeta\neq\eta\neq\xi}\beta_{\eta\zeta\zeta}\beta_{\eta\xi\xi}+$$

$$\frac{4}{105}\ \ {}^{x,y,z}_{\zeta\neq\eta\neq\xi}\beta_{\zeta\eta\xi}{}^2 \qquad (23b)$$

In addition, the molecular geometric information is given by the depolarization ratio (DR), which is expressed by $DR=\ \beta_{ZZZ}{}^2\ \ \beta_{ZXX}{}^2$.

To clarify the nature of the symmetric Rank-3 β tensor, $\beta_{HRS}{}^2$ can be decomposed as the sum of the dipolar $\beta_{J=1}$ and octupolar $\beta_{J=3}$ tensorial components [58], which are expressed as:

$$\beta_{HRS}=\ \overline{\beta_{HRS}{}^2}\ =\ \overline{\frac{10}{45}\ \beta_{J=1}{}^2+\frac{10}{105}\ \beta_{J=3}{}^2} \qquad (24)$$

$$\beta_{J=1}{}^2=\frac{3}{5}\ \ {}^{x,y,z}_{\zeta}\beta_{\zeta\zeta\zeta}{}^2+\frac{6}{5}\ \ {}^{x,y,z}_{\zeta\neq\eta}\beta_{\zeta\zeta\zeta}\beta_{\zeta\eta\eta}+\frac{3}{5}\ \ {}^{x,y,z}_{\zeta\neq\eta}\beta_{\eta\zeta\zeta}{}^2+\frac{3}{5}\ \ {}^{x,y,z}_{\zeta\neq\eta\neq\xi}\beta_{\eta\zeta\zeta}\beta_{\eta\xi\xi} \qquad (25a)$$

$$\beta_{J=3}{}^2=\frac{2}{5}\ \ {}^{x,y,z}_{\zeta}\beta_{\zeta\zeta\zeta}{}^2-\frac{6}{5}\ \ {}^{x,y,z}_{\zeta\neq\eta}\beta_{\zeta\zeta\zeta}\beta_{\zeta\eta\eta}+\frac{12}{5}\ \ {}^{x,y,z}_{\zeta\neq\eta}\beta_{\eta\zeta\zeta}{}^2-\frac{3}{5}\ \ {}^{x,y,z}_{\zeta\neq\eta\neq\xi}\beta_{\eta\zeta\zeta}\beta_{\eta\xi\xi}+\ \ {}^{x,y,z}_{\zeta\neq\eta\neq\xi}\beta_{\zeta\eta\xi}{}^2$$

(25b)

Then, the nonlinear anisotropy parameter $\rho = \beta_{J=3} \quad \beta_{J=1}$ is employed to evaluate the ratio of the octupolar $\phi_{J=3} = \rho \quad 1+\rho$ and dipolar $\phi_{J=1} = 1 \quad 1+\rho$ contribution to the hyperpolarizability tensor.

Furthermore, assuming a general elliptically polarized incident light propagating along the X direction, the intensity of the harmonic light at the 90° along the Y direction and vertically (V) polarized along the Z axis are given by Bersohn's expression [58]:

$$I_{\Psi V}^{2\omega} \alpha \ \beta_{ZXX}{}^2 \ cos^4\Psi + \beta_{ZZZ}{}^2 \ sin^4\Psi + sin^2\Psi cos^2\Psi \times (\beta_{ZXZ} + \beta_{ZZX})^2 - 2\beta_{ZZZ}\beta_{ZXX} \tag{26}$$

where the orientational averages $(\beta_{ZXZ} + \beta_{ZZX})^2 - 2\beta_{ZZZ}\beta_{ZXX}$ is expressed as:

$$\beta_{ZXZ} + \beta_{ZZX}{}^2 - 2\beta_{ZZZ}\beta_{ZXX} = 7\ \beta_{ZXX}{}^2 - \beta_{ZZZ}{}^2 = \frac{2}{35} \sum_{\zeta}^{x,y,z} \beta_{\zeta\zeta\zeta}{}^2 - \frac{32}{105} \sum_{\zeta\neq\eta}^{x,y,z} \beta_{\zeta\zeta\zeta}\beta_{\zeta\eta\eta} + \frac{10}{21} \sum_{\zeta\neq\eta}^{x,y,z} \beta_{\eta\zeta\zeta}{}^2 - \frac{16}{105} \sum_{\zeta\neq\eta\neq\xi}^{x,y,z} \beta_{\eta\zeta\zeta}\beta_{\eta\xi\xi} + \frac{22}{105} \sum_{\zeta\neq\eta\neq\xi}^{x,y,z} \beta_{\zeta\eta\xi}{}^2 \tag{27}$$

1.10. Aims of Thesis

1.10.1. To synthesise non-peripherally substituted metal-free and nickel isomeric *tert*-butylphenoxy phthalocyanines **(Figure 1.16)** and novel binuclear phthalocyanines **(Figure 1.17)**.

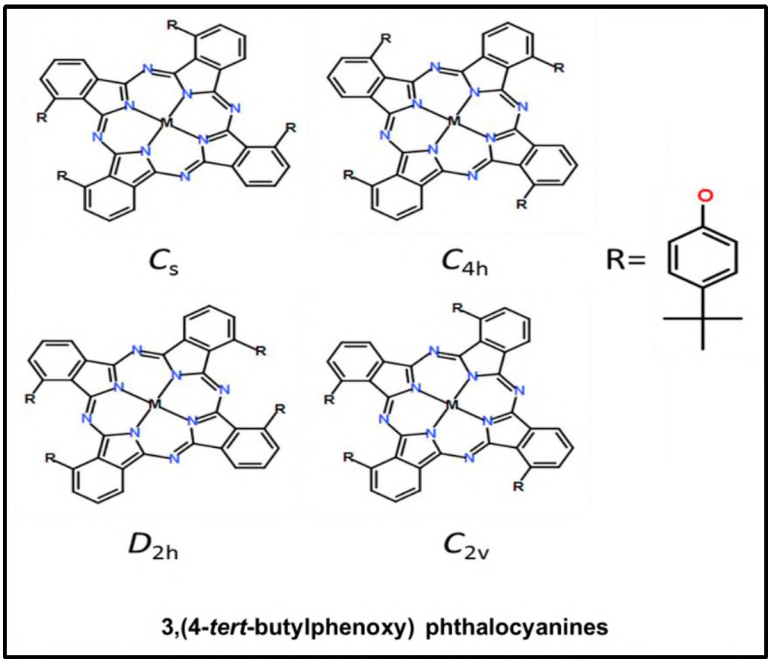

Figure 1.16: The synthesised 3-(4-*tert*-butylphenoxy) phthalocyanine isomers.

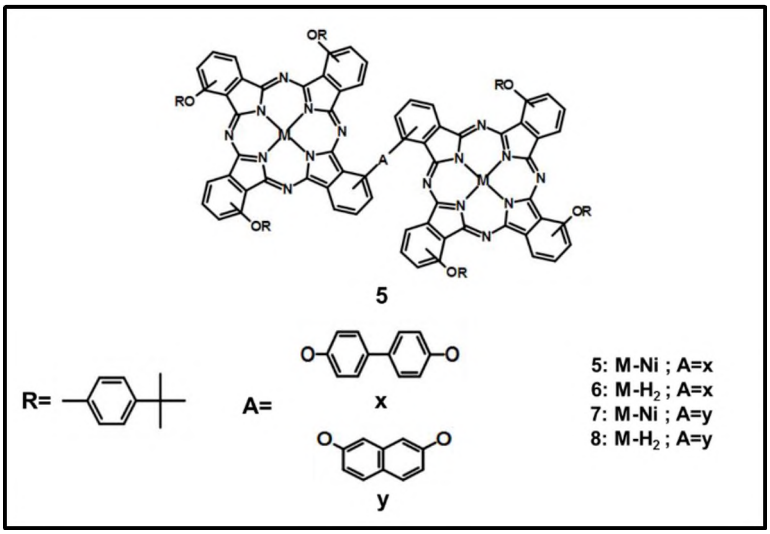

Figure 1.17: The synthesised Biphenyl and Naphthyl linked binuclear phthalocyanines.

1.10.2. To study the spectroscopic properties of the synthesised complexes.

1.10.3. Use DFT calculations to explain the spectroscopic and nonlinear optical properties of these complexes.

1.10.4. To study the nonlinear optical properties of each synthesised compound for nonlinear related application.

Chapter 2

Experimental

2. Experimental

2.1 Materials

The following chemicals were purchased from Sigma-Aldrich 4-*tert*-butylphenol, 3-nitrophthalic acid, formamide, thionyl chloride, 4-aminophthalonitrile, terephthalaldehyde, p-phenylenediamine, terephthalaldehyde, 4,4'-dihydroxybiphenyl, 2,7-dihydroxynaphthalene, lithium metal, nickel (II) acetate tetrahydrate (98%), 1,8-diazabicyclo[5,4,0] undec-7-ene (98%) (DBU), anhydrous 1, 2-dichlorobenzene, silica gel (with high-purity grade pore size 60Å 70-230 mesh 63-200μm for column chromatography), deuterated chloroform ($CDCl_3$) and dimethyl sulfoxide (DMSO-d6). Saarchem-Merck supplied us with anhydrous potassium carbonate, 32% hydrochloric acid (was used to prepare 1M stock solution), 32% ammonia solution, tetrahydrofuran (THF), chloroform, acetone, methanol, and hexane. *N, N*-dimethylformamide (DMF) was kept dry over molecular sieves before use, toluene, 1-octanol, acetic acid, dichloromethane (DCM) were purchased at Beckman/B & M Scientific. BDH laboratory reagents supplied acetonitrile. Bio-Rad Laboratories and Minema supplied bio-beads S-X1 with 200-400 mesh for gel permeation chromatography for size exclusion and 98% sulphuric acid respectively.

2.2 Equipment/Instrumentation

Electronic absorption spectra were recorded on a Shimadzu UV-2550 spectrophotometer. Magnetic circular dichroism (MCD) spectra were measured on a Chirascan Plus spectropolarimeter equipped with a permanent magnet, which produces a magnetic field of 1T (1 tesla). A solid state large area avalanche photodiode (LAAPD) was used as the detector. Fluorescence lifetimes were measured with a FluoTime 300 EasyTau spectrometer (PicoQuant GmbH) using a time correlated single photon counting (TCSPC) technique. The samples were excited at 670 nm with a diode laser (LDH-P-670, 20 MHz repetition rate, 44 ps pulse width, PicoQuant GmbH). The detector employed was a Peltier cooled photomultiplier (PMA-C 192-M, PicoQuant GmbH). Mass spectral data were collected on a Bruker AutoFLEX III smart-beam MALDI-TOF mass spectrometer using α-cyano-4-hydroxycinnamic acid as the matrix in positive ion mode.

All Z-scan experiments described in this study were performed using a frequency-doubled Nd:YAG laser (Quanta-Ray, 1.5 J/10 ns fwhm pulse duration) as the excitation source. The laser was operated in a near Gaussian transverse mode at 532 nm (second harmonic), with a pulse repetition rate of 10 Hz and an energy range of 0.1 μJ – 0.1 mJ, which was monitored with an energy detector (Coherent J5-09). The low repetition rate of the laser prevents cumulative thermal nonlinearities. The beam was spatially filtered to remove the higher order modes and tightly focused with a 15 cm focal length lens. No damage was detected between runs when the sample was moved or replaced. Ultra-violet photoemission spectroscopy (UPS) measurements were carried out in a Kratos Axis Ultra DLD system (Kratos Analytical, Manchester UK), with a base pressure in the analysis chamber of approximately 2×10^{-10} mbar. The sample was illuminated with He I (alpha) emission (21.2 eV) from a double differentially-pumped Kratos Vacuum Ultraviolet Source. Photoelectrons ejected from a 110 micrometer area

of the sample were collected using the delay line detector at a pass energy of 5 eV and a step size of 0.01 eV.

Solid state UV/vis absorption spectra were measured using a Perkin Elmer LAMBDA 25. Isomer thin films were formed by spin coating from 1,2-dichlorobenzene onto Quartz substrates.

The Gaussian 03 software package [119] running on an Intel/Linux cluster was used to perform a series of B3LYP geometry optimizations with 6-31G(d) and SDD basis sets. Gaussview 4.1 was used for all visualizations of molecular orbitals (MOs) and properties [119]. The B3LYP exchange-correlation density functional employs Becke's method for using Lee–Yang Parr's gradient-correction, which includes a hybrid of semi-empirical Hartree–Fock and DFT exchange. B3LYP/6-31G(d) formalism was used to perform single-point energy calculations to determine the NLO response (β), following literature methods [118]. TD-DFT calculations were carried out using the CAM-B3LYP functional of the Gaussian 09 software package with 6-31G(d) basis sets [120].

2.3. Synthesis

2.3.1. Synthesis of phthalonitriles

2.3.1.1. Synthesis of 3-nitrophthalonitrile (5)

A multi-step synthetic procedure which has the steps below was followed for the synthesis of 3-nitrophthalonitrile.

3-Nitrophthalic anhydride

3-nitrophthalic acid (52.8 g; 0.25 mol) dissolved in acetic anhydride (50 mL) were stirred in a reflux condenser. The mixture was heated gently until 3-nitrophthalic acid had completely dissolved then left to boil for 5-10 minutes. Reacted mixture was poured into a porcelain dish and allowed to cool to form crystals. 3-nitrophthalic anhydrid (i.e. crystal product) was thoroughly grounded with a mortar then filtered under suction while being washed with diethyl ether. The 3-nitrophthalic anhydride was left overnight to dry in the oven at 105°C. IR [(KBr) ν_{max}/cm^{-1}]: 1856, 1772 (C=O); 1541 ($-NO_2$); 1263, 1222 (C-O-C).

3-Nitrophthalimide

A suspension of 3-nitrophthalic anhydride (12.5 g; 0.064 mol) in formamide (20 mL) was refluxed at 210°C for 3 hours. After the reaction mixture was cooled to room temperature, it was filtered and washed with water then dried overnight at 110°C. IR [(KBr) ν_{max}/cm^{-1}]: 3159, 3075 (N-H); 1771, 1703 (C=O); 1531 ($-NO_2$).

3-nitrophthalamide

3-nitrophthalimide (11.8 g; 0.061 mol) was stirred in 32% ammonium solution (30 mL) for 24 hours at room temperature. The resulting white product was filtered off under reduced pressure and washed four times with 200 mL of cold deionised water. The solid white product was then dried overnight in the oven at 110°C. IR [(KBr) ν_{max}/cm^{-1}]: 3419, 3294, 3198, 3103 (N-H); 1662, 1619 (C=O); 1532 ($-NO_2$).

3-Nitrophthalonitrile

Dry DMF (60 mL) was stirred under nitrogen gas while thionyl chloride (36 mL) which was kept at 0°C, was slowly poured into the reaction vessel. After 2 hours, 3-nitrophthalamide (10.2 g; 0.048 mol) was added to the reaction mixture and stirred for 3 hours at room temperature. 3-nitrophthalonitrile (final product) was added to 200 g ice. The white product was then filtered, washed with cold water then dried at 65°C overnight. Yield: 6.43 g (14.9%); IR [(KBr) ν_{max}/cm^{-1}]: 2232 (C=N), 2967, 2875, (C-H); 1538 ($-NO_2$); Elemental: expected values (%) C: 54.90, H: 2.90, N: 24.00; results (%) C: 55.08, H: 1.25, N: 24.05.

2.3.1.2. Synthesis of 3-(4-*tert*-butylphenoxy) phthalonitrile (7)

Following a literature method [79, 121], at room temperature 4-*tert*-butylphenol (840 mg; 6.11 mmol) and 3-nitrophthalonitrile (1580 mg; 6.11 mmol) were dissolved in dry DMF (10 mL). In addition, anhydrous K_2CO_3 (2010 mg) was slowly added while stirring the reaction mixture. After 4 hours of stirring, an additional anhydrous K_2CO_3 (1030 mg) was added portion-wise every 15 minutes. After 24 hours total reaction time, 1M HCl (50 mL) was added to the reaction mixture to encourage the formation of a precipitate. The reaction was than filtered and recrystallized in methanol and water (1:0.5) to yield a pale white product **(7)**. Yield: 1.23 g (72.7%); IR [(KBr) ν_{max}/cm^{-1}]: 2232 (C=N), 2967, 2875, (C-H); 3094 (=CH); Elemental: expected values (%) C: 78.23, H: 5.84, N: 10.14; results (%) C: 78.22, H: 6.32, N: 10.08.

2.3.1.3. Synthesis of bisorthodinitrile (10)

Following a literature method [122], the Dean and Stark distilling trap was fitted onto a flask which contained 4-aminophthalonitrile (1060 mg; 7.38 mmol), terephthalaldehyde (470 mg; 3.69 mmol) and toluene (25 mL). The mixture was heated overnight at approximately 110°C. After cooling the reaction it resulted in the formation of a yellow precipitate which was filtered and washed with toluene then allowed to dry. The product was then extracted using hot acetonitrile and filtered. The filtrate was placed in an ice bath to encourage the formation of a precipitate.

The precipitate was recrystallized using hexane to afford a yellow product, bisorthodinitrile. Yield: 1.01g (75.4%); IR [(KBr) ν_{max}/cm^{-1}]: 2230 (C=N), 1624, 1586 (R_2C=N-R); Elemental: expected values (%) C: 74.99, H: 3.15, N: 21.86; results (%) C: 73.21, H: 3.19, N: 21.74.

2.3.1.4. Synthesis of 3-[4-[4-(2,3-dicyanophenoxy)phenyl]phenoxy]phthalonitrile (12a')

Under nitrogen gas, 3-nitrophthalonitrile (470 mg, 2.71 mmol) and 4, 4'-dihydroxybiphenyl (250 mg, 1.35 mmol) were dissolved in dry DMF (10 mL) at room temperature. In addition, anhydrous K_2CO_3 (1510 mg) was slowly added while stirring the reaction mixture. After 4 hours of stirring, an additional anhydrous K_2CO_3 (2000 mg) was added portion-wise every 15 minutes. After 24 hours total reaction time, 1M HCl (50 mL) was added to the reaction mixture to encourage the formation of a precipitate. The reaction was than filtered and recrystallized in methanol and water (1:0.5) to yield a pale white product **(12a')**. Yield: 0.52 g (87%); IR [(KBr) ν_{max}/cm^{-1}]: 1209, 1278 (C-O-C stretch); 1492 (CH_3 bend); 1573 (CH_2 bend); 2230 (C≡N stretch); Elemental: expected values (%) C: 76.7, H: 3.2, N: 12.8; results (%) C: 76.78, H: 3.19, N: 12.79.

2.3.1.5. Synthesis of 3-[7-(3,4-dicyanophenoxy)-2-naphthyl]oxy]phthalonitrile (12b')

Under nitrogen gas, 3-nitrophthalonitrile (470 mg, 2.70 mmol) and 2,7-dihydroxynaphthalene (220 mg, 1.25 mmol) were dissolved in dry DMF (10 mL) at room temperature. In addition, anhydrous K_2CO_3 (1.51 g) was slowly added while stirring the reaction mixture. After 4 hours of stirring, an additional anhydrous K_2CO_3 (2.00 g) was added portion-wise every 15 minutes. After 24 hours total reaction time, 1M HCl (50 mL) was added to the reaction mixture to encourage the formation of a precipitate. The reaction was than filtered and recrystallized in methanol and water (1:0.5) to yield a pale white product **(12b')**. Yield: 0.28 g (65%); IR [(KBr) ν_{max}/cm^{-1}]: 1218, 1288 (C-O-C stretch); 1493 (CH_3 bend); 1579 (CH_2 bend); 2230 (C≡N stretch); Elemental: expected values (%) C: 75.7, H: 2.9, N: 13.6; results (%) C: 74.9, H: 2.13, N: 13.31.

2.3.2. Synthesis of phthalocyanines and binuclear phthalocyanines

2.3.2.1. Preparation of 3,(4-*tert*-butylphenoxy)phthalocyanine (14a)

Using literature method [79, 121], with minor modification 3-(4-*tert*-butylphenoxy) phthalonitrile (0.49 g, 1.71 mol) was cyclised in the presence of DBU as a catalyst to yield 3,(4-*tert*-butylphenoxy)phthalocyanine as a mixture of isomers. The four positional isomers were further separated by column chromatography.

Fraction A **(C_s symmetry isomer)**

IR [(KBr) ν_{max} /cm-1)]: 1246 (C-O-C); 1362 (CH3); 1486, 1506, 1584 (C=C); 2853, 2922, 2954 (-C-H); 3060, 3289 (=C-H), UV/vis (DCM): λ_{max} nm (log ε): 714 (5.15), 683 (5.07), 654 (4.64), 620 (4.47), 357 (4.73), 333 (4.77). MS (MALDI-TOF) m/z: Calcd 1107.0; Found 1107.7 $[M-H]^+$.

Fraction B **(C_{4h} symmetry isomer)**

IR [(KBr) ν_{max} /cm-1)]: 1246 (C-O-C); 1362 (CH3); 1486, 1506, 1583 (C=C); 2865, 2955 (-C-H); 3036, 3290 (=C-H), UV/vis (DCM): λ_{max} nm (log ε): 719 (5.17), 689 (5.11), 654 (4.64), 625 (4.51), 402 (4.59), 360 (4.46). MS (MALDI-TOF) m/z: Calcd 1107.0; Found 1107.7 $[M-H]^+$.

Fraction C **(D_{2h} symmetry isomer)**

IR [(KBr) ν_{max} /cm-1)]: 1247 (C-O-C); 1362 (CH3); 1485, 1506, 1583 (C=C); 2865, 2957, (-C-H); 3036, 3288 (=C-H), UV/vis (DCM): λ_{max} nm (log ε): 718 (5.03), 688 (4.97), 658 (4.49), 626 (4.36), 353 (4.59), 334 (4.68). MS (MALDI-TOF) m/z: Calcd 1107.0; Found 1107.7 $[M-H]^+$.

Fraction D **(C_{2v} symmetry isomer)**

IR [(KBr) ν_{max}/cm-1)]:1248 (C-O-C); 1362 (CH3); 1477, 1506, 1589 (C=C); 2856, 2924, 2957 (-C-H); 3297 (=C-H), UV/vis (DCM): λ_{max} nm (log ε): 715 (5.04), 687 (5.00), 657 (4.75), 627 (4.56), 360 (4.88), 334 (4.99). MS (MALDI-TOF) m/z: Calcd 1107.0; Found 1107.7 $[M-H]^+$.

2.3.2.2. Preparation of (2,3-dicyanophenoxy)phenyl]phenoxy] binuclear phthalocyanine (15a)

Using the cyclisation method, 1-octanol (1.0 mL) and 1, 2-dichlorobenzene (1.0 mL) were heated at 160°C under nitrogen atmosphere. A 1:20 ratio of 3-[4-[4-(2, 3-dicyanophenoxy) phenyl] phenoxy] phthalonitrile (51 mg, 11.6 mmol) **(12a')** and 3-(4-*tert*-butylphenoxy) phthalonitrile (190 mg, 69.7 mmol) **(7)** were added. Once dissolved a catalytic piece of lithium (29 mg, 4.20 mmol) was added to the reaction mixture. The reaction was left overnight; the dark green product was left to cool, followed by the addition of acetic acid (1.0 mL). After 30 minutes, methanol (1.5 mL) was added and the product was filtered and washed with methanol and water. The product was then purified using flash column chromatography over silica gel to obtain a mixture of normal phthalocyanine and binuclear phthalocyanine. Further column chromatography purification was done over bio-beads for size exclusion to obtain pure BiPc. Yield: 0.025 g (10.3%). IR [(KBr) ν_{max}/cm^{-1}]: 1232, 1248 (C-O-C stretch); 1433 (CH_3 bend); 1590 (CH_2 bend); 1732 (C=O aldehyde); 2869, 2955 (-CH stretch); 3622 (-OH stretch), UV/vis (THF): λ_{max} nm (log ε): 716 (6.47), 687 (6.48), 653 (6.35), 629 (6.23), 407 (6.05), 334 (6.42). MS (MALDI-TOF) *m/z*: Calcd. 2100.5; Found 2102.2 $[M+2H]^+$.

2.3.2.3. Preparation of (2,3-dicyanophenoxy)phenyl]phenoxy]nickel binuclear phthalocyanine (15b)

Using the cyclisation method, 1-octanol (1.0 mL) and 1, 2-dichlorobenzene (1.0 mL) were heated at 160°C under nitrogen atmosphere. A 1:20 ratio of 3-[4-[4-(2,3-dicyanophenoxy)phenyl] phenoxy] phthalonitrile (50 mg, 11.4 mmol) and 3-(4-*tert*-butylphenoxy) phthalonitrile (190 mg, 68.3 mmol) were added. An excess amount of nickel (II) acetate tetrahydrate (1200 mg, 4.82 mmol) was added. Once dissolved, DBU (0.5 mL) was added to the reaction mixture. The reaction was left overnight and the dark blue product was left to cool. After 30 minutes, methanol (1.5 mL) was added and the product was filtered and washed with methanol and water. The product was then purified using flash column chromatography over silica gel to obtain a mixture

of normal metal phthalocyanine and metal binuclear phthalocyanine. Further column chromatography purification was done over bio-beads for size exclusion to obtain pure NiBiPc. Yield: 0.019 g (7.66%). IR [(KBr) ν_{max}/cm^{-1}]: 1232, 1258 (C-O-C stretch); 1433 (CH_3 bend); 1592 (CH_2 bend); 1734 (C=O aldehyde); 2868, 2915, 2957 (-CH stretch); 3622 (-OH stretch), UV/vis (THF): λ_{max} nm (log ε): 687 (6.59), 636 (6.54), 406 (5.76), 334 (6.43). MS (MALDI-TOF) *m/z*: Calcd. 2213.8; Found 2219.7 $[M+6H]^+$.

2.3.2.4. Preparation of (3,4-dicyanophenoxy)-2-naphthyl] binuclear phthalocyanine (15c)

Using the cyclisation method, 1-octanol (1.0 mL) and 1, 2-dichlorobenzene (1.0 mL) were heated at 160°C under nitrogen atmosphere. A 1:20 ratio of 3-[7-(3,4-dicyanophenoxy)-2-naphthyl]oxy] phthalonitrile (11 mg, 242.6 mmol) **(12b')** and 3-(4-*tert*-butylphenoxy) phthalonitrile (41 mg, 14.6 mmol) **(2)** were added. Once dissolved a catalytic piece of lithium (30 mg, 4.28 mmol) was added to the reaction mixture. The reaction was left overnight; the dark green product was left to cool, followed by the addition of acetic acid (1.0 mL). After 30 minutes, methanol (1.5 mL) was added and the product was filtered and washed with methanol and water. The product was then purified using flash column chromatography over silica gel to obtain a mixture of normal phthalocyanine and binuclear phthalocyanine. Further column chromatography purification was done over bio-beads for size exclusion to obtain pure BiPc. Yield: 0.010 g (20.5%). IR [(KBr) ν_{max}/cm^{-1}]: 1248 (C-O-C stretch); 1433 (CH_3 bend); 1590 (CH_2 bend); 1732 (C=O aldehyde); 2868, 2955 (-CH stretch); 3622 (-OH stretch), UV/vis (THF): λ_{max} nm (log ε): 712 (6.51), 684 (6.63), 651 (6.64), 626 (6.59), 385 (6.30), 326 (6.67). MS (MALDI-TOF) *m/z*: Calcd. 2074.4; Found 2080.8 $[M+6H]^+$.

2.3.2.5. Preparation of (3,4-dicyanophenoxy)-2-naphthyl] nickel binuclear phthalocyanine (15d)

Using the cyclisation method, 1-octanol (1.0 mL) and 1, 2-dichlorobenzene (1.0 mL) were heated at 160°C under nitrogen atmosphere. A 1:20 ratio of 3-[7-(3,4-dicyanophenoxy)-2-naphthyl]oxy]

phthalonitrile (14 mg, 11.4 mmol) and 3-(4-*tert*-butylphenoxy) phthalonitrile (130 mg, 65.2 mmol) were added. An excess amount of nickel (II) acetate tetrahydrate (1200 mg, 4.82 mmol) was added. Once dissolved, DBU (0.5 mL) was added to the reaction mixture. The reaction was left overnight and the dark blue product was left to cool. After 30 minutes, methanol (1.5 mL) was added and the product was filtered and washed with methanol and water. The product was then purified using flash column chromatography over silica gel to obtain a mixture of NiPc and NiBiPc. Further column chromatography purification was done over bio-beads for size exclusion to obtain pure NiBiPc. Yield: 0.021 g (29.5%). IR [(KBr) ν_{max}/cm^{-1}]: 1214, 1232 (C-O-C stretch); 1433 (CH_3 bend); 1592 (CH_2 bend); 1760 (C=O aldehyde); 2868, 2918, 2955 (-CH stretch); 3622 (-OH stretch), UV/vis (THF): λ_{max} nm (log ε): 681 (6.49), 630 (6.52), 398 (5.72), 343 (6.30). MS (MALDI-TOF) *m/z*: Calcd. 2187.8; Found 2182.7$[M-5H]^+$.

PUBLICATIONS

Some of the results discussed in this thesis, are based on work published in a peer-reviewed journal and have not been referenced further:

1. Spectroscopic and nonlinear optical properties of the four positional isomers of 4α-(4-*tert*-butylphenoxy)phthalocyanine, **G.N. Ngubeni**, J. Britton, j. Mack, E. New, I. Hancox, M. Walker, T. Nyokong, T.S. Jones and S. Khene, J. Mater. Chem. C, 3 (2015) 10705-10714.
2. Spectroscopic and nonlinear optical properties of 4α-(4-*tert*-butylphenoxy) binuclear phthalocyanine, **G.N. Ngubeni**, J. Britton and S. Khene, Polyhedron (**Submitted**).

Chapter 3

Results and Discussion

3. Results and Discussion

This section presents the spectroscopic and nonlinear optical properties of the compounds synthesised in this work.

3.1. Phthalonitriles

The preparation of the phthalonitriles in **Scheme 3.1** and **Scheme 3.2** are not new because these compounds have been synthesised before [79, 121] however, their synthesis is shown to highlight the exact synthetic methods followed in this thesis.

3.1.1. Synthesis and characterisation of phthalonitrile complexes

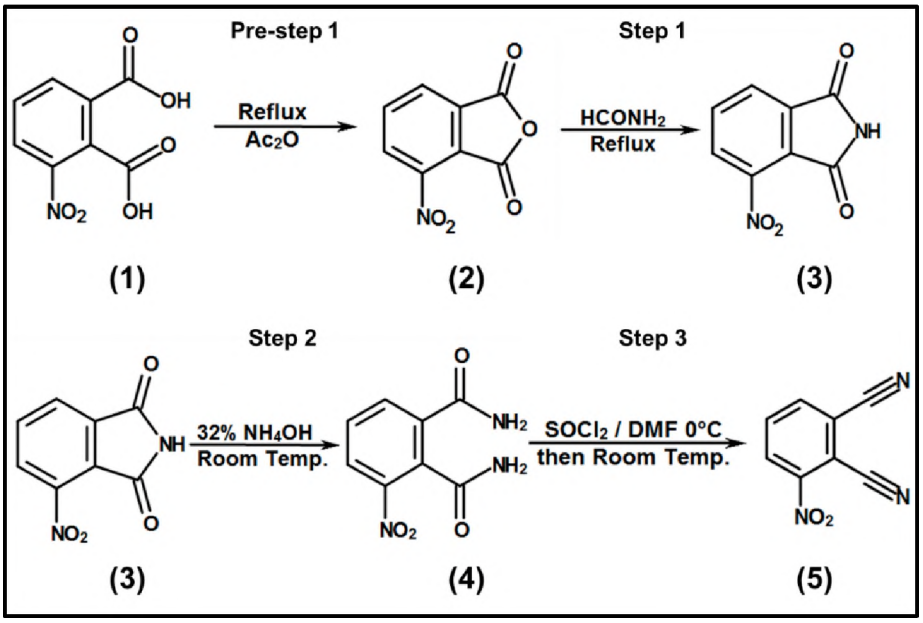

Scheme 3.1: Preparation of 3-nitrophthalonitrile **(5)**.

Each intermediate and final step of this synthesis was carefully monitored by IR in order to ensure that each product had formed prior to moving forward. The entire procedure takes approximately 4 days to complete. This procedure can be started from 3-nitrophthalic anhydride **(2)** however, 3-nitrophthalic acid **(1)** was readily available and used as a precursor to make 3-nitrophthalic anhydride. The nitro ($-NO_2$) group at ~1538 cm^{-1} was retained at each

step. While the formation of the nitrile (-C≡N) group at ~2230 cm^{-1} and the elemental analysis was a good indication that 3-nitrophthalonitrile **(5)** had been successfully synthesised.

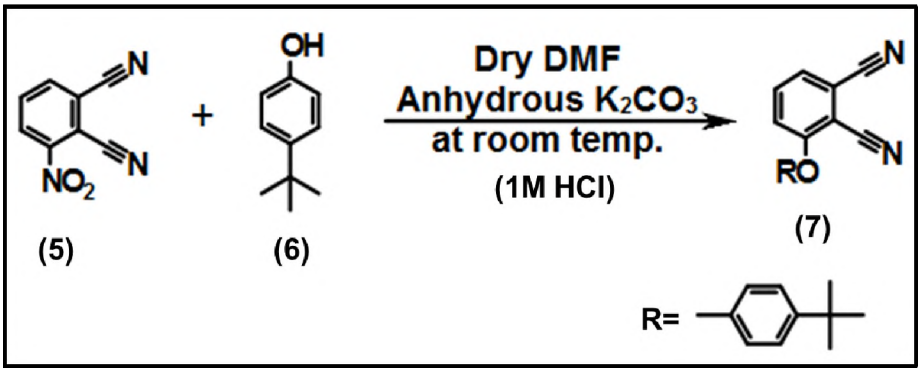

Scheme 3.2: Preparation of 3-(4-*tert*-butylphenoxy) phthalonitrile **(7)**.

Williamson Ether synthesis (**Scheme 3.2)** is the method used for the above preparation where either DMF or DMSO can be utilised. This synthesis involves the nucleophilic aromatic substitution reaction (S_NAr) for the synthesis of substituted phthalonitrile. The Williamson ether synthesis converts an alcohol (R-OH) into ether (R-O-R) in an organohalide (HCl). 4-butylphenol **(6)** was reacted with 3-nitrophthalonitrile **(5)** under the presence of nitrogen gas to produce 3-(4-*tert*-butylphenoxy) phthalonitrile **(7)**. DMF was dried overnight in molecular sieves prior to being used in the reaction. The disappearance of the nitro group, formation of the methyl groups and the retained nitrile peak was observed in the IR spectrum. Elemental analysis also confirmed the product had formed.

3.1.2. Bisphthalodinitriles

Three types of bisphthalodinitriles that are conjugated (in **Scheme 3.3)** and unconjugated (in **Scheme 3.4**) were synthesised.

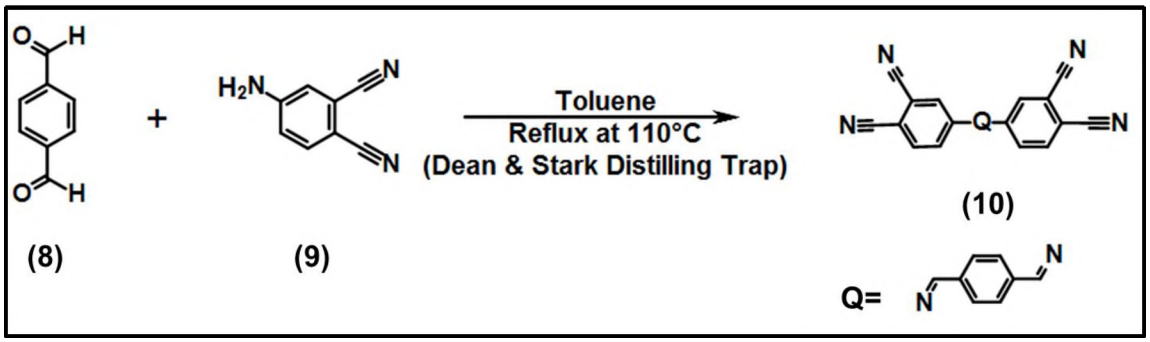

Scheme 3.3: Preparation of Bisorthodinitrile **(10)**.

Bisorthodinitrile **(10)** was synthesised using the literature method [121], whereby commercially bought terephthalaldehyde **(8)** and 4-aminophthalonitrile **(9)** were refluxed. The Dean and Stark distilling trap enabled the successful formation of the yellow product (**Scheme 3)**. **Figure 3.1** shows the IR spectrum of compound **10**. The formation of the Schiff base (-C=N) at ~1624cm^{-1} and ~1586 cm^{-1}, the prominent nitrile peak at ~2240 cm^{-1} that was retained from the 4-aminophthalonitrile and the reduction of the amine and alkene peaks at ~3088cm^{-1} and ~3375cm^{-1} respectively indicate that the product **(10)** was successfully synthesised.

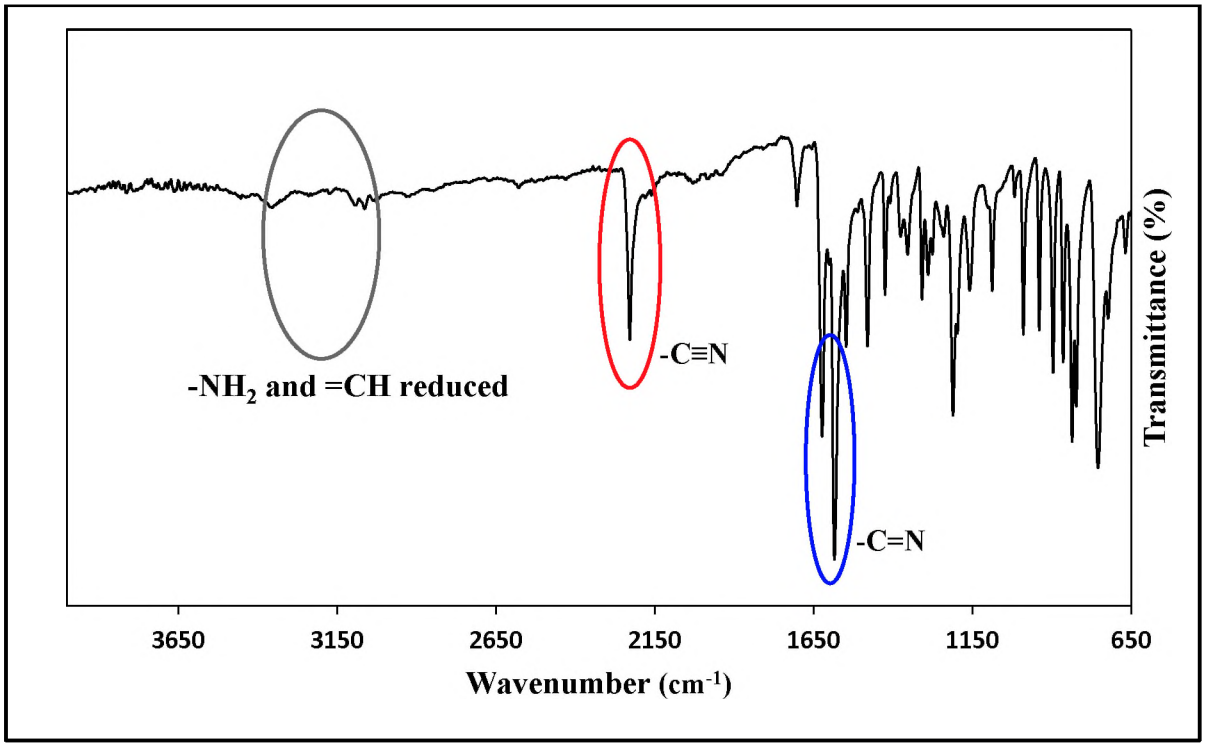

Figure 3.1: IR spectrum of Bisorthodinitrile **(10)**

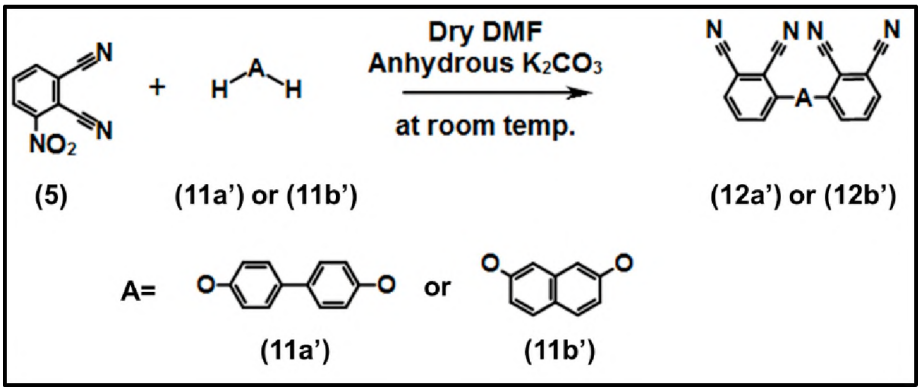

Scheme 3.4: Preparation of 3-[4-[4-(2,3-dicyanophenoxy)phenyl]phenoxy]phthalonitrile **(12a')** and 3-[7-(3,4-dicyanophenoxy)-2-naphthyl]oxy]phthalonitrile **(12b')** respectively.

The synthesis of the bisphthalodinitriles **(Scheme 3.4)** involves the reaction of diols **(11a' and 11b')** with phthalonitrile **(5)** in dry DMF in the presence of excess potassium carbonate at room temperature under nitrogen gas. The elemental analysis and IR spectroscopy (**Figure 3.2**) confirmed the successful synthesis of these linkers, where in both compounds the nitrile group

was retained. Three main functional groups were observed i.e. aromatic rings (=CH) at ~3096 and 3038 cm^{-1}; nitrile (-C≡N) at ~2231 cm^{-1} and ethers (C-O-C) at ~1167, 1207 and 1278 cm^{-1}.

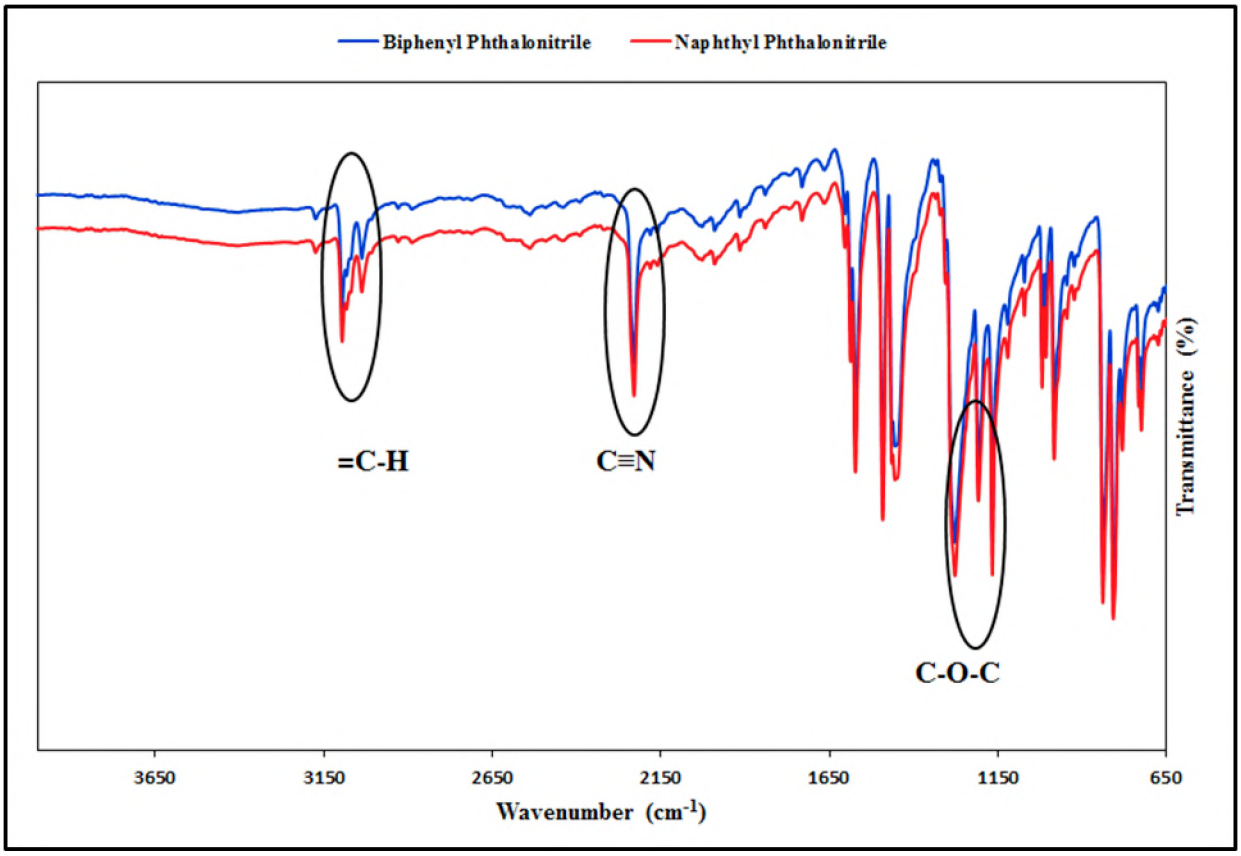

Figure 3.2: Infrared spectra of bisphthalodinitriles.

3.2. Synthesis and spectroscopic characterisation of phthalocyanines and binuclear phthalocyanines

3.2.1. Attempt to synthesise binuclear phthalocyanine

Bisorthodinitrile **(10)** was reacted with 3-nitrophthalonitrile **(7)** to synthesise a BiPc compound. The synthesis of BiPc was not successful however, a mixture of isomeric Pcs were formed **(Scheme 3.5)**. The isomers **(Figure 3.3)** were separated by using flash column chromatography. The column was packed with A Grade silica gel and using dichloromethane (DCM) as the mobile phase. The four possible positional isomers of 3,(4-*tert*-butylphenoxy)phthalocyanine with C_s, C_{4h}, D_{2h} and C_{2v} symmetry are shown in **Figure 3.4**. DCM was used to elute the first three fractions (A, B and C) and a mixture of DCM and MeOH (10:1 ratio) was used to elute the last fraction (D). **Figure 3.3** shows the four fractions that were obtained in order of elution. Fraction A (blue) was eluted first followed by fractions B (light green), C (light green) and D (olive green) with minimal overlap between the fractions.

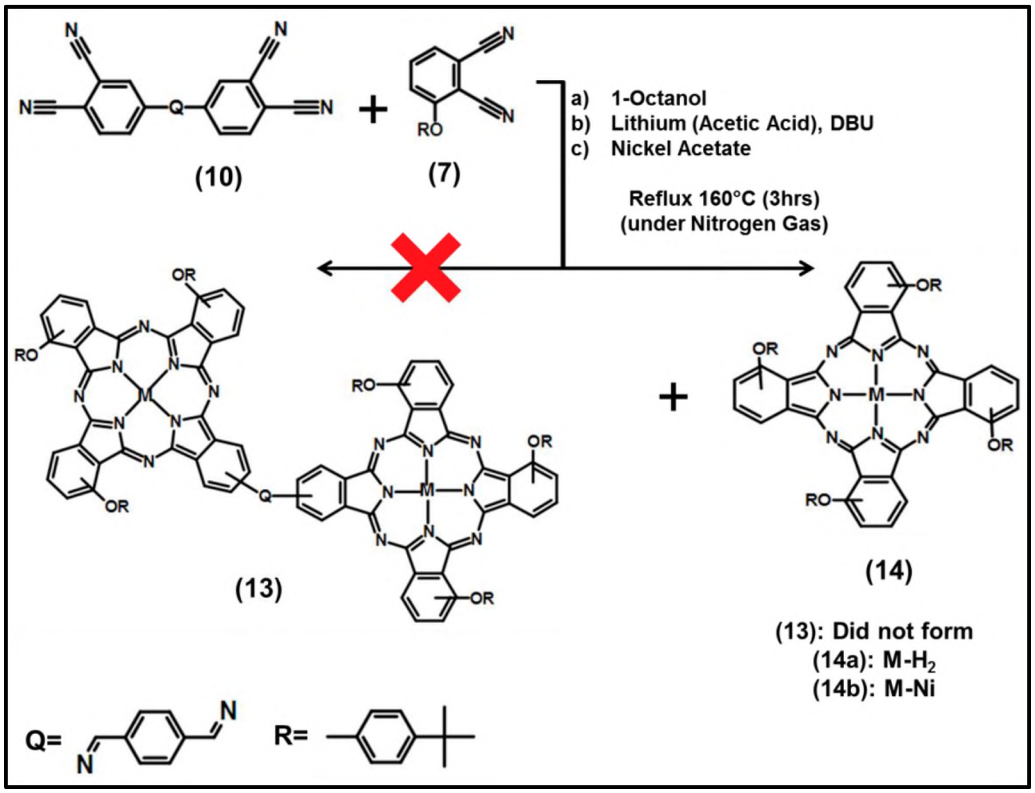

Scheme 3.5: Preparation of 3,(4-tert-butylphenoxy)phthalocyanine **(14)**.

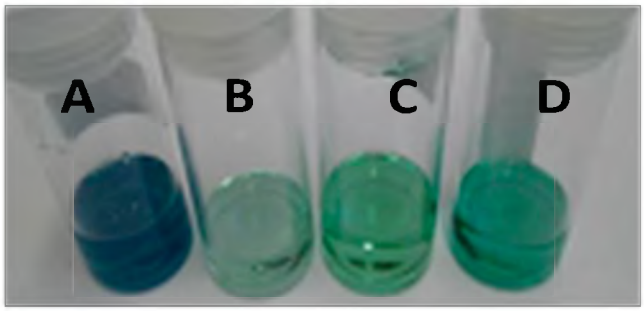

Figure 3.3: Colour changes for the C_s (A), C_{4h} (B), D_{2h} (C) and C_{2v} (D) isomers in DCM.

It is also worth noting that the attempt to separate the tetra-substituted isomers from the cyclisation of only 3-nitrophthalonitrile was made and also resulted in a mixture of isomers where only three isomers were separated. Fraction A was observed to be in such low yield that it could not be eluted by column chromatography. However as mentioned before, separation using advanced techniques such as HPLC have been reported to successfully separate α- or β-substituted Pc isomers synthesised from pure phthalonitrile. In this thesis Z-scan and DFT calculation where used to assign the various symmetries, to be discussed later.

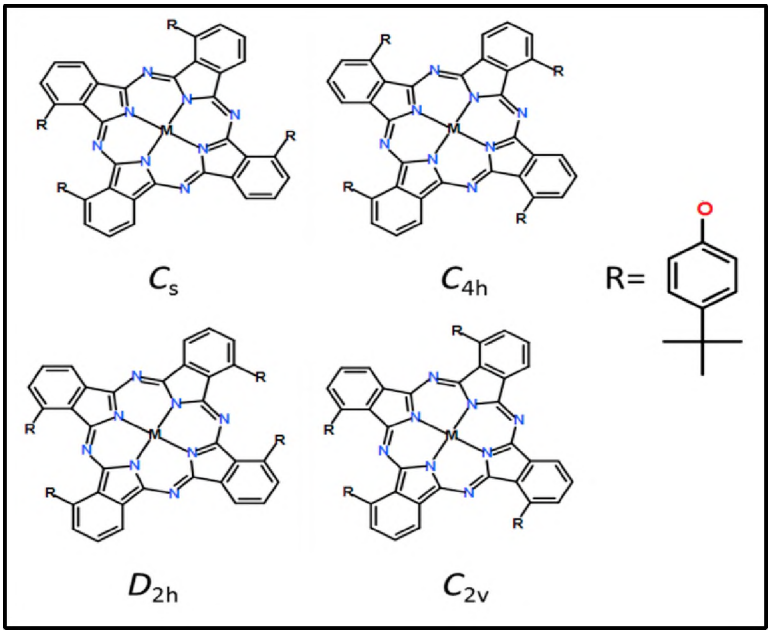

Figure 3.4: The four positional isomers of 1, 8(or 11), 15(or18), 22(or25)-tetrasubstituted phthalocyanines.

The IR spectra **(Figure 3.5)** data indicates the reduction of the nitrile peak at ~2230 cm^{-1} and MALDI-MS **(**see **appendix, Figure 6.1 A)** measurements (1110.7 m/z) were consistent with the properties of the 4α-(4-*tert*-butylphenoxy)phthalocyanine isomers. ^{1}H NMR spectra of the free base phthalocyanine isomers was attempted however; poor resolution was observed possibly due to aggregation which leads to broad peaks of the spectrum [113, 114]. It is a well-known challenge to obtain broad spectrum for Pcs thus NMR spectra data is not included in this work thus, evidence from various techniques is provided.

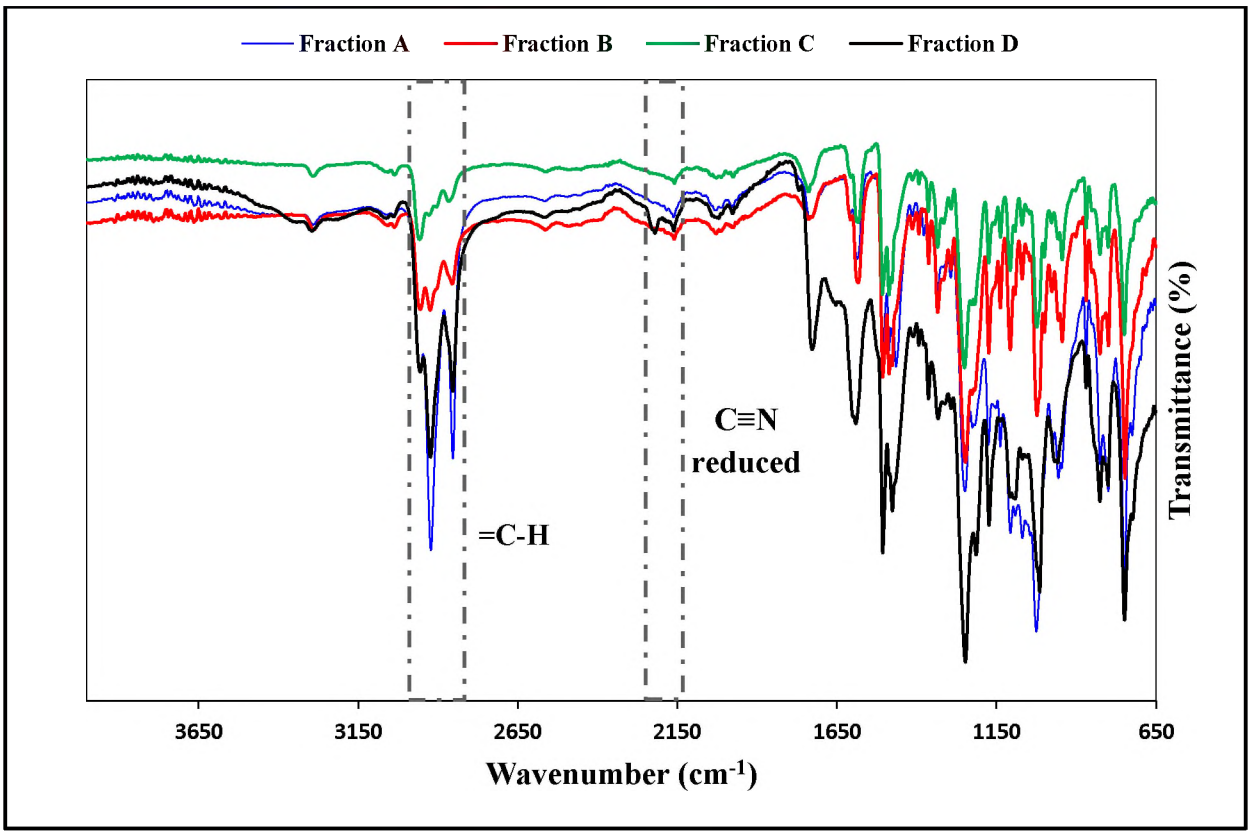

Figure 3.5: Infrared spectra of phthalocyanine isomers.

3.2.2. Binuclear phthalocyanines

Binuclear phthalocyanine molecules have also been studied as a mixture of isomers, this is as a result of statistical condensation method. The isomers could not be separated according to their individual symmetry using column chromatography. However, two possible isomeric mixtures were separated and studied as such. Here the unconjugated oxygen containing linkers were

employed to investigate the effect of the flexibility and rigidity of the linker on NLO properties of BiPcs. **Scheme 3.6** shows the synthesis of the binuclear and mononuclear synthesis of phthalocyanines.

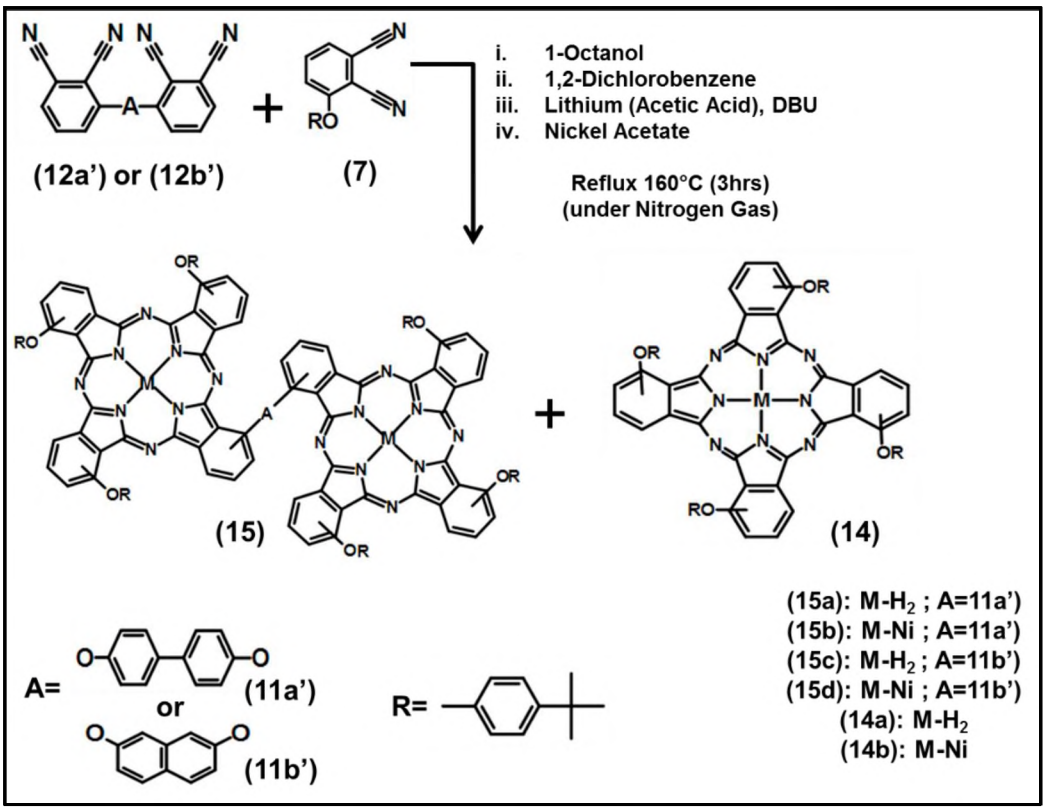

Scheme 3.6: Preparation of mono-Pc, H_2BiPc and Nickel Biphenyl **(15a** and **15b)** and Naphthyl **(15c** and **15d)** binuclear phthalocyanine complexes respectively.

The unconjugated linker and the presence of an oxygen group (instead of the Schiff base) enabled the activation of the benzene ring which facilitated the effective cyclisation of the BiPc molecule. Using the same solvent system as the isomeric compounds, two mixtures of the metal-free and nickel binuclear mixture of isomers were obtained. **Figure 3.6** shows the separated fractions that were obtained in order of elution. Two fractions were obtained from each synthesis such that Fraction E (green), Fraction G (blue), Fraction I (blue/green) and Fraction K (green) were eluted first followed by Fraction F (green), Fraction H (blue), Fraction J (green) and Fraction L (blue) in the metal free and nickel BiPc separation process

respectively. Fraction 2 were eluted with a mixture of MeOH and DCM (10:1 ratio). In the same way, the successful formation of the BiPc molecules were also characterised by IR spectroscopy **(Figure 3.7)** where the reduction of the nitrile group at ~2230 cm^{-1} was observed. Using MS the molecular weight observed was ~2107 m/z (~2081 m/z) and ~2208 m/z (~2187 m/z) for the metal-free and nickel Biphenyl and Naphthyl BiPcs (in brackets) respectively **(**see **appendix**, **Figure 6.1 C-F)**.

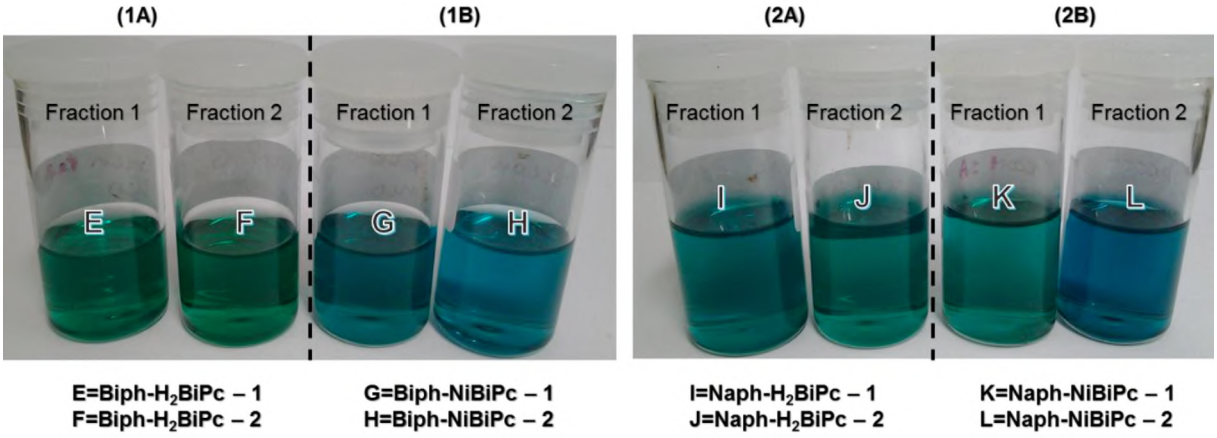

Figure 3.6: Colour changes observed for **(1A)** Biph–H_2BiPc, **(1B)** Biph–NiBiPc, **(2A)** Naph–H_2BiPc and **(2B)** Naph–NiBiPc in THF.

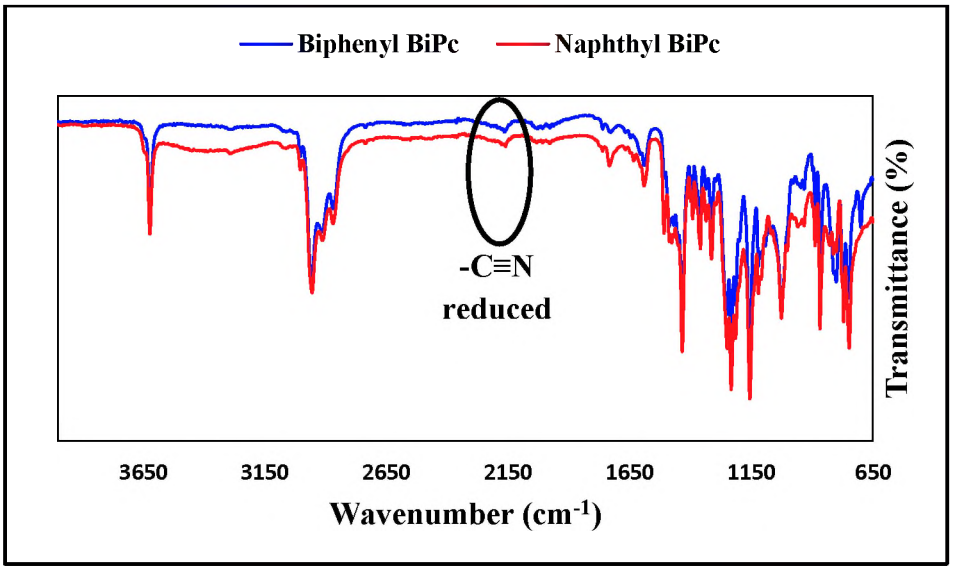

Figure 3.7: Infrared spectra of binuclear phthalocyanines.

3.3. Electronic absorption and MCD spectroscopy

3.3.1. Phthalocyanines

Figure 3.8 shows the optimised structures of 4α-(4-*tert*-butylphenoxy) phthalocyanine positional isomers according to their symmetry. The structures were optimised at the B3LYP level of theory with SDD basis set.

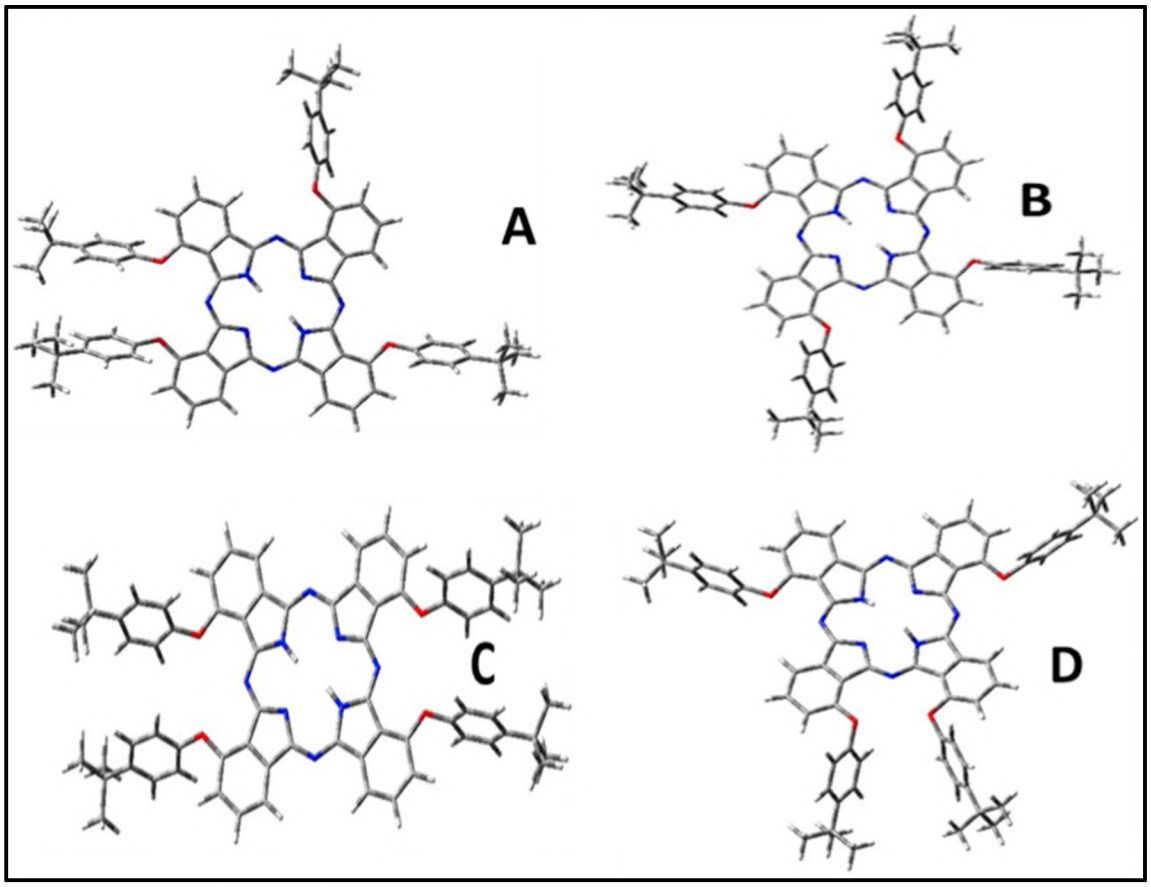

Figure 3.8: Optimised structures of 4α-(4-*tert*-butylphenoxy) phthalocyanine positional isomers with C_s (A), C_{4h} (B), D_{2h} (C), and C_{2v} (D) symmetry substitution patterns.

MCD spectroscopy can be used to identify the main electronic Q(0,0) and B(0,0) bands, due to the presence of intense Faraday $\mathbf{A_1}$ terms or coupled pairs of oppositely-signed Faraday $\mathbf{B_0}$ terms [18]. The Stillman group [123-127] used the simultaneous spectral band deconvolution of the electronic absorption and MCD spectra of phthalocyanines to identify the presence of a second intense absorption band close in the B band region, so the band nomenclature for phthalocyanines was modified to, in ascending energy, the Q (ca. 670 nm), B1 (ca. 370 nm),

B2 (ca. 330 nm), N (ca. 275 nm), L (ca. 245 nm) and C (ca. 210 nm) bands [124]. **Figure 3.9** contains the absorption and MCD spectrum of the C_{4h} positional isomer. The optical spectra of the four positional isomers are almost identical, **Figure 3.9** (and **Table 6.1,** see **appendix)** as are the TD-DFT calculated spectrum that were carried out at the B3LYP/6-31(d) level of theory for a series of positional isomers of a $H_2(OH)_4Pc$ model compound. Since no significant differences are observed or predicted in band energies that are related to the relative orientations of the peripheral substituents, optical spectral data cannot be used to definitively identify the four positional isomers. This is not surprising, since peripheral substituents have a relatively minor impact on the energies of the four frontier π-MOs, **Figure 3.10**, in the absence of a large mesomeric interaction with the Pc π-system [18].

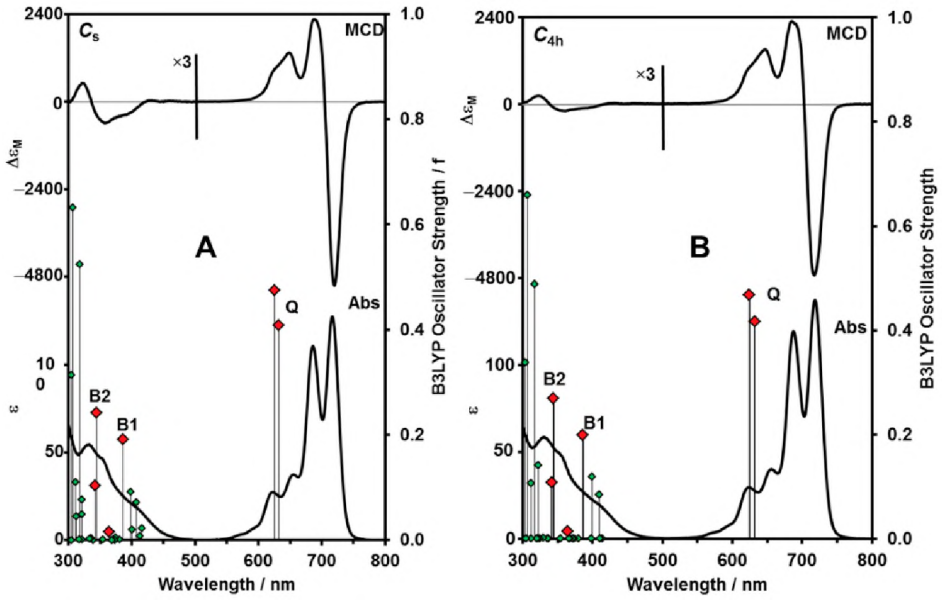

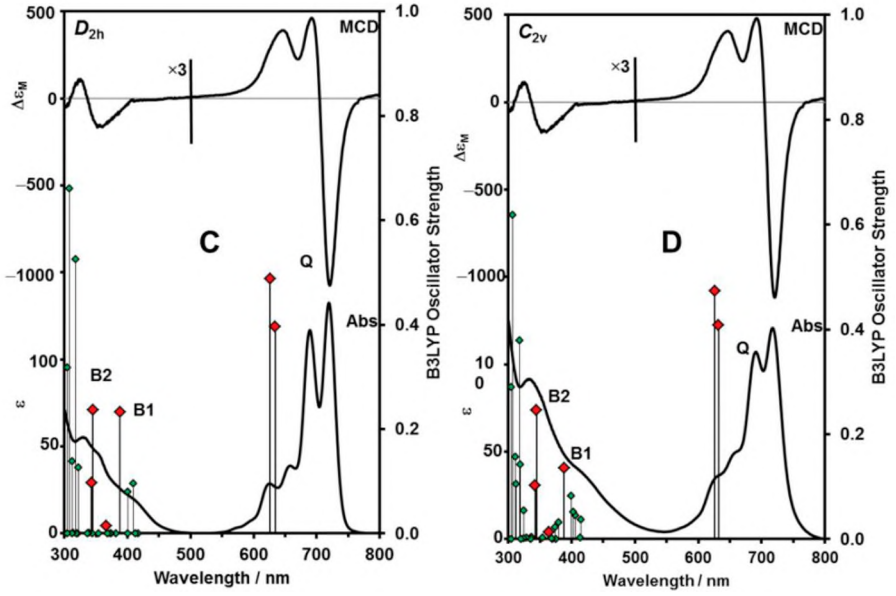

Figure 3.9: UV/vis absorption and MCD spectra of the 4α-(4-*tert*-butylphenoxy) phthalocyanine positional isomers measured in DCM. The calculated bands for the four positional isomers of the $H_2(OH)_4Pc$ model compound are plotted against a secondary axis with red diamonds used to highlight the Q, B1 and B2 bands.

The MCD spectra of the four isomers, **Figure 3.9** shows the peak and trough of the coupled pair of oppositely-signed Faraday B_0 terms in the Q band region. **Figure 3.9**, corresponds to the band centres of the split Q bands in the absorption spectrum. This is the pattern that is anticipated for free base phthalocyanines, since there is no three-fold or higher axis of symmetry. The presence of intense Faraday B_0 term intensity demonstrates that the B1 and B2 bands lie in the 300 – 400 nm region. Although the absorption and MCD spectra are broadly consistent with those normally observed for free base phthalocyanines [18], there is an envelope of intensity in the 400 – 470 nm region that is normally not observed when there are no peripheral substituents. Similar band envelopes have been assigned previously to n → π* transitions associated with the lone pairs on the peripheral oxygen atoms [128], or to the destabilising effect of the electron donating effect of the sp^3 hybridized oxygen atoms on the

π–MOs that are associated primarily with the fused-ring-expansion of the ligand with benzo rings [129], since there are large MO coefficients at the points of attachment for the phenoxy substituents at the α–positions. The presence of π–π* states in the TD-DFT calculations, **Figure 3.9**, is broadly consistent with the latter explanation.

Electronic absorption spectroscopy is one of the most useful methods for characterising phthalocyanines, due to the presence of the characteristic Q and B bands of Gouterman's 4-orbital model [130]. A D_{16h} symmetry $C_{16}H_{162}$– cyclic polyene corresponding to the inner ligand perimeter can be regarded as being the parent hydrocarbon perimeter for describing and rationalising the optical properties. The π-system contains a series of MOs arranged in ascending energy with ML = 0, ±1, ±2, ±3, ±4, ±5, ±6, ±7 and 8 nodal properties based on the magnetic quantum number for the cyclic perimeter, ML. The frontier π-MOs have ML = ±4 and ±5 nodal properties, respectively. The four spin-allowed ML = ±4 → ±5 excitations give rise to two orbitally degenerate $1E_u$ excited states, on the basis of the ΔML = ±9, and ΔML = ±1 transitions. This results in the forbidden and allowed Q and B bands of Gouterman's 4-orbital model for porphyrins [130], since an incident photon can provide only one quantum of orbital angular momentum. Michl [131-134] introduced an a, s, -a and -s terminology for the four MOs derived from the HOMO and LUMO of the parent perimeter so that π-systems of porphyrinoids with differing molecular symmetry can be readily compared, **Figure 3.7**. One MO derived from the HOMO of a $C_{16}H_{162}$– parent hydrocarbon perimeter and another derived from the LUMO have nodal planes which coincide with the yz-plane and are referred to, respectively, as the a and -a MOs, while the corresponding MOs with antinodes on the yz-plane are referred to as the s and -s MOs. Since the a and s MOs that are derived from the HOMO of the parent perimeter have angular nodal planes on alternating sets of atoms, **Figure 3.10**, the incorporation of the *aza*-nitrogen atoms have a much larger stabilising effect on the energy of the s MO resulting in a large separation of the a and s MOs and Q(0,0) bands that are

dominated by the a → -a and a → -s one-electron transitions rather than having near equal contributions from the s → -a and s → -s one-electron transitions [132]. This leads to a mixing of the allowed and forbidden properties of the Q and B bands, so that the Q band becomes the dominant spectral feature in the context of phthalocyanines.

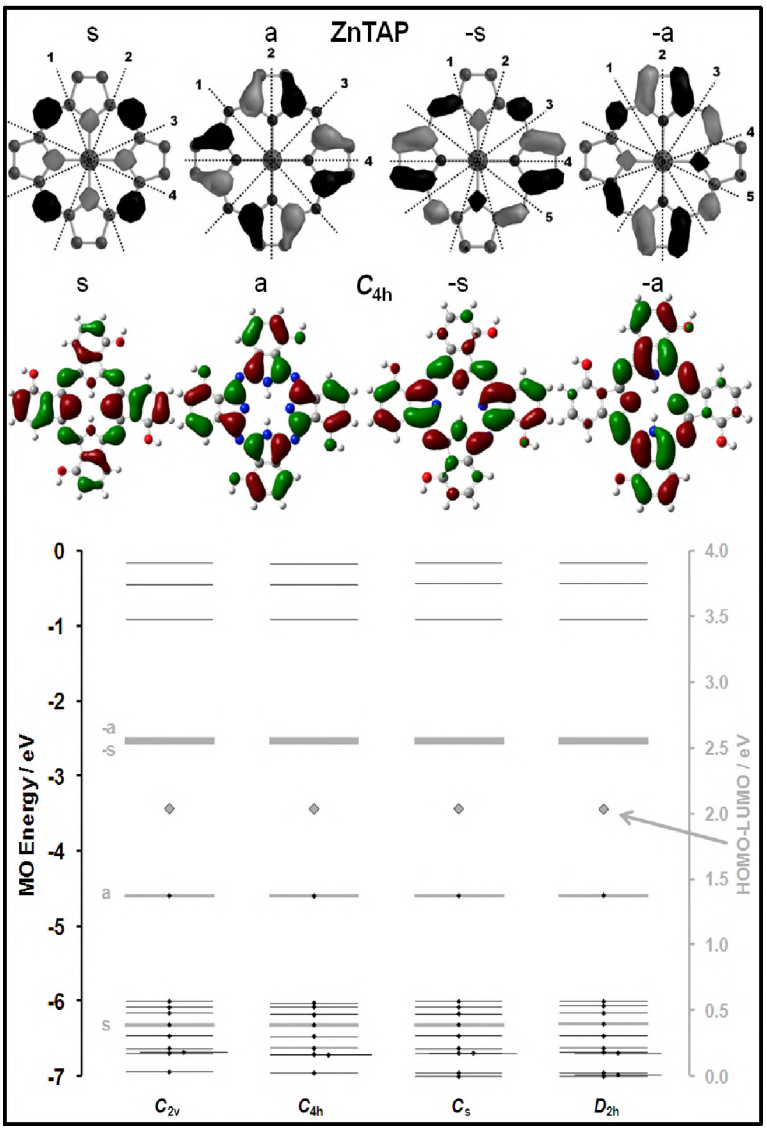

Figure 3.10: Nodal patterns (TOP) of the four frontier π–MOs of zinc tetraazaporphyrin (ZnTAP) with the angular nodal planes highlighted to describe the ML = ±4 and ±5 nodal patterns, and the nodal patterns of C_{4h} isomer of the $H_2(OH)_4Pc$ model compound at an isosurface value of 0.04 a.u. Michl [131-135] introduced a, s, -a and -s nomenclature to describe the four frontier π–MOs based on whether there is a nodal plane (a and -a) or an antinode (s and -s) on the y-axis. Once the alignment of the angular nodal planes has been

clearly defined the effect of different structural perturbations can be readily conceptualized on a qualitative basis through a consideration of the relative size of the MO coefficients on each atom on the perimeter. The MO energies (BOTTOM) of the four positional isomers of the $H_2(OH)_4Pc$ model compound. The a, s, -a and -s MOs of Michl's perimeter model [131-135] are highlighted in gray. σ–MOs associated primarily with the aza-nitrogen lone pairs are offset to the right. Occupied MOs are denoted with small black diamonds. The HOMO–LUMO gap values are plotted against a secondary axis.

3.3.2. Binuclear phthalocyanines

Figure 3.11 shows the optimised structures of high symmetry isomers of C_{4h}:C_{4h} and D_{2h}:D_{2h} representing the first fraction i.e. Biph-H_2BiPc-1 or Naph-H_2BiPc-1 mixture and low symmetry fraction two isomers of C_s:C_s and C_{2v}:C_{2v} are represented by Biph-H_2BiPc-2 or Naph-H_2BiPc-2 mixture **(**see **appendix Figure 6.2** for **Naph-H_2BiPc** and **Naph-NiBiPc)**. For convenience, the same symmetry assignments are used to represent the metalated isomers.

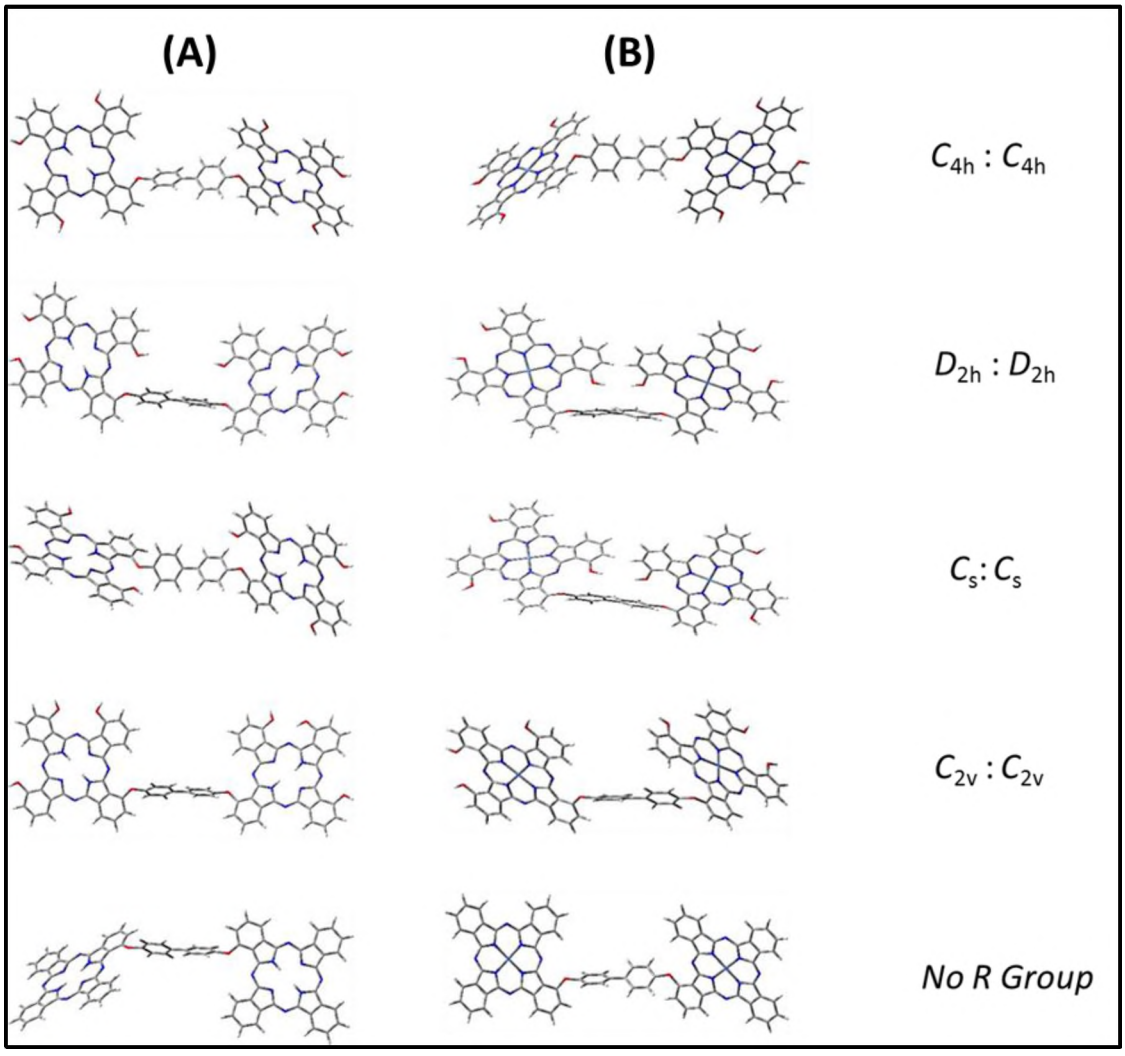

Figure 3.11: Optimised isomeric structures of Biph-H_2BiPc (A) and Biph-NiBiPc (B) with OH groups at the B3LYP level of theory with SDD basis set.

MCD and UV/vis spectra of compounds **15a-d (**in **Figure 3.12 (**E-L**))** shows an intense blue shifted band between ca. 600-350 nm, which is associated with H-aggregation through the

exciton coupling of the Pc units [136]. The intensity of the peak and wavelength indicates a strong intramolecular coupling and thus reflects a co-facial arrangement of the binuclear phthalocyanines aggregates [137].

Pcs with D_{2h} symmetry are known to produce negative MCD troughs associated with the Q band absorption peak at the longest wavelength [98]. Each unit of the metal free BiPcs **(15a and 15c)** approximate the D_{2h} symmetry. Therefore the π system of 3a and 3c is predicted to contain four lowest unoccupied molecular orbitals (LUMOs) of b_{3g}, b_{2g}, b_{1u} and a_u symmetry and two highest occupied molecular orbitals (HOMOs) each from the $1a_{1u}$ and $1a_{2u}$ molecular orbitals (MOs). These MOs are associated with Gouterman's 4-orbital model [130], with b_{3g} and a_u, and b_{2g} and b_{1u} symmetry, respectively. The MCD spectra of 3a and 3c **(Figure 3.12 (E-F** and **I-J))** show negative MCD troughs associated with Faraday B_0 term for the Q band (ca. 630-700 nm) in the longest wavelength. The presence of Faraday B_0 terms indicate that no degeneracy exists in either the ground or the excited states [98]. **Figure 3.12 (E-F** and **I-J)** shows the UV/vis absorption and MCD spectra of metal-free BiPcs contained in Fraction 1 and 2 (**15a and 15c**) which is consistent with those reported previously for D_{2h} symmetry [138]. The UV/vis absorption and MCD spectra of nickel complexes **15b** and **15d** in **Figure 3.12 (G-H** and **K-L)** are consistent with those reported for D_{4h} symmetry [98].

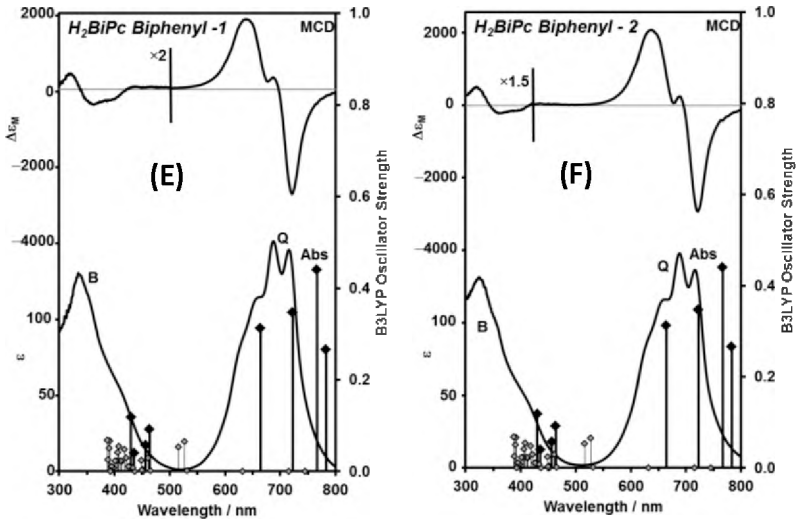
H2BiPc Biphenyl -1
MCD
×2
(E)
B
Q
Abs
ε
Δε_M
B3LYP Oscillator Strength
Wavelength / nm
H2BiPc Biphenyl - 2
MCD
×1.5
(F)
B
Q
Abs
B3LYP Oscillator Strength
Wavelength / nm

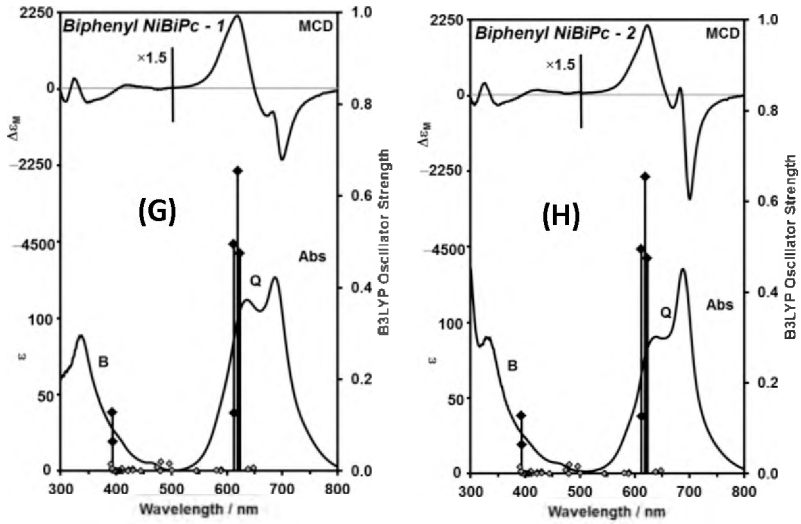
Biphenyl NiBiPc - 1
MCD
×1.5
(G)
B
Q
Abs
ε
Δε_M
B3LYP Oscillator Strength
Wavelength / nm
Biphenyl NiBiPc - 2
MCD
×1.5
(H)
B
Q
Abs
B3LYP Oscillator Strength
Wavelength / nm

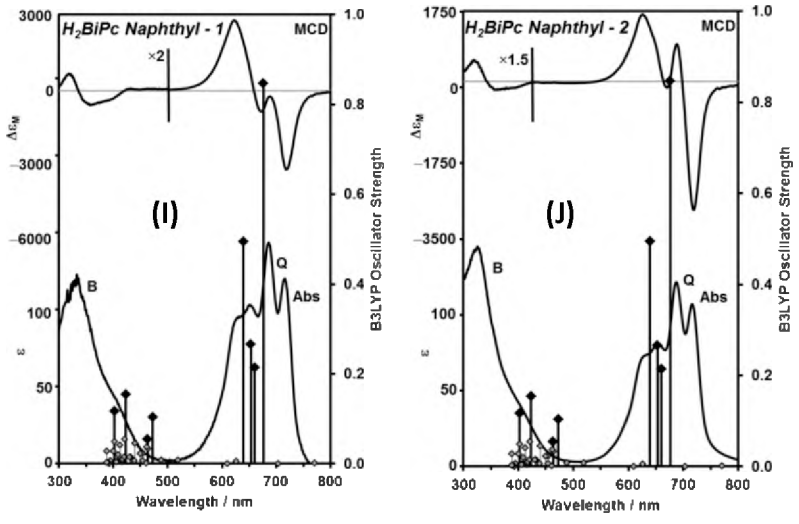
H2BiPc Naphthyl - 1
MCD
×2
(I)
B
Q
Abs
ε
Δε_M
B3LYP Oscillator Strength
Wavelength / nm
H2BiPc Naphthyl - 2
MCD
×1.5
(J)
B
Q
Abs
B3LYP Oscillator Strength
Wavelength / nm

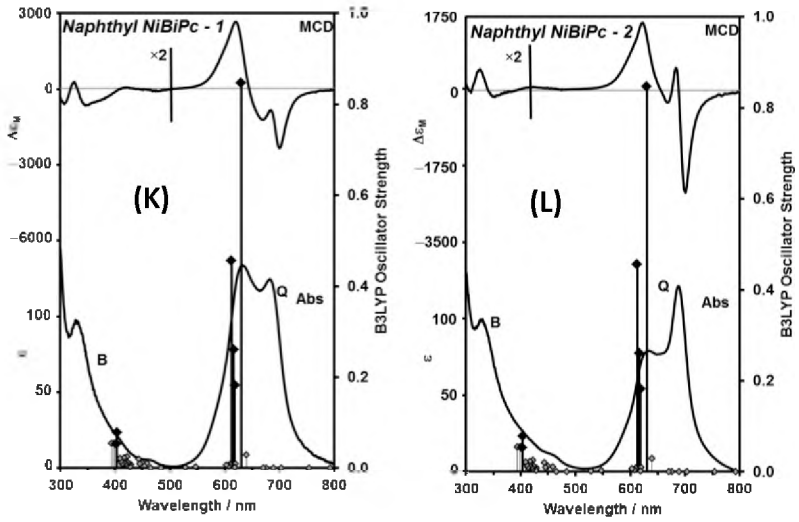

Figure 3.12: MCD and UV/vis spectra of Biphy-H_2BiPc-1 **(E)**, Biphy-H_2BiPc-2 **(F)**, Biphy-NiBiPc-1 **(G)**, Biphy-NiBiPc-2 **(H)**, Naph-H_2BiPc-1 **(I)**, Naph-H_2BiPc-2 **(J)**, Naph-NiBiPc-1 **(K)** and Naph-NiBiPc-2 **(L)** in THF.

The split Q-band observed for compound **15a and 15c (Figure 3.12 (E-F** and **I-J))** is attributed to the π - π^* transition assigned as the Q_{x00} and Q_{y00} of the Pc^{2-} ring [129]. The split Q-band is due to the presence of low symmetry (D_{2h}) which lifts the degeneracy of the two LUMO levels [129]. The B bands in the UV region arise from the deeper π level - LUMO transition.

The MCD Q-bands observed for **15a** and **15c** in the longer wavelength consist of superposition of Faraday $\mathbf{B_0}$ terms originating from individual phthalocyanine units. Similarly to Pcs, the envelope of absorption intensity in the ca. 400-470 nm region has been assigned previously to $n \rightarrow \pi^*$ transitions as associated with the lone pairs on the peripheral oxygen atoms [128], or the destabilizing effect of the electron donating effect of the sp^3 hybridized oxygen atoms on the π −MOs that are associated primarily with the fused-ring-expansion of the ligand with benzo rings [128].

The MCD Q-band of NiBiPcs **15b** and **15d**, **Figure 3.12 (G-H** and **K-L)** shows a single Q-band (ca. 700 nm) with Faraday $\mathbf{A_1}$ terms which is consistent with a metal phthalocyanine

possessing a D_{4h} symmetry [98]. The observed Q-band Faraday $\mathbf{A_1}$ terms suggest that the LUMOs energy levels are degenerate. NiBiPcs **15b** and **15d** MCD Q band consists of superimposition of two Faraday $\mathbf{A_1}$ terms, since each Pc unit approximate a D_{4h} symmetry.

The prominence of the blue shifted aggregation bands observed in **Figure 3.12 (G-H** and **K-L)** again indicates a strong intramolecular coupling and thus reflecting a co-facial arrangement of the NiBiPcs (**15b** and **15d**). The aggregation peak (ca. 620 nm) in **Figure 3.12 (G-H** and **K-L)**, shows that NiBiPcs (**15b** and **15d**) from fraction 1 are more aggregated in solution compared to fraction 2 NiBiPcs. A monomer-like species is expected in the Q band region if the solution contains a monomer-like species with an intense and negative MCD absorption peak around ca. 700-710 nm [136], which is the case for compound **15a-d**.

The rationalisation and description of the MOs of BiPcs is similar to that of the Pcs above. Similarly, **Figure 3.13** shows the incorporation of the *aza*-nitrogen atoms have a much larger stabilizing effect on the energy of the s MO resulting in a large separation of the a and s MOs and Q(0,0) bands that are dominated by the **a** → **-a** and **a** → **-s** one-electron transitions (see **appendix Table 6.2**) rather than having near equal contributions from the **s** → **-a** and **s** → **-s** one-electron transitions. In **Figure 3.13** the MO energy levels of BiPcs are lower compared to MO energy levels of Pcs, which suggest that the studied BiPcs s are easily oxidised compared to their Pc counterpart (see **appendix figure 6.3** for **Biph-NiBiPc, Naph-H_2BiPc** and **Naph-NiBiPc** nodal patterns).

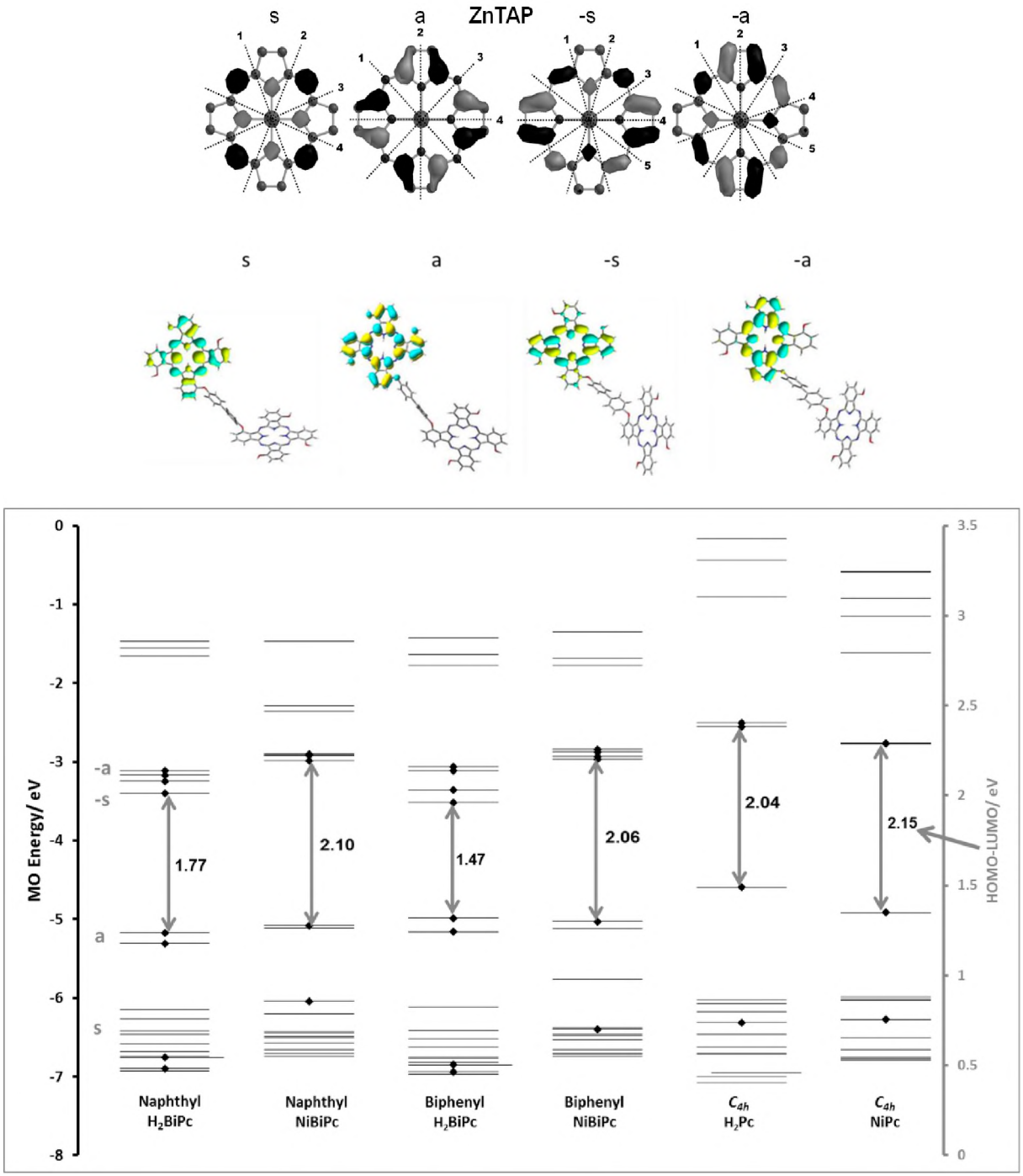

Figure 3.13: The MO energies modelled as C_{4h} symmetry structures of Naph-H_2BiPc (A), Naph-NiBiPc (B), Biph-H_2BiPc (C), Biph-NiBiPc (D), H_2Pc (E) and NiPc (D). The HOMO-LUMO gap values are plotted against a secondary axis with the difference indicated. The eight BiPc MO's and four Pc MO's of Michl's perimeter model are highlighted in grey letters with small black diamonds. Michl [123-127] introduced a, s, -a and -s nomenclature to describe the four frontier π-MOs based on whether there is a nodal plane (a and -a) or an antinode (s and -s)

on the y-axis. The effect of different structural perturbations can be readily understood by first defining the nodal planes and by considering the relative size of the MO coefficients on each atom in the perimeter.

3.4. Absorption, fluorescence & excitation

3.4.1. Phthalocyanines

Time correlated single photon count (TCSPC) has been used to characterise the fluorescence properties of the metal-free synthesised compounds. **Figure 3.14** shows the normalised absorption, excitation and fluorescence spectra of all the isomers. The excitation spectra of the D_{2h}, C_{4h} and C_s isomers are identical to their ground state absorption spectra, but that of the C_{2v} isomer is not. The C_{2v} isomer may be more prone to aggregation than the other isomers.

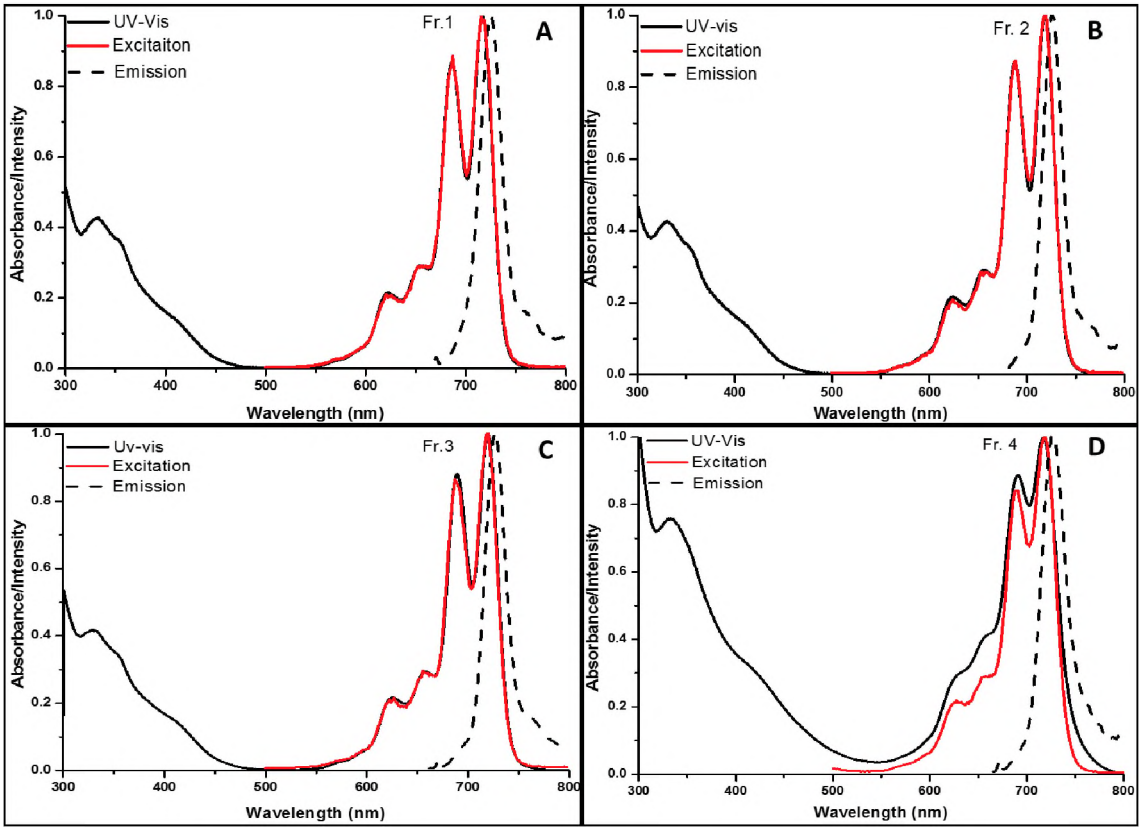

Figure 3.14: UV/vis absorption, excitation and fluorescence emission spectra of isomers C_s (A), C_{4h} (B), D_{2h} (C) and C_{2v} (D) ($\lambda_{exc.}$= 620 nm).

A typical time resolved mono-exponential fluorescence decay curve for the C_s isomer in DCM is shown in **Figure 3.15**. The fluorescence lifetimes for all four isomers lie in the 5.0-5.3 ns

range, see **Table 3.1**, and fall within the range that is typically observed for monomeric phthalocyanine compounds [139].

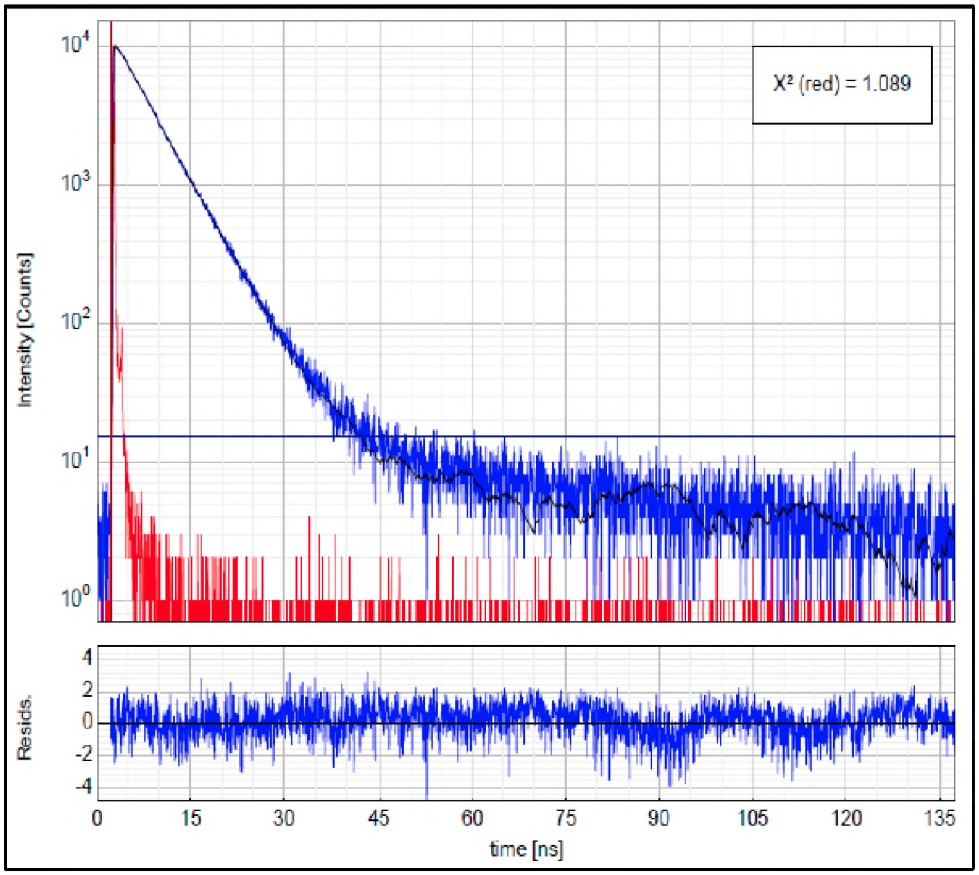

Figure 3.15: Fluorescence decay curve for the C_s isomer in DCM with residuals (λ_{ex} = 670 nm).

The rotational correlation times for isomers C_s, C_{4h}, D_{2h} and C_{2v} were found to be 0.4, 0.4, 0.3 and 0.6 ns respectively. The C_{2v} isomer has a significantly greater correlation time than the other isomers. Differences in rotational correlation times are usually controlled by solvent viscosity, and the size and shape of the molecule [140]. The isomers were measured in the same solvent and have the same molecular weight, so any difference in rotational correlation times can be attributed to the differences in the molecular structures. The correlation times suggest that the C_{2v} isomer experiences a greater drag against the solvent molecules as it rotates compared to D_{2h}, C_{4h} and C_s isomers.

Table 3.1: Q band maxima in the absorption (Abs.), fluorescence excitation (Exc.) and emission (Em.) spectra, fluorescence lifetime (t), anisotropy rotational correlation time (Φ) values and molecular volumes (V_m) in DCM.

Pc	Abs. λ_{max}(nm)	Exc. λ_{max}(nm)	Em. λ_{max}(nm)	τ (ns)	Φ (ns)	$V_m/10^{-27}m^3$
C_s	687:717	655	670	5.3 ± 0.0227	0.360 ± 0.162	3.59
C_{4h}	686:717	652	682	5.3 ± 0.0240	0.381 ± 0.198	3.80
D_{2h}	688:718	654	662	5.1 ± 0.0218	0.339 ± 0.175	3.38
C_{2v}	689:716	653	665	5.0 ± 0.0230	0.641 ± 0.376	6.39

The rotational correlation times ($\boldsymbol{\phi}$) were used to calculate the molecular volume occupied by each isomer using **Equation 28** [140]:

$$\boldsymbol{\phi} = \frac{\eta V}{kT} \qquad (28)$$

were k is the Boltzman constant, η the viscosity, V the molecular volume and T the absolute temperature. The results of molecular volume using the above equation are summarised in **Table 3.1**. The molecular volumes from **Equation 28** are within range of theoretically calculated molecular volume of $\mathbf{1.29 \times 10^{-27} m^3}$ for an unsubstituted phthalocyanine compound. The unsubstituted phthalocyanine diameter was estimated to be **13.5 Å**. The theoretical value was calculated from DFT optimised structures at the B3LYP/6-31G(d) level of theory. The D_{2h}, C_{4h} and C_s isomers are determined experimentally to have similar molecular volumes of 3.59×10^{-27}, 3.80×10^{-27} and $3.38 \times 10^{-27} m^3$ respectively. The C_{2v} isomer has a molecular volume of $6.39 \times 10^{-27} m^3$, which is approximately twice the measured molecular volume of isomer D_{2h}, C_{4h} and C_s. The four positional isomers are expected to have approximately the same molecular volume. The discrepancy observed for the

C_{2v} isomer suggests that this isomer interacts with a greater number of solvent molecules and hence does not move freely in DCM.

3.4.2. Binuclear phthalocyanines

Similarly to Pcs, **Figure 3.16** shows the normalised absorption, excitation and fluorescence spectra of metal free **15a and 15c** (**Fraction 1**, **E** and **I** and **Fraction 2**, **F** and **J**). The excitation spectrum of **15a** and **15c** are not identical to their ground state absorption spectrum, due to the intensity of the aggregation band. The excitation spectra of **15a** and **15c** confirm the bands between ca. 600-650 nm correspond to aggregation, since aggregated species do not fluoresce. As expected no fluorescence or excitation spectra was obtained for nickel complexes. This is because the nickel atom is known to quench the excited state, due to the unpaired electron in the d orbital.

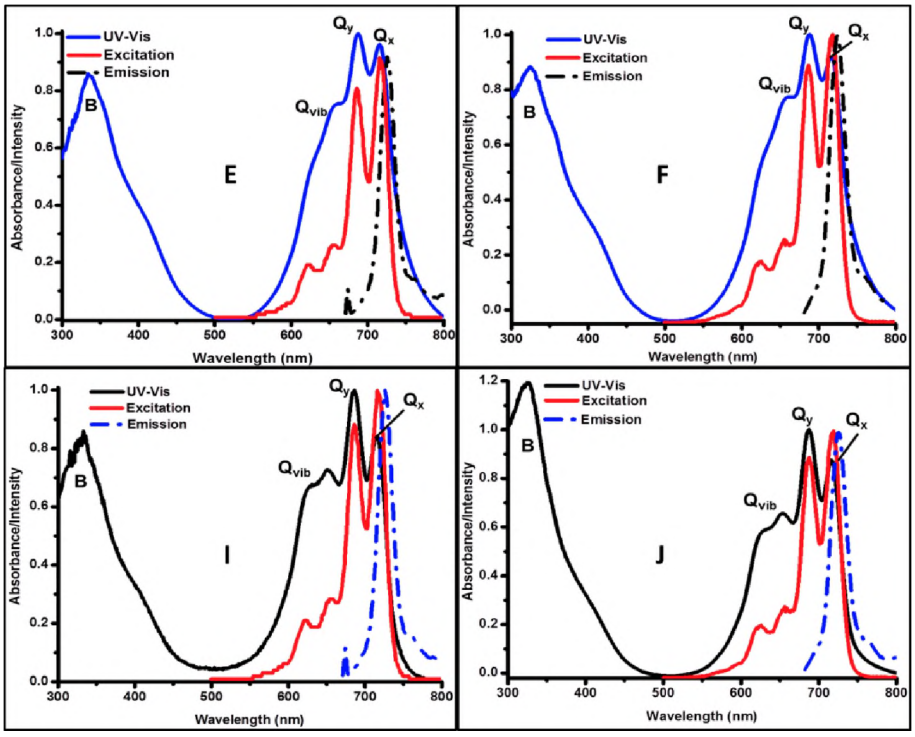

Figure 3.16: UV/vis absorption, excitation and fluorescence emission spectra of binuclear phthalocyanine mixture of isomers for Biphenyl compounds **E** and **F** including Naphthyl compounds **I** and **J** ($\lambda_{exc.}$ = 670 nm).

Similarly, a typical time resolved mono-exponential fluorescence decay curve for metal free binuclear Pc (**15c**) in THF is shown in **Figure 3.17** as an example**.** Contrasting to Pcs, two fluorescence lifetimes (τ) for **15a (**Fraction 1 and 2) and **15c** (Fraction 1 and 2) were obtained (in THF and DCM). The first and second lifetimes (τ_1 and τ_2) were found to be between ~4.1-6.1 ns and ~1.4-3.6 ns respectively, see **Table 3.2**. These lifetimes fall within a typical range for monomeric phthalocyanine compounds [139]. TCSPC concentration studies on ZnPc have shown that with increasing concentration some types of intermolecular interaction, including aggregation, occurs between Pcs [141, 142]. Generally H-type aggregates are known not to fluoresce [142], while J-type aggregates fluorescence is rarely observed [142]. The UV/vis spectra (**Figure 3.16**) predominantly indicates the presence of H-type aggregates.

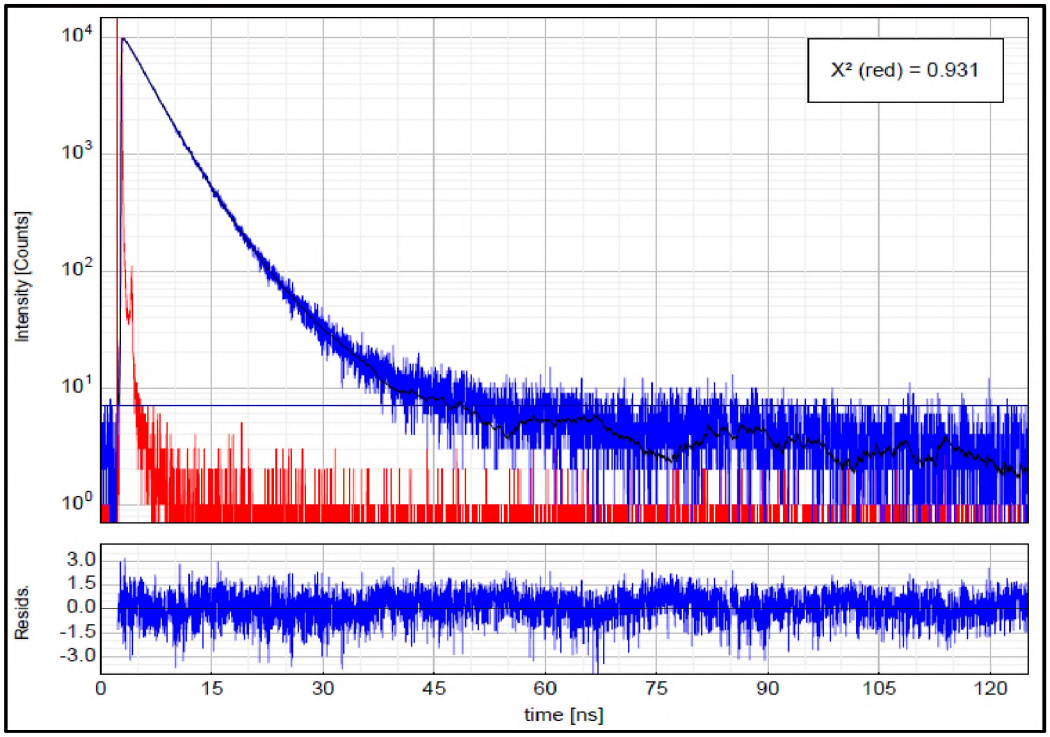

Figure 3.17: Fluorescence decay curve for the Biphenyl isomer in THF with residuals ($\lambda_{exc.}$ = 670 nm).

The intermolecular interaction has been reported to result in appearance of short-lived emitters and broadening of the emission spectrum due to contribution of fast decaying species [141].

Figure 3.17 shows time resolved emission spectra (TRES) of (A) Biphy-H_2BiPc-1, (B) Naph-H_2BiPc-1, (C) Biphy-H_2BiPc-2 and (D) Naph-H_2BiPc-2. The black and red trace, in **Figure 3.17,** correspond to monomeric BiPcs and aggregate species respectively. Therefore TRES results and UV/vis spectra lack of J-type aggregation peak (in **Figure 3.16)** suggest that amongst myriads of possible interaction between isomers, J-type aggregates are present in small amount with respect to H-type aggregates.

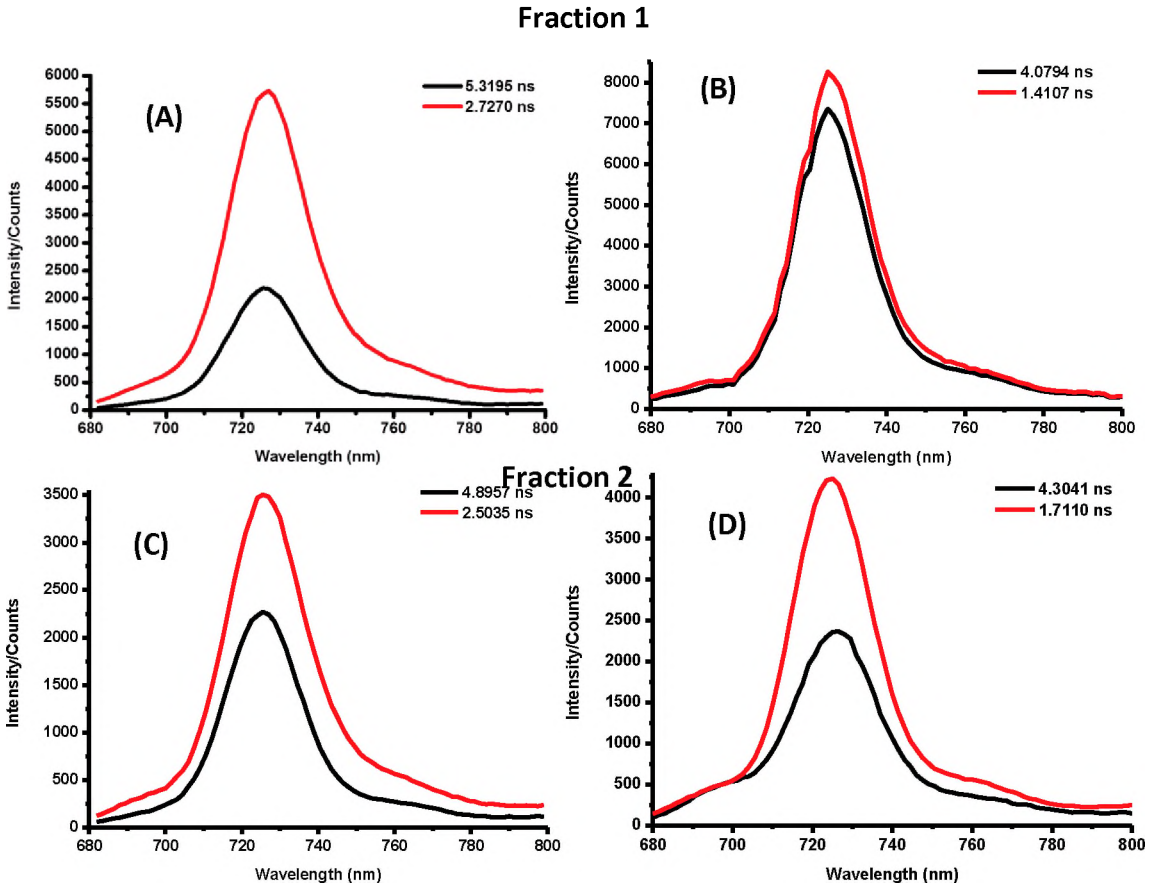

Figure 3.18: Time resolved emission spectra of (A) Biphy-H_2BiPc-1, (B) Naph-H_2BiPc-1, (C) Biphy-H_2BiPc-2 and (D) Naph-H_2BiPc-2 in THF.

Likewise, **Table 3.2** summaries the rotational correlation times (Φ) in THF and DCM for Biphy-H_2BiPc-1 (**A**), Biphy-H_2BiPc-2 (**B**) and Naph-H_2BiPc-1(**C**) were found to be 0.88 (0.52), 1.86 (0.84) and 0.89 (0.78) ns respectively (DCM values indicated in brackets). Naph-

H_2BiPc-2 (**D**) rotational life times could not be measured in the two solvents. In addition, the results of molecular volume using the **Equation 28** (explained above) are summarised in **Table 3.2**.

Table 3.2: Q band maxima in the absorption (Abs), and fluorescence excitation (Exc) and emission (Em) spectra, fluorescence lifetime (τ) and anisotropy rotational correlation time (Φ) values and molecular volumes (V_m) in THF and DCM.

	λ_{max} (nm)			τ (ns)	Φ (ns)	V_m	Solvent
	Abs	Exc	Em			($10^{-27}m^3$)	
(A)	688:716	650	670	6.1±0.0763 (27.8%) 3.6±0.0198 (72.2%)	0.52±0.39	5.19	DCM
	688:716	650	670	5.3±0.0774 (31.6%) 2.7±0.02 (68.4%)	0.882±0.587	7.96	THF
(B)	689:715	650	670	5.4±0.0536 (40.9%) 2.9±0.0235 (59.1%)	0.842±0.891	8.39	DCM
	689:715	650	670	4.9±0.0499 (47.5%) 2.50±0.084 (52.5%)	1.86±0.3.43	16.8	THF
(C)	684:712	650	670	4.8±0.0411 (56.8%) 1.4±0.0230 (43.2%)	0.78±0.567	7.78	DCM
	684:712	650	670	4.1±0.0348 (67.0 %) 1.6±0.0377	0.89±0.540	8.03	THF

				(33.0 %)			
(D)	687:716	650	672	5.1±0.0366	-	-	DCM
				(83.6 %)			
				1.4±0.0198			
				(16.4 %)			
	687:716	650	672	4.3±0.0288	-	-	THF
				(84.8 %)			
				1.7±0.0780			
				(15.2%)			

The molecular volumes are within range of theoretically calculated molecular volume of $1.29 \times 10^{-27} m^3$ for an unsubstituted Pc compound as mentioned above. Biphy-H_2BiPc-1 (**A**), Biphy-H_2BiPc-2 (**B**) and Naph-H_2BiPc-1(**C**) molecular volumes were experimentally determined in THF and DCM (in brackets) to be 8.0×10^{-27} 5.19×10^{-27}, 16.8×10^{-27} 8.4×10^{-27} and 8.0×10^{-27} 7.8×10^{-27} m^3 respectively (see **Table 3.2**). The experimentally determined molecular volumes are expected to be more accurate in THF, because THF is a more viscous solvent compared to DCM. Viscous solvents tend to slow down the rotation of molecules in solution. Compared to molecular volume determined for normal Pc ($\sim 3.0 \times 10^{-27}\ m^3$) for Pcs above, BiPcs occupy greater molecular volume as expected.

3.5. Solid state absorption and UPS spectra of phthalocyanines

Figure 3.19 contains the solid state electronic absorption spectra of D_{2h}, C_{4h}, C_{2v} and C_s isomers adsorbed on indium tin oxide (ITO) substrate. The spectra of the D_{2h} and C_{4h} isomers show the typical aggregation pattern for phthalocyanine compounds, whereby the aggregation peak is blue shifted with respect to the monomer peak. The blue-shifted peak is consistent with H aggregation of phthalocyanine molecules on the ITO substrate. The absorption spectra of the low symmetry C_s and C_{2v} isomers exhibit a red-shifted aggregation peak with respect to the monomeric peak. This is consistent with J aggregation of phthalocyanine molecules on the ITO substrate. The stacking pattern is directed by the symmetry of the phthalocyanine molecules. The observed aggregation pattern helps to distinguish the fractions possessing the higher (D_{2h} and C_{4h}) and lower symmetry (C_s and C_{2v}) isomers. The different spectral properties of the two groups provides further support for the symmetry assignments that were made based on the β values obtained from the *Z*-scan technique. However the solid state absorption techniques are not sensitive enough to the relative orientations of the peripheral substituents to readily distinguish between the D_{2h} and C_{4h}, or C_s and C_{2v} isomers.

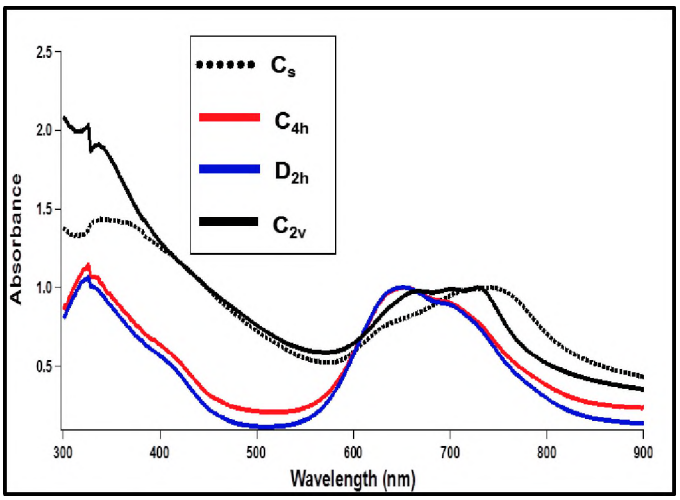

Figure 3.19: UV/vis absorption spectra for C_s (black line), C_{4h} (red line), D_{2h} (dotted line), and C_{2v} (blue line) against an ITO background scan.

The UPS technique is sensitive enough to distinguish subtle differences between the four isomers in a solid state arrangement, **Figure 3.20**. The secondary electron UPS spectra **(Figure 3.20a)** determines the work function for each isomer while the valence band UPS spectra **(Figure 3.20b)** shows the variance in HOMO onset from the Fermi level.

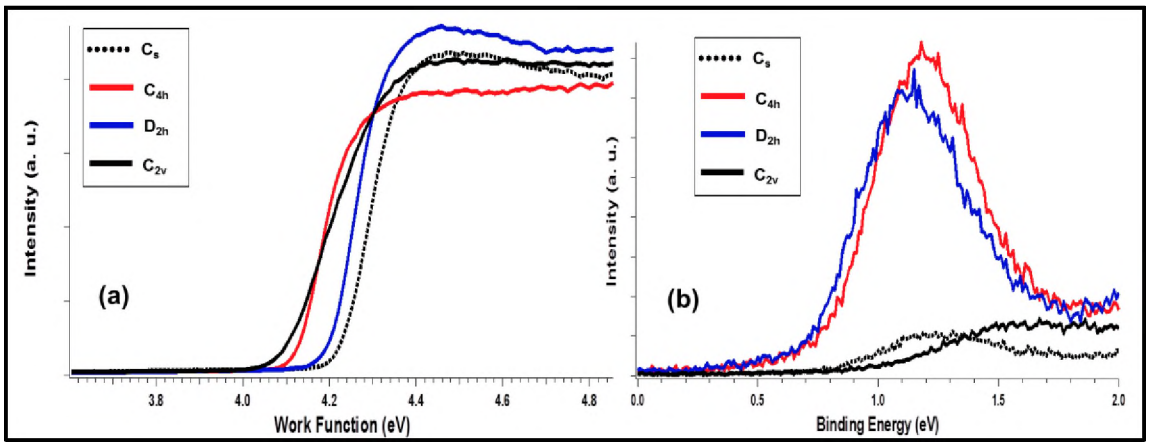

Figure 3.20: (a) Onset of the secondary electron cut-off and (b) valence band UPS spectra for C_s-H_2Pc (black line), C_{4h}-H_2Pc (red line), D_{2h}-H_2Pc (dotted line) and (4) C_{2v}-H_2Pc (blue line) system on bare ITO.

The work function and HOMO onset (EF-HOMO)) values from the UPS data are used to construct a schematic energy level diagram, **Figure 3.21**, for the (A) C_s-H_2Pc, (B) C_{4h}-H_2Pc, (C) D_{2h}-H_2Pc and (D) C_{2v}-H_2Pc system on bare ITO. The energy level diagram shows the different combinations of the work function and EF-HOMO onset energies to determine the ionization potential (IP) energy level for each isomer. The differences in the work function and EF-HOMO of the isomers could be due to variation in the thickness and pinning to the ITO. Hence the ionisation potential is the most important parameter to compare between the isomers. The work function and the EF-HOMO values are added together to determine IP for each isomer. The low symmetry C_s and C_{2v} isomers are predicted to have similar ion IP of 5.02 and 5.04 eV, respectively, while the high symmetry D_{2h} and C_{4h} isomers are both predicted to

have values of 4.91 eV. UPS results matches with the solid state UV/vis absorption for the isomer symmetry pairing.

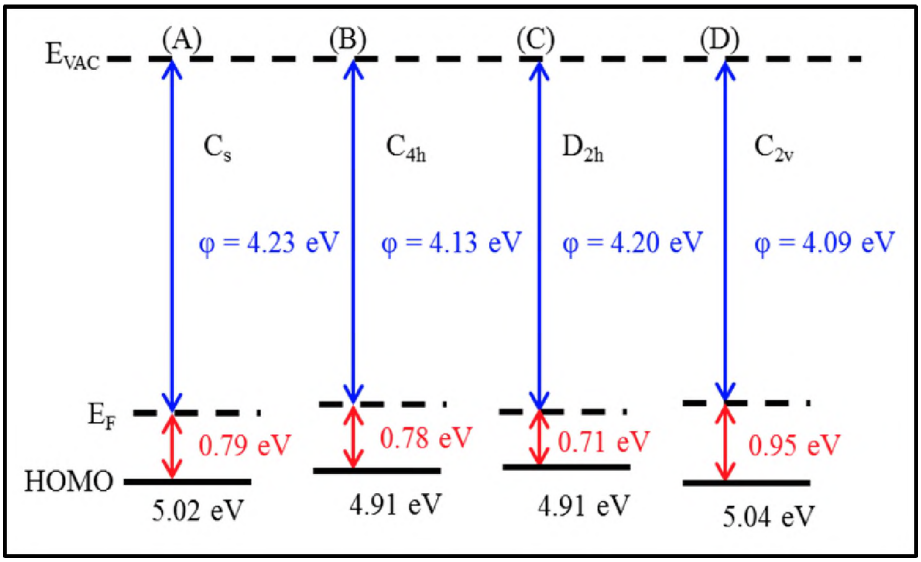

Figure 3.21: Schematic energy level diagram for the (A) C_s-H_2Pc, (B) C_{4h}-H_2Pc, (C) D_{2h}-H_2Pc and (D) C_{2v}-H_2Pc system on bare ITO.

Due time constraints, the solid-state and UPS analysis could not be conducted for the binuclear phthalocyanine compounds.

3.6. Experimental and computational nonlinear optical properties

3.6.1. *Z*-scan properties of phthatlocyanines

In this thesis, the four positional tetra-α-substituted (4α) isomers of metal free 1, 8(or 11), 15(or 18), 22(or 25)-(4-tert-butylphenoxy)phthalocyanine and the eight binuclear phthalocyanines have been fully separated and their NLO properties have been measured separately, to identify which isomer provides the largest contribution towards the observed NLO response.

A symmetry sensitive method i.e. *Z*-scan, was applied to determine the NLO response properties of these material. *Z*-scan revealed that each compound was significantly different from each other. Strong nonlinear absorption behaviour, with reverse saturable absorption (RSA) profiles, was observed for all of the isomers studied, **Figure 3.22**. The nonlinear absorption coefficient (**β**), third order optical susceptibility (Im[$\chi^{(3)}$]) and hyperpolarizability (γ) values were determined for all of the isomers, **Table 3.3 and 3.4**. The **β** values were obtained by a nonlinear fit of $\mathbf{q_0(z_s)}$, a parameter that characterises the strength of the nonlinearity in the curve depicted in **Figure 3.22**, using **Equations 9 and 11** above. The measured **β** values for the isomers display a trend in which (Fraction B) C_{4h} (34.0×10^{-5} m.MW^{-1}) > (Fraction D) D_{2h} (28.8×10^{-5} m.MW^{-1}) > (Fraction A) C_{2v} (22.8×10^{-5} m.MW^{-1}) > (Fraction C) C_s (13.7×10^{-5} m.MW^{-1}).

The measured **β** values lie within the range of those reported previously for phthalocyanine complexes [86, 143, 144]. In the absence of single crystals suitable for X-ray crystallography, the symmetry labelling for the four fractions was determined using DFT by analysing the calculated **β** values, since **β** values are known to be very sensitive to symmetry [87]. **Table 3.3** gives the measured and DFT calculated **β** values, which were used to identify the symmetry of the Pc in each fraction. The theoretical **β** values suggest that the C_{4h} isomer is the most active and is responsible for most of the observed overall NLO response when measurements are made with a mixture of isomers.

It is known that nonlinearity increases with asymmetry when absorption by the excited state predominates [145]. The observed trends suggest that the C_{4h} isomer possesses the most efficient acentric order in terms of **β** values. The C_{2v} isomer shows a greater efficiency with respect to the C_s isomer, and the D_{2h} isomer has the least efficient acentric order. Efficient acentric molecular ordering is known to be the most important property for achieving a large bulk second order NLO response.

The values of third order nonlinear imaginary susceptibility (Im[$\chi^{(3)}$]) and hyperpolarizability (γ) values are shown in **Table 3.4**. The optimal third order nonlinear hyperpolarizability values for phthalocyanines in solution have been reported to lie within $\mathbf{10^{-34}}$ - $\mathbf{10^{-29}}$ esu range [116]. The values determined for the series of isomers are all higher than the lower value. The measured γ values for the monomeric isomers follows a trend where C_{4h} (2.32×10^{-31} esu) > D_{2h} (2.11×10^{-31} esu) > C_{2v} (1.11×10^{-31} esu) > C_s (0.68×10^{-31} esu) respectively.

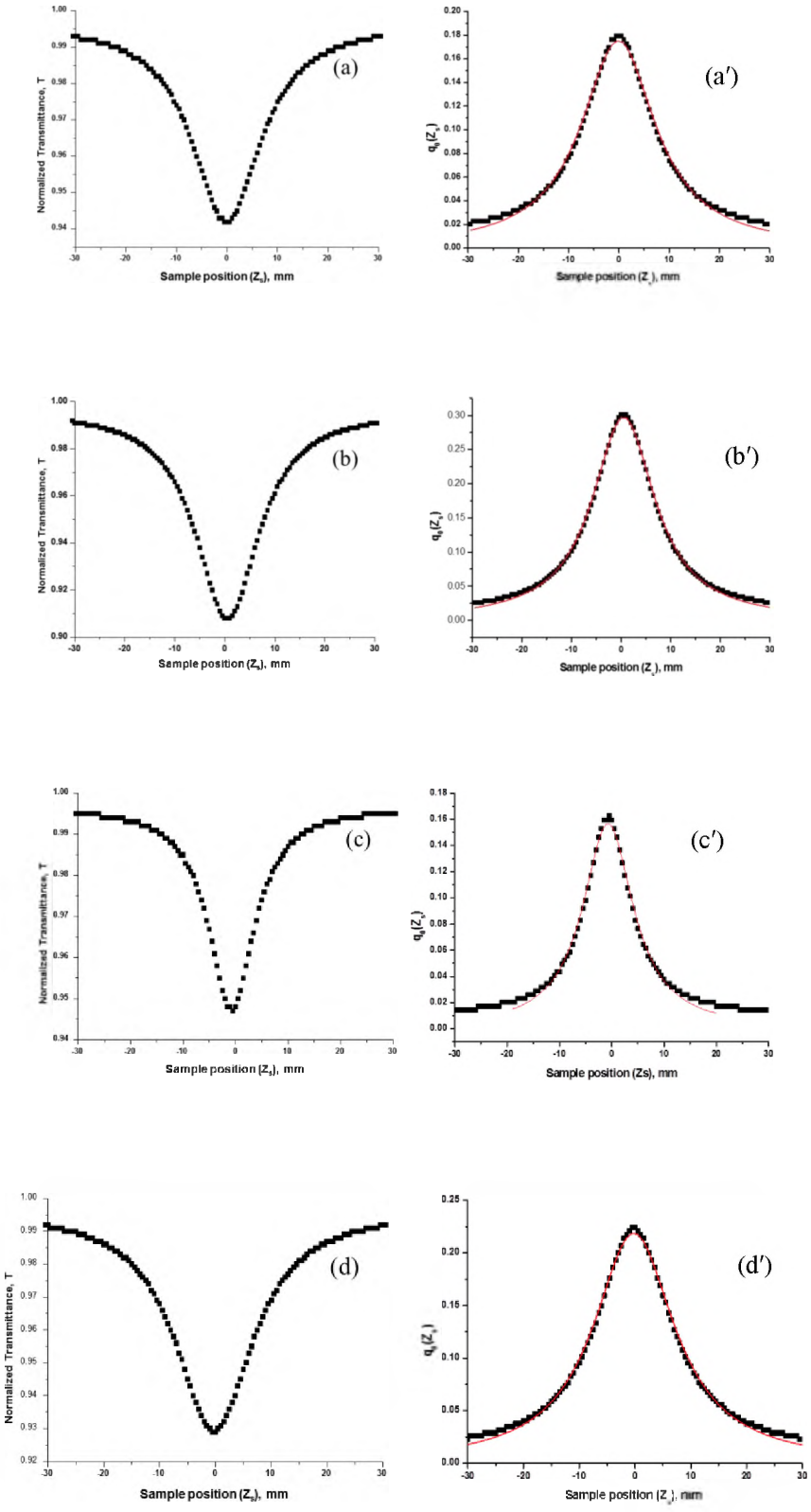

Figure 3.22: *Z*-scan (a-d) and nonlinear fit (a′-d′) curves ($q_0(Z_s)$) for (a) C_s-H_2Pc, (b) C_{4h}-H_2Pc, (c) D_{2h}-H_2Pc and (d) C_{2v}-H_2Pc. All experiments were conducted in DCM solution.

Table 3.3: Experimental and theoretical *Z*-scan results for second order nonlinear polarizability, **β**. DFT calculated with the B3LYP functional and 6-31G(d) basis sets.

Fraction	**Details**	**Q_0**	**Z_R (mm)**	**β (m. MW^{-1}) $\times 10^{-5}$ (exp.)**	**β (esu) $\times 10^{-5}$ (Theor.)**
A	C_s	0.157	5.91	13.7	2.49
B	C_{4h}	0.297	7.74	34.0	4.61
C	D_{2h}	0.219	8.90	28.8	4.00
D	C_{2v}	0.177	8.68	22.8	3.42

Table 3.4: Z-scan results for third order nonlinear hyperpolarizability, γ, and imaginary susceptibility, $Im[\chi^{(3)}]$.

Isomer	**$Im\ \chi^3$ /α(esu)**	**γ(esu) $\times 10^{-31}$**
C_s	2.30×10^{-14}	0.68
C_{4h}	3.43×10^{-14}	2.32
D_{2h}	1.38×10^{-14}	2.11
C_{2v}	$2.91\ 10^{-14}$	1.11

3.6.2. *Z*-scan properties of binuclear phthalocyanines

The *Z*-scan results below (**Figure 3.23**) represents a sample of *Z*-scan/NLO plots showing a typical nonlinear absorption behaviour, with reverse saturable absorption (RSA) profiles for Biph-H_2BiPc-1 (e, e'), Biph-NiBiPc-1 (f, f'), Naph-H_2BiPc-1 (i, i') and Naph-NiBiPc-1 (j, j') (**see appendix for Fraction 2 data Figure 6.4**). Using **Equations 12-17** described above, nonlinear absorption coefficient (β) was determined for all BiPcs studied in this work and the results are summarised in **Table 3.5**.

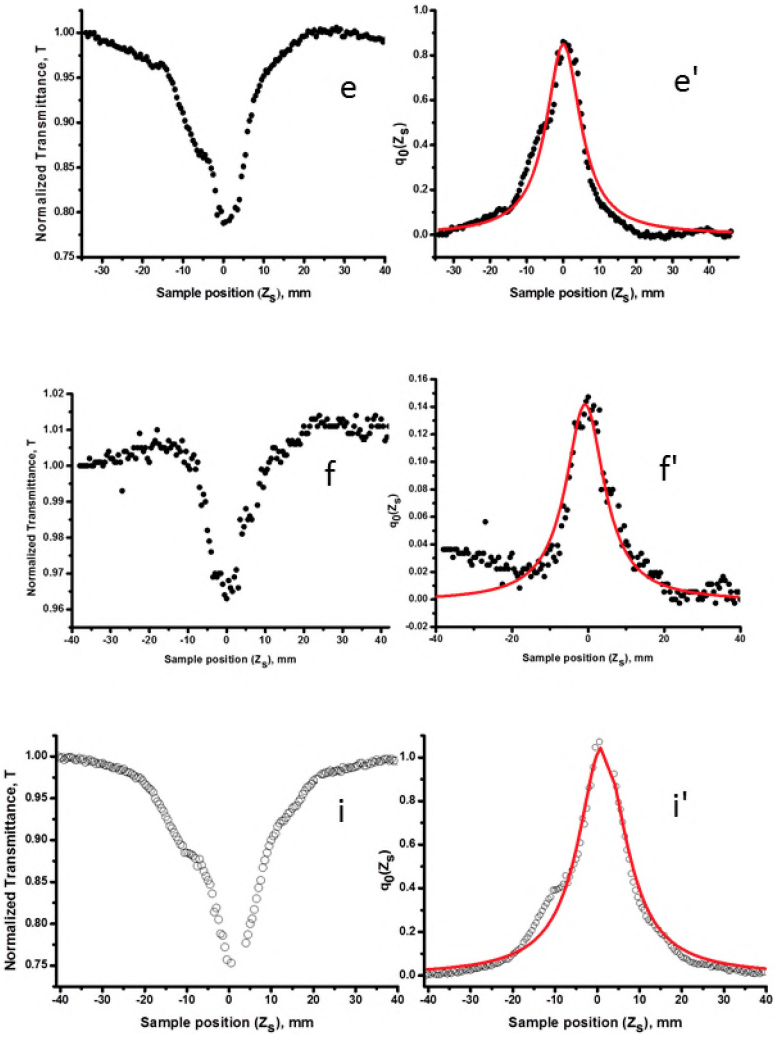

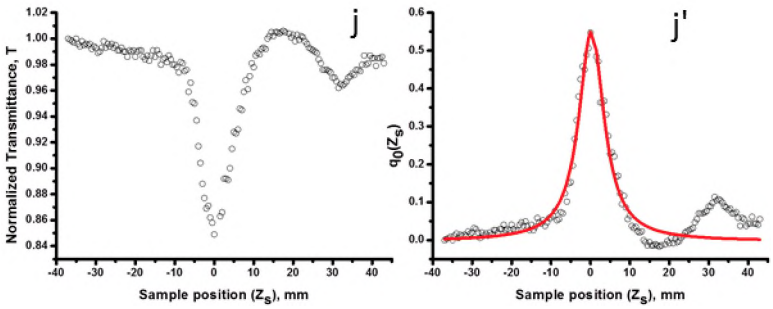

Figure 3.23: *Z*-scan and nonlinear fit curves for Biph-H_2BiPc-1 (e, e'), Biph-NiBiPc-1 (f, f'), Naph-H_2BiPc-1 (i, i') and Naph-NiBiPc-1 (j, j') in THF solution.

Table 3.5 below shows the experimental *Z*-scan results for second-order nonlinear polarizability and theoretically calculated β values for binuclear phthalocyanine compounds. Fraction 1 and 2 of both Biphy-H_2BiPcs and Naph-H_2BiPcs where assigned to possess isomers of high and low symmetry respectively. The assigmnents were based on previous work done on their monomeric counterpart (Pcs above), whereby Fraction 1 and 2 of the monomer where found to possess isomers grouped into high and low symmetry respectively. **Table 3.5** shows the different fractions as Biph-H_2BiPc-1 and Naph-H_2BiPc-1 for high symmetry as the first fraction and Biph-H_2BiPc-2 and Naph-H_2BiPc-2 for low symmetry as the second fraction.

In **Table 3.5**, Biph-H_2BiPc-1 and Biph-H_2BiPc-2 experimental β values were found to be $72.2 \times 10^{-5} m.MW^{-1}$ and $36.5 \times 10^{-5} m.MW^{-1}$ respectively. The results suggest that the isomers found in this high symmetry fraction shows enhanced β values compared to the low symmetry isomers. A similar trend was observed for Naph-H_2BiPc-1 and Naph-H_2BiPc-2, with β values $82.6 \times 10^{-5} m.MW^{-1}$ and $47.5 \times 10^{-5} m.MW^{-1}$ respectively. The Naph-H_2BiPc-1 experimental β value was found to be the highest for unmetalated fractions. The β value trend for unmetalated BiPcs is summarised as follows Naph-H_2BiPc-1 > Biph-H_2BiPc-1 > Naph-H_2BiPc-2> Biph-H_2BiPc-2. The highly aggregated H_2BiPc β values are higher than their monomeric H_2Pc isomers, with C_{4h} symmetry isomers found to have highest β value of $34.0 \times 10^{-5} m.MW^{-1}$ in DCM solvent (Pcs in Section B above).

Table 3.5: Experimental and theoretical *z-scan* results for second-order nonlinear polarizability, β, in THF. DFT calculated values at B3LYP functional and SDD basis set.

Details *Possible Symmetries*	**Q_0**	**Z_R (mm)**	**β× 10^{-5} (m/MW^{-1}) (exp.)**	**β× 10^{-28} (esu) (Theor.)**	**$\phi_{J=1}$**	**$\phi_{J=3}$**
Biph–H_2BiPc – 1 *C4h:C4h* *D2h:D2h*	0.851	5.73	**72.2**	**10.0**	**0.2449**	0.7551
				8.09	**0.3239**	0.6761
Biph–H_2BiPc – 2 *Cs:Cs* *C2v:C2v*	0.398	6.21	**36.5**	**9.62**	**0.2227**	0.7772
				5.42	**0.7204**	0.2796
Biph–NiBiPc – 1 *C4h:C4h* *D2h:D2h*	1.90	3.61	**38.6**	**8.80**	**0.2932**	0.7068
				5.58	**0.4999**	0.5000
Biph–NiBiPc – 2 *Cs:Cs* *C2v:C2v*	0.117	3.46	**6.00**	**3.23**	**0.6176**	0.3824
				10.4	**0.3262**	0.6738
Naph–H_2BiPc – 1 *C4h:C4h* *D2h:D2h*	1.20	4.63	**82.6**	**3.64**	**0.1716**	0.8284
				11.0	**0.5245**	0.4754
Naph–H_2BiPc – 2 *Cs:Cs* *C2v:C2v*	1.12	2.86	**47.5**	**10.5**	**0.6028**	0.3972
				3.51	**0.1767**	0.8233
Naph–NiBiPc – 1 *C4h:C4h* *D2h:D2h*	0.320	5.26	**24.9**	**3.85**	**0.1970**	0.8030
				5.28	**0.2442**	0.7558
Naph–NiBiPc – 2 *Cs:Cs* *C2v:C2v*	0.555	3.88	**31.9**	**4.36**	**0.2628**	0.7372
				5.68	**0.7394**	0.2606

The nickel metalated version of the fractions above are represented as Biph-NiBiPc-1, Biph-NiBiPc-2, Naph-NiBiPc-1 and Naph-NiBiPc-2, see **Table 3.5**. Upon metalation the β values of $38.6 \times 10^{-5} m.MW^{-1}$ and $6.0 \times 10^{-5} m.MW^{-1}$ where obtained for Biph-NiBiPc-1 and Biph-NiBiPc-2 respectively. Compared to their unmetalated counter part, both Biph-NiBiPc-1 and Biph-NiBiPc-2 showed an increase in β value. Similarly upon metalation Naph-H_2BiPc-1 and Naph-H_2BiPc-2 fractions showed β values of $24.9 \times 10^{-5} m.MW^{-1}$ and $31.9 \times 10^{-5} m.MW^{-1}$ respectively. Both Naph-H_2BiPc-1 and Naph-H_2BiPc-2 show a decrease in β values compared to their unmetalated counterpart. The β value trend for nickel substituted BiPcs is summarised as follows Biph-NiBiPc-1 > Naph-NiBiPc-2 > Naph-NiBiPc-1 > Biph-NiBiPc-2. Overall the experimental β value for Naph-H_2BiPc-1 was found to be the highest compared to other BiPcs studied in this work. The general reduction in β value upon metalation is attributed to the interaction of unfilled d orbitals of Ni(II) with the large π-electron system of BiPcs, as observed for other NiPc reported on literacture [146, 147]. The interaction creates pathways for fast nonradiative excited state deactivation through internal conversion [146, 147]. H-aggregation is generally undesirable due to the strong intermolecular interactions which usually add relaxation pathways, shorten excited state lifetime and reduce the effective nonlinear absorption [148]. However despite the aggregation oberved for BiPcs studied in this work, the β values observed are within range or better than β values of monomeric Pcs studied in literature [116]. The above suggest that BiPcs studied in this work have potential of overcoming the primary barrier to further improvement of the optical limiting perfomance of the Pc based material.

3.7. Density functional theory calculations for binuclear phthalocyanines

In order to rationalise the β values observed above, β values of high and low symmetry BiPc isomers where theoretically calculated (see **Table 3.5**). All DFT calculations were carried out using SDD basis set at B3LYP level of theory, with hydroxyl group substituted in place of 4-*tert*-butylphenoxy group. There are ten different possibilities for tetra-substituted binuclear phthalocyanine molecules that could result from mixed condensation synthesis (**Table 3.6**). The symmetry (based on the substitution pattern for the metal-free molecules) of the BiPcs can be listed as shown in the table below.

Table 3.6: Possible combinations of binuclear phthalocyanine isomers.

	1	**2**	**3**	**4**	**5**	**6**	**7**	**8**	**9**	**10**
Left	C_{4h}	C_{2v}	C_s	D_{2h}	C_{4h}	C_{4h}	C_{4h}	C_{2v}	C_{2v}	C_s
Right	C_{4h}	C_{2v}	C_s	D_{2h}	C_{2v}	C_s	D_{2h}	C_s	D_{2h}	D_{2h}

The first four possible isomers (shaded in grey) were selected as a representative of high and low symmetry isomers in order to carry out DFT calculation. Hydroxyl groups where used as substituents in order to minimise calculation time.

Similar to molecules studied by Duncan et al. [74], BiPcs have the potential to transform their approximated D_{2h} symmetry to a D_2 or D_{2d} symmetry, by changing the angles (θ and ϕ) corresponding to the torsional relationship between their Pc units and the bridge least square plane [74]. The D_2 or D_{2d} symmetry, similar to D_{3h} or T_d symmetry are known to belong to octupolar molecules [149]. For BiPcs with a bridge torsional angle of $\theta = -\phi < 45^{\circ}$ correspond to D_2 symmetry, $\theta = -\phi = 45^{\circ}$ correspond to D_{2d} symmetry and $\theta = -\phi = 0^{\circ}$ correspond to D_{2h} symmetry [74]. NLO materials containing octupolar molecules are known to be less likely to undergo relaxation due to the lack of ground-state dipole moment [150, 151].

To serve as an example **Figure 3.24** shows the DFT optimize nickel naphthalene bridged bis-4-hydroxy binuclear phthalocyanine.

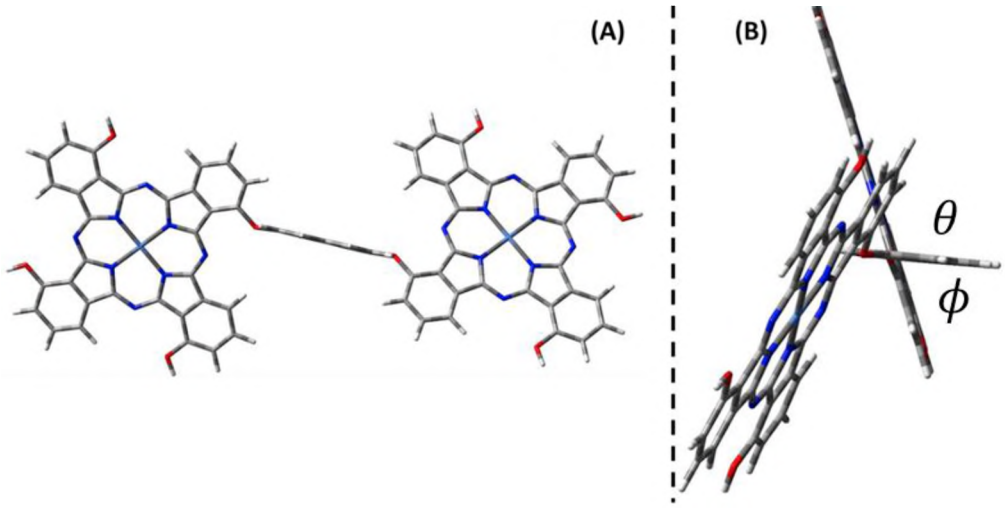

Figure 3.24: Front (**A**) and side (**B**) view of naphthalene bridged nickel bis-4-hydroxy binuclear phthalocyanine.

The angles θ and ϕ corresponding to the torsional relationship between the Pc units and the naphthalene bridged least square plane are measured to be $\theta = -\phi \approx 68^{\circ}$, which approximate a D_{2d} symmetry [74]. The Pc units with biphenyl bridged least square plane are measured to be $\theta = -\phi \approx 65^{\circ}$, approximating a D_{2d} symmetry. The above result suggest that the enhanced β value for both Biph-NiBiPc-1 (**15b)** and Naph-NiBiPc (**15d**) is also due to the approximation of the D_{2d} symmetry. Similar improvement in β value due to D_{2d} symmetry has been observed in literature [74]. The highly aggregated BiPc complexes suggest the measured β value is mainly due to the octupolar nature of the molecules, brought about by the tortional angle between the Pc units and the least square plane.

To further investigate the octupolar nature of the BiPcs and its effect on the NLO response, theoretical β values (see **Table 3.5**.) together with dipolar and octupolar ($\Phi_{J=1}$ and $\Phi_{J=3}$) contribution were calculated. **Table 3.5**, summaries the theoretically calculated β values for all the BiPcs. The theoretically determined β values shows a similar trend to experimental results

except for BiPcs possessing C_{2v}:C_{2v} symmetry and Naph-BiPc (C_{4h}:C_{4h} symmetry). In which unmetalated BiPcs (in Fraction 1 or 2) shows higher β values compared to their metalated couterpart. Upon metalation Naph-BiPc (C_{4h}:C_{4h} symmetry) and BiPcs possessing C_{2v}:C_{2v} symmetry, for both Biph-BiPc and Naph-BiPc, showed an increase in theoretical β values. The differences observed in theoretically determined β values, upon metalation, suggest that nickel interacts differently with a given symmetry of a BiPc. The observed theoretical trend for BiPcs possessing C_{2v}:C_{2v}, in comparison to experimental β value trend, suggest that the relative percentage of C_s:C_s isomer in Fraction 2 mixture is higher.

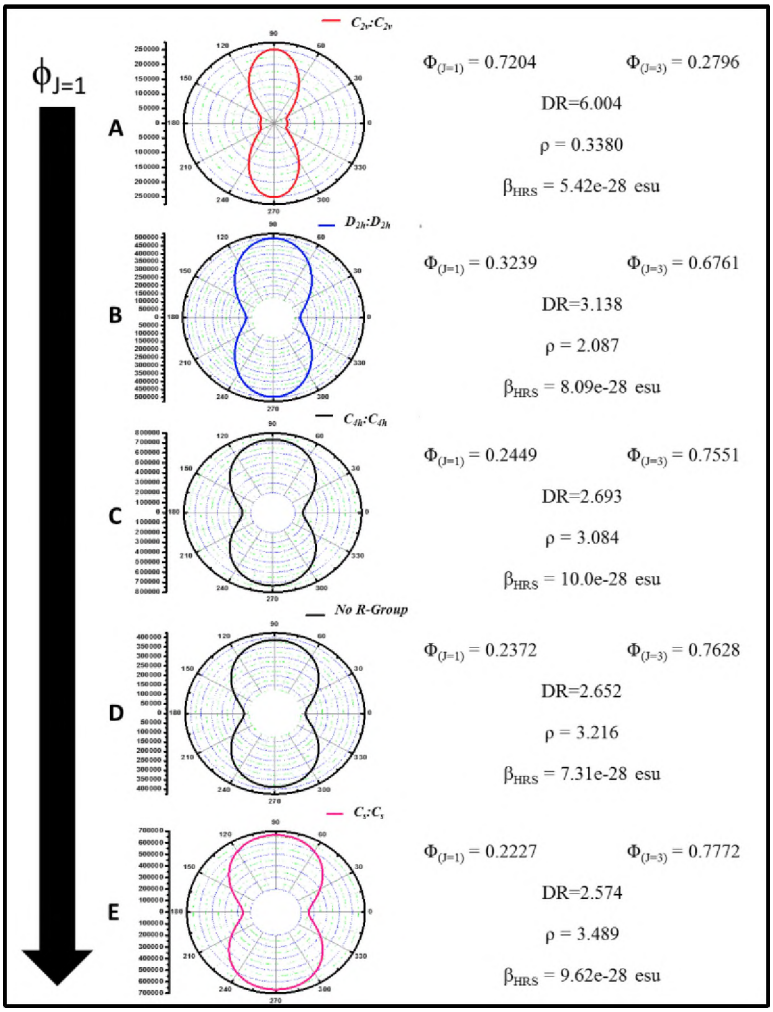

Scheme 3.7: Harmonic light intensity as a function of the polarisation angle ψ by polar representation of Biphy-H_2BiPc-2 (C_{2v}:C_{2v}) (A), Biphy-H_2BiPc-1 (D_{2h}:D_{2h}) (B), Biphy-H_2BiPc-1 (C_{4h}:C_{4h}) (C), unsubstituted Biphy-H_2BiPc (D) and Biphy-H_2BiPc-1 (C_s:C_s) (E).

Scheme 3.7, above shows the harmonic light intensity as a function of the polarisation angle ψ by polar representation of Biphy-H_2BiPc-2 (C_{2v}:C_{2v}) (A), Biphy-H_2BiPc-1 (D_{2h}:D_{2h}) (B), Biphy-H_2BiPc-1 (C_{4h}:C_{4h}) (C), unsubstituted Biphy-H_2BiPc (D) and Biphy-H_2BiPc-1 (C_s:C_s) (E) in the order of decreasing depolarization ratio (DR) **(**see **appendix** for **Biph-NiBiPc and Naph-H_2BiPc, Scheme 6.1-6.3)**. The DR values are sensitive to the structural properties of the molecule. The dipolar/octupolar contribution ($\phi_{J=1}$ and $\phi_{J=3}$) to β values where calculated for all the isomers selected and are all tabulated in **Table 3.5**. The DR value coincide with the dipolar or octupolar contribution for all BiPcs studied in this work, **Scheme 3.7** serves as an example. A depolarization ratio of 1.5 corresponds to purely octopolar contributions to the NLO signal, while a value of 5 corresponds to purely dipolar contributions [152]. The DR values trend calculated for Biph-H_2BiPc isomers and H_2Pc, shown in **Scheme 3.7**, are observed to follow the following trend, Biphy-H_2BiPc-2 (C_{2v}:C_{2v})> Biphy-H_2BiPc-1 (D_{2h}:D_{2h})> Biphy-H_2BiPc-1 (C_{4h}:C_{4h})> Biph-H_2BiPc>Biphy-H_2BiPc-1 (C_s:C_s). The above trend suggest that the Biphy-H_2BiPc-2 (C_{2v}:C_{2v}) has more dipolar contributions to the NLO signal compared to all other isomers studied in this work and Biphy-H_2BiPc-1 (C_s:C_s) has more octupolar contribution to NLO signal. However Biph-NiBiPc isomers DR values followed a different trend whereby Biphy-NiBiPc-1 (C_s:C_s)> Biphy-NiBiPc-1 (D_{2h}:D_{2h})> Biphy-NiBiPc-2 (C_{2v}:C_{2v})> Biphy-NiPcBiPc-1 (C_{4h}:C_{4h})>Biph-NiBiPc. The above observation suggest that insertion of nickel has a different effect for different isomers resulting in different dipolar/octupolar contributions to the NLO signal. Naph-H_2BiPc isomers DR values followed the following trend Naph-H_2BiPc-1 (C_s:C_s)> Naph-H_2BiPc-1 (D_{2h}:D_{2h})> Naph-H_2BiPc-2 (C_{2v}:C_{2v})> Naph-H_2BiPc-1 (C_{4h}:C_{4h})>Naph-H_2BiPc, which is a similar trend to that of Biph-NiBiPcs. Once again metalation of Naph-H_2BiPc resulted in a different trend being observed, Naph-NiBiPc-2 (C_{2v}:C_{2v})> trend Naph-NiBiPc-1 (C_s:C_s)> Naph-H_2BiPc-1 (D_{2h}:D_{2h})>Naph-NiBiPc> Naph-H_2BiPc-1 (C_{4h}:C_{4h}). The above results suggest that the linker or bridge between the Pc units affects the dipolar/octupolar contributions to the NLO signal.

Chapter 4

Conclusions

4. Conclusions

This chapter summaries all the results obtained for the mononuclear and binuclear phthalocyanines studied in this thesis.

4.1. General conclusions

The four positional isomers of metal free 4α-(4-*tert*-butylphenoxy)phthalocyanine have been successfully separated. The UV/vis absorption and MCD spectroscopy of the monomeric forms of the isomers have been studied. The fluorescence lifetimes of ~5 ns in DCM are similar in each case, and the D_{2h}, C_{4h} and C_s isomers have rotational times in the range of ~0.3 ns, while the C_{2v} isomer has a longer rotational time of ~0.6 ns. The viscosity values calculated on this basis, predict that the C_{2v} isomer has a greater viscosity value due to a greater interaction with the solvent molecules. Since TD-DFT calculations predict that the optical spectra of the four isomers are very similar, symmetry-sensitive *Z*-scan measurements were used to assign the different isomers by making use of the DFT calculated β values. These follow a similar trend to the experimentally derived γ values that were determined for each isomer. While the C_{4h} isomer displays an enhanced NLO response in terms of both the β and γ values compared to the other isomers, smallest NLO response were observed for the D_{2h} and C_s isomers, respectively. Solid state UV/vis absorption spectroscopy and UPS data provide further support to the symmetry assignments.

Unmetalated and nickel metalated Biph-BiPc and Naph-BiPc were successfully synthesised and characterised. The electronic absorption, MCD and fluorescence properties of these compounds were studied accordingly. The fluorescence lifetimes were determined to be in the range between ~1.4 – 5 ns, which is in accordance with literature values for Pcs. Using *Z*-scan, the highest and lowest β values for unmetaled BiPcs **15a** and **15c** were 72.2×10^{-5} m/W, 36.5×10^{-5} m/W and 82.6×10^{-5} m/W, 47.5×10^{-5} m/W respectively, compared to their nickel

counterparts **15b** and **15d** with β values of 38.6×10^{-5} m/W, 6.00×10^{-5} m/W and 24.9×10^{-5} m/W, 31.9×10^{-5} m/W respectively. High β values have been assigned to mixed isomers with high symmetry except for Naph-NiBiPc-1. The theoretically determined β values were further analysed according to their dipolar and octupolar ratio contributions. The presence of H-aggregation in these BiPcs does not have a significant effect on β as compared to H_2Pcs. In addition, the central metal in metalated compounds does not significantly affect the dipolar/octupolar contribution. Hence the experimentally observed higher β values for BiPcs could be attributed to the increased octupolar nature. The improvement in BiPcs β values from H_2Pc is also attributed to D_{2d} symmetry approximation.

5. References

[1] A. Braun, J. Tcherniac, Ber. Dtsch. Chem. Ges, 40 (1907) 2709.

[2] H. de Diesbach, E. von der Weid, Helv. Chim. Acta, 10 (1927) 886.

[3] R.P. Linstead, Br. Asso. Adv. Sci. Rep, (1933) 465.

[4] A.G. Dandridge, H.A.E. Drescher, J. Thomas, Dyes British Patent, 322 (1929) 169.

[5] R.P. Linstead, J. Chem. Soc, (1934) 1016.

[6] R.P. Linstead, A.R. Lowe, J. Chem. Soc, (1934) 1031.

[7] J.M. Robertson, J. Chem. Soc, (1935) 615.

[8] A. Y. Tolbin, V.E. Pushkarev, E.V. Shulishov and L.G. Tomilova, J. Porph. and Phthalocyan., 16 (2012) 341.

[9] M. Gouterman, J. Mol. Spec, 6 (1961) 138.

[10] S.P. Singh, S. Emin, and A. Loukanov, Adv. Mater. Lett. 1(2) (2010) 149.

[11] C.C. Leznoff and Lever, A. P. B., Eds.; VCH: Vol. 1(1989); Vol. 2 (1992); Vol. 3 (1993); Vol. 4 (1996), New York.

[12] C.G. Claessens, W. J. Blau, M. Cook, M. Hanack, R.J.M. Nolte, T. Torres and Dieter Wohrle, Monatshefte fur Chemie, 132 (2001) 3.

[13] G. Torres, P. Vazquez, F. Agullo-Lopez and T. Torres, Chemistry Review, 104 (2004) 3723.

[14] M.J. Cook, A.J. Dunn, S.D. Howe, A.J. Thomson, K.J. Harrison, J. Chem. Soc. Perkins Transcations, 1 (1988) 2453.

[15] M. Hanack, G. Schmid and M. Sommerauer, Angew. Chem., 32 (1993) 1422.

[16] M. Sommerauer, C. Rager and M. Hanack, J. Am. Chem. Soc., 118 (1996) 10085.

[17] J. Mack and N. Kobayashi, Chem. Rev., 111 (2011) 281.

[18] Y. Chen, M. Hanack, W.J. Balu, D. Dini, Y. Liu, Y. Lin and J. Bai, J. Mater. Sci., 41 (2006) 2169.

[19] K. Sanusi, E. Antunes and T. Nyokong, Dalton Trans., 43 (2014) 999.

[20] E.S. Dodsworth, A.B.P. Lever, P. Seymour and C.C. Leznoff, J. Phys. Chem., 89 (1985) 5698.

[21] Z. Chen, L. Niu, Y. Cheng, X. Zhou, C. Zhang and F. Zhang, Dalton Trans., 40 (2011) 393.

[22] R. D. George, A. W. Snow, J. S. Shirk, W. R. Barger, Journal of Porphyrins and Phthalocyanines, 2 (1998) 1.

[23] E.E. Jelly, Nature, 139 (1937) 631.

[24] G. Scheibe, Angew. Chem., 50 (1937) 212.

[25] Z.S. Wang, K. Hara, Y. Dan-Oh, C. Kasada, A. Shinpo, S. Suga, H. Arakawa and H. Sugihara, J. Phys. Chem. B., 109 (2005) 3907.

[26] A. Satake and Y. Kobuke, Org. Biomol. Chem., 5 (2007) 1679.

[27] T. Kobayashi, J. Du and Y. Kida, World Scientific, Chp. 1 (1996) 1.

[28] S. Chakraborty, P. Debnath, D. Dey, D. Bhattacharjee, S.A. Hussain, J. Photochem. Photobiol. A, 293 (2014) 57.

[29] X.-F. Zhang, Q. Xi and J. Zhao, J Mater. Chem., 20 (2010) 6726.

[30] G. Zengin, G. Johansson, P. Johansson, T.J. Antosiewicz, M. Käll and T. Shegai, Scient. Reports, (2013) DOI:10.1038/srep3074.

[31] N.B. McKeown, Ed. Phthalocyanine Materials, Synthesis, Structure and Function, Cambridge University Press: Cambridge, 1998.

[32] M.S. Khene, Synthesis, Photophysics and electrochemical study of tin macrocycles, MSc Thesis, Rhodes University (2008).

[33] G. de la Torre, P. Vázquez, F. Agulló-López and T. Torres, Chem. Rev., 104 (2004) 3723.

[34] M. Calvete, Binuclear phthalocyanines: Synthesis, characterisation and optical limiting properties, MSc Dissertation, der Eberhand-Karls-Universität Tübingen (2004).

[35] C.C. Leznoff, H. Lam, S.M. Marcuccio, W.A. Nevin, P. Janda, N. Kobayashi and A.B.P. Lever, J. Chem. Soc. (1987) 699.

[36] S. Vigh, H. Lam, P. Janda, A.B.P. Lever and C.C. Leznoff, Can. J. Chem., 69 (1991) 1457.

[37] I. Seotsanyana-Makhosi, S. Maree, M. D. Maree and T. Nyokong, J Porph. Phthaloc., 7 (2003) 167.

[38] A.Y. Tolbin, A.V. Ivanov, L.G. Tomilova and N.S. Zefirov, J Porph. Phthaloc., 7 (2003) 162.

[39] T.W. Hall, S. Greenberg, C.R. McArthur, B. Khouw and C.C. Leznoff, Nouv. J. Chim., 6 (1982) 653.

[40] X. Peng, D.R. Draney and J. Chen, United States Patent (2006).

[41] F. Baumann, B. Bienert, G. Rösch, H. Voliman, W. Wolf, Angew. Chem., 68 (1965) 133.

[42] S.W. Oliver and T.D.J. Smith, J. Chem. Soc., Perkin Trans. II, (1987) 1579.

[43] A.M. D'Ascanio, A study of solvent and metal effects on the formation of phthalocyanines at room temperature, MSc thesis, York University Toronto (1999).

[44] M.G. Kuzyk, Nonlinear Optics, Chapter 1 (2010) 1.

[45] P. Neethling, Determining nonlinear optical properties using the z-scan technique, Thesis, University of Stellenbosch (2005).

[46] F. Pan, K. McCallion and M. Chiappetta, Appl. Phys. Lett., 74 (1999) 492.

[47] T. Kaino, B. Cai and K. Takayama, Adv. Funct. Mater., 12 (2002) 599

[48] W. Geis, R. Sinta, W. Mowers, S.J. Deneault, M.F. Marchant, K.E. Krohn, S.J. Spector, D.R. Calawa and M. Lyszczarz, Appl. Phys., 84 (2004) 3729.

[49] L.R. Dalton, Pure Appl. Chem., 76 (2004) 1421.

[50] Y. Shi, C. Zhang, H. Zhang, J.H. Bechtel, L.R. Dalton, B.H. Robinson, W.H. Steier, Science, 288 (2000) 119.

[51] H. Ma, A.K.Y. Jen and L.R. Dalton, Adv. Mater., 14 (2002) 1339.

[52] G. de la Torre, P. Vázquez, F. Agulló-López, T. Torres, J. Mater. Chem., 8 (1998) 1671.

[53] H.M. Kim and B.R. Cho, J. Mater. Chem., 19 (2009) 7402.

[54] L. Zhang, D. Qi, L. Zhao, C. Chen, Y. Bian and W. Li, J. of Phys. Chem., 116 (2012) 10249.

[55] C. Wang, C. Chen, Q, Zhang, D. Qi and J. Jiang, Tur. J. Chem., 38 (2014) 1046.

[56] J. M. Fox, T. J. Katz, S. V. Elshocht, T. Verbiest, M. Kauranen, A. Persoons, T. Thongpanchang, T. Krauss, L. Brus, J. Am. Chem. Soc., 121 (1999) 3453.

[57] A. Plaquet, M. Guillaume, B. Champagne, F. Castet, L. Ducasse, J. Pozzo and V. Rodriguez, Phys. Chem. Chem. Phys., 10 (2008) 6223.

[58] F. Castet, E. Bogdan, A. Plaquet, L. Ducasse, B. Champagne, and V. Rodriguez, J. Chem. Phys., 136 (2012) 024506.

[59] P. C. Ray, Chem Rev.,110 (2010) 5332.

[60] T. Verbiest, S. Houbrechts, M. Kauranen, K. Clays, A. Persoons, J. Mater. Chem., 7 (1997) 2175.

[61] E. M. Maya, A. W. Snow, J. S. Shirk, R. G. S. Pong, S. R. Flom, G. L. Roberts, J. Mater. Chem., 13 (2003) 1603.

[62] M. A. Diaz-Garcia, J. Porphyrins Phthalocyanines, 13 (2009) 652.

[63] B. Sheehy, L.F. Di-Mauro, Ann. Rev. Phys. Chem., 47 (1996) 463.

[64] J. Britton, M. Durmus S. Khene, V. Chauke, T. Nyokong, J. Porphyrins Phthalocyanines, 17 (2013) 691.

[65] C. Mkhize, J. Britton, T. Nyokong, Polyhedron, 81 (2014) 607.

[66] J. Britton, M. Durmuş, V. Chauke, T. Nyokong, J. Mol. Struct., 1054-1055 (2013) 209.

[67] E. Garmire, Overview of Nonlinear Optics, Nonlinear Optics, Dr. N. Kamanina (Ed.) Chp.1, (2012) 3.

[68] D. Dini, M. Hanack, H.-J. Egelhaaf, J.C. Sancho-García and J. Cornil, J. Phys. Chem. B, 109 (2005) 5425.

[69] J. Wang, Y. Chen, R. Li, H. Dong, L. Zhang, M. Lotya, J.N. Coleman and W.J. Blau, Nonlinear Optical Properties of Graphene and Carbon Nanotube Composites, Carbon

Nanotubes – Synthesis, Characterisation, Applications, Dr. S. Yellampalli (Ed.), Chp. 19 (2011) 397.

[70] G.Y. Yang, M. Hanack, Y.W. Lee, Y. Chen, M.K.Y. Lee and D. Dini, Chem. Eur. J., 9 (2013) 2758.

[71] J. Britton, E. Antunes and T. Nyokong, J. Molec. Struc., 1047 (2013) 143.

[72] P.W. Milonni, J. Phys B: Atomic, molecular and optical physics, 35 (2002) R31.

[73] K. Clays and A. Persoons, Phys. Rev. Lett., 66 (1991) 2980.

[74] T.V. Duncan, K. Song, S.-T. Hung, I. Miloradovic, A. Nayak, A. Persoons, T. Verbiest, M.J. Therien and K. Clays, Angew. Chem., 120 (2008) 3020.

[75] Y.-C. Shen, Z. Tang, M. Gui, J. Cheng, X. Wang and Z. Lu , Chem. Lett., (2000) 1140.

[76] F. W. Vance and J. T. Hupp, J. Am. Chem. Soc., 121, (1999) 4047; C. Boutton, K. Clays, A. Persoon, T. Wada, and H. Sasabe, Chem. Phys. Lett., 286, (1998) 101; J. A. Sattigeri, C. W. Shiau, C. C. Hsu F. F. Yeh, S. Liou, B. Y. Jin, and T. Y. Luh, J. Am. Chem. Soc., 121 (1999) 1607.

[77] K. Clays, E. Hendrick, M. Triest, T. Verbiest, A. Persoons, C. Dehu, and J.-L. Bredas, Science, 262 (1993) 1419.

[78] P. Galletto, P. F. Brevet, H. H. Girault, R. Antoine, and M. Broyer, Chem. Commun., (1999) 581.

[79] P. Tau, T. Nyokong, Electrochim, Acta, 52, 11 (2007) 3641.

[80] M.-R. Ke, J.-D. Huang and S.-M. Weng, J. Photochem. And Photobio. A: Chemistry 201 (2009) 23.

[81] Z. Biyiklioğ lu and I. Acar, Syn. Metals 162 (2012) 1156.

[82] P.Apostol, A. Bentaleb, M. Rajaoarivelo, R. Clérac and H. Bock, Dal. Trans. 44 (2015) 5569.

[83] K. Sanusi, E.K. Amuhaya and T. Nyokong, J. Phys. Chem. C, 118 (2014) 7057.

[84] O.M. Bankole and T. Nyokong, J. Coord. Chem., 68 (2015) 3727.

[85] R.S.S. Kumar, S.V. Rao, L. Giribabu and D.N. Rao, Prov. SPIE, 6875 (2008) 68751D.

[86] C. Nitschke, S. M. O'Flaherty, M. Kroll, J. J. Doyle, W. J. Blau, Chem. Phys. Lett., 383 (2004) 555.

[87] T. Verbiest, S. V. Elshocht, A. Persoons, C. Nuckolls, K. E. Phillips, T. J. Katz, Langmuir, 17 (2001) 4685.

[88] Z. Li, Y. Liu, H. Kim, J.M. Hales, S.H. Jang, J. Luo, T. Baehr-Jones, M. Hochberg, S.R. Marder, J.W. Perry, A.K.-Y. Jen, Adv. Mater., 24 (2012) OP326.

[89] S. D. Bella, Chem. Soc. Rev., 30 (2001) 355.

[90] Y. Chen, M.E. El-Khouly, J.J. Doyle, E.G.A. Notaras, W.J. Blau and S.M. O'Flaherty (2006) 1.

[91] C.G. Claessens, D. González-Rodriguez, T. Torres, G. Martín, F. Agulló-López, I. Ledoux, J. Zyss, V.R. Ferro and J.M. García de la Vega, J. Phys. Chem. B, 109 (2005) 3800.

[92] G. de la Torre, G. Bottari, M. Sekita, A. Housmann, D.M. Guldi and T. Torres, Chem. Soc. Rev., 42, (2013) 8049.

[93] H. Yoshiyama, N. Shibata, T. Sato, S. Nakamura and T. Toru, Organic and Bimolecular Chemistry, 6 (2008) 4498.

[94] L.-C. Liu, C.-H. Tai, A.T. Hu and T.-H. Wei, J. Porphy. Phthaloc., 8 (2004) 984.

[95] K.P. Unnikrishnan, J.Thomas, V.P.N. Nampoori and C.P.G. Vallabhan, Appl. Phys. B, 75 (2002) 871.

[96] K.E. Sekhosana, E. Amuhaya, J. Mack and T. Nyokong, J. Mater. Chem C, 2 (2014) 5431.

[97] K.E. Sekhosana and T. Nyokong, Opt. Mater., 47 (2015) 211.

[98] J. Mack, M.J. Stillman and N. Kobayashi, Coodination Chemistry Reviews, 251 (2007) 429.

[99] N. Kobayashi and K. Nakai, Chem. Commun., (2007) 4077.

[100] F. Paulat and N. Lehnert, Inorg. Chem., 47 (2008) 4963.

[101] J. Mack, X. Liang, T.V. Dubinina, L.G. Tomilova, T. Nyokong and N. Kobayashi, J. Porphy. Phthaloc., 17 (2013) 489.

[102] J. Mack and M.J. Stillman, Coordination Chemistry Reviews, 219-221 (2001) 993-1032.

[103] J.R. Lakowicz, Principles of Fluorescence Spectroscopy, Chapter 1, 3rd edition (2006) 1-26.

[104] A. Jablonski, Nature, (1933) 839.

[105] J.R. Lakowicz, Principles of Fluorescence Spectroscopy, Chapter 7, 3rd edition (2006)

[106] S. Tombe, E. Antunes and T. Nyokong, New J. Chem., 37 (2013) 679.

[107] L. Ma, Y. Zhang and P. Yuan, Optics Express, 18 (2010) 17666.

[108] E.W. van Stryland and M. Sheik-Bahae, Characterisation Techniques and Tabulations for Organic Nonlinear Materials, M.G. Kuzyk and C.W. Dirk (Eds.) (1998) 655.

[109] M.Sheik-Bahae, A.A. Said and E.E. van Stryland, Opt. Lett., 14 (1989) 955.

[110] C-K. Chang, Y-C. Li, C-W. Chen, L-S. Lee, J-L. Tang, C-C. Wang, C-C. Leu, T-H. Wei, T-H. Huang and Y. Song, J. Chem. Phys., 130 (2009) O24511.

[111] G. Tsigaridas, I. Polyzos, P. Persephonis, V. Giannetas, Opt. Commun., 266 (2006) 284.

[112] M. Sheik-Bahae, A. A. Said, T. H. Wei, D, J. Hagan, E. W. Van Stryland, IEEE J. Quantum Elect., 26 (1990) 760.

[113] M. Kandaz, Ali R. Özkaya, and Özer Bekaroğlu, Monatsh. Chem., 132 (2001) 1013-1022.

[114] M. J. MacLachlan. in Frontiers in Transition Metal-Containing Polymers, ed. A. S. Abd-El-Aziz and I. Manners, Wiley & Sons, New York (2007) 208-216.

[115] E. M. García, S. M. O'Flaherty, E. M. Maya, G. de la Torre, W. Blau, P. Vázqueza and T. Torres, J. Mater. Chem., 13 (2003) 749.

[116] D. Dini and M. Hanack. In The Porphyrin Handbook: Physical Properties of Phthalocyane-based Materials, Vol. 17, K. M. Kadish, K. M. Smith and R. Guilard (Eds.) Academic Press: USA (2003) 22-31.

[117] J. Simon and C. Sirlin, Pure Appl. Chem., 61 (1989) 1625.

[118] P.S. Liyanage, R.M. de Silva, K.M.N. de Silva, J. Mol. Struct. (Theochem.), 639 (2003) 195.

[119] M.J. Frisch, G.W. Trucks, H.B. Schlegel, G.E. Scuseria, M.A. Robb, J.R. Cheeseman, J.A. Montgomery Jr., T. Vreven, K.N. Kudin, J.C. Burant, J.M. Millam, S.S. Iyengar, J. Tomasi, V. Barone, B. Mennucci, M. Cossi, G. Scalmani, N. Rega, G.A. Peters son, H. Nakatsuji, M. Hada, M. Ehara, K. Toyota, R. Fukuda, J. Hasegawa, M. Ishida, T. Nakajima, Y. Honda, O. Kitao, H. Nakai, M. Klene, X. Li, J.E. Knox, H.P. Hratchian, J.B. Cross, V. Bakken, C. Adamo, J. Jaramillo, R. Gomperts, R.E. Stratmann, O. Yazyev, A.J. Austin, R. Cammi, C. Pomelli, J.W. Ochterski, P.Y. Ayala, K. Morokuma, G.A. Voth, P. Salvador, J.J. Dannenberg, V.G. Zakrzewski, S. Dapprich, A.D. Daniels, M.C. Strain, O. Farkas, D.K. Malick, A.D. Rabuck, K. Raghavachari, J.B. Foresman, J.V.D.J. Fox, T. Keith, M.A. Al-Laham, C.Y. Peng, A. Nanayakkara, M. Challacombe, P.M.W. Gill, B. Johnson, W. Chen, M.W. Wong, C. Gonzalez, J.A. Pople, Gaussian 03, Revision E.01, Gaussian Inc., Wallingford, CT, (2004).

[120] Gaussian 09, Revision D.01, M. J. Frisch, G. W. Trucks, H.B. Schlegel, G. E. Scuseria, M. A. Robb, J. R. Cheeseman, G. Scalmani, V. Barone, B. Mennucci, G. A. Petersson, H. Nakatsuji, M. Caricato, X. Li, H. P. Hratchian, A. F. Izmaylov, J. Bloino, G. Zheng, J. L. Sonnenberg, M. Hada, M. Ehara, K. Toyota, R. Fukuda, J. Hasegawa, M. Ishida, T. Nakajima, Y. Honda, O. Kitao, H. Nakai, T. Vreven, J. A. Montgomery, Jr., J. E. Peralta, F. Ogliaro, M. Bearpark, J. J. Heyd, E. Brothers, K. N. Kudin, V. N. Staroverov, R. Kobayashi, J. Normand, K. Raghavachari, A. Rendell, J. C. Burant, S. S. Iyengar, J. Tomasi, M. Cossi, N. Rega, J. M. Millam, M. Klene, J. E. Knox, J. B. Cross, V. Bakken, C. Adamo, J. Jaramillo, R. Gomperts, R. E. Stratmann, O. Yazyev, A. J. Austin, R. Cammi, C. Pomelli, J. W. Ochterski, R. L. Martin, K. Morokuma, V. G. Zakrzewski, G. A. Voth, P. Salvador, J. J. Dannenberg, S. Dapprich, A. D. Daniels, Ö. Farkas, J. B. Foresman, J. V. Ortiz, J. Cioslowski, and D. J. Fox, Gaussian, Inc., Wallingford CT, (2009).

[121] T. Nyokong and E. M. Antunes, J. Porph. and Phthalocyan., 13 (2009) 153.

[122] J.R. Griffith and J.G. O'Rear, United States Patent, (1977).

[123] T. Nyokong, Z. Gasyna, M. J. Stillman, Inorg. Chem., 26 (1987) 548.

[124] T. Nyokong, Z. Gasyna, M. J. Stillman. Inorg. Chem., 26 (1987) 1087.

[125] E. A. Ough, T. Nyokong, K. A. M. Creber, M. J. Stillman, Inorg. Chem., 27 (1988) 2724.

[126] J. Mack, M. J. Stillman, J. Phys. Chem., 95 (1995) 7935.

[127] J. Mack, M. J. Stillman, Inorg. Chem., 36 (1997) 413.

[128] Z. Gasyna, N. Kobayashi, M. J. Stillman, J. Chem. Soc. Dalton Trans., (1989) 2397.

[129] J. Mack, N. Kobayashi, M. J. Stillman, J. Inorg. Biochem., , 102 (2010) 472.

[130] M. Gouterman, In The Porphyrins, vol. III, D. Dolphin (Ed.) Academic Press: New York (1978) 1–165.

[131] J. Michl, J. Am. Chem. Soc., 100 (1978) 6801.

[132] J. Michl, J. Am. Chem. Soc., 100 (1978) 6812.

[133] J. Michl, Pure Appl. Chem., 52 (1980)1549.

[134] J. Michl, Tetrahedron, 40 (1984) 3845.

[135] J. Mack, Y, Asano, N, Kobayashi, M. J. Stillman, J. Am. Chem. Soc., 127 (2005) 17697.

[136] N. Kobayashi, Y. Yanagisawa and C. C. Leznoff, Analytical Sciences, 6 (1990) 813.

[137] G. de la Torre, A. Gouloumis, P. Vázquez and T. Torres, Angew. Chem. Int. Ed., 40(15), 2001, 2895.

[138] N. Kobayashi and K. Nakai, Chem. Commun., (2007) 4077.

[139] N. Nombona, W. Chidawanyika and T. Nyokong, J. Mole. Struc., 1012 (2012) 31.

[140] J.W. Borst, M.A. Hink, A. van hoek and A.J.W.G. Visser, J. Fluores., 15 (2005) 153.

[141] G. Valduga, E. Reddi, G. Jori, J. Photochem. Photobiol. B, Biol., 16 (1992) 331.

[142] J. D Spikes, Photochem. Photobiol., 43 (1986) 691.

[143] P.T. Anusha, P. Silviya Reeta, L. Giribabu, Surya P. Tewari, S. Venugopal Rao, Material Letters, 64 (2010) 1915.

[144] M. G. Kuzyk and C. W. Dirk, Phys. Rev. A, 41 (1990) 5098.

[145] J. Zhu, Y. Li, Y. Chen, J. Wang, B. Zhang, J. Zhang, W. J. Blau, Carbon, 49 (2011) 1900.

[146] A. V. Soldatova, J. Kim, X. Peng, A. Rosa, G. Ricciardi, M. E. Kenney and M. A. J. Rodgers, Inorg. Chem., 46 (2007) 2080.

[147] A. V. Nikolaitchik and M. A. J. Rodgers, J. Phys. Chem. A, 103 (1999) 7597.

[148] J. S. Shirk, R. G. S. Pong, S. R. Flom, H. Heckmann and M. Hanack, J. Phys. Chem. A, 104 (2000) 1438.

[149] J. L. Bredas, F. Meyers, B. M. Pierce, J. Zyaa, J. Am. Chem. Soc., 114 (1992) 4928.

[150] M. Joffre, D. Yaron, R. J. Silbey, J. Zyss, J. Chem. Phys., 97 (1992) 5607.

[151] Mi-Yun Jeong and Bong Rae Cho, Chem. Rec., 15 (2015) 132.

[152] S. Deckers, J. Steverlynck, P. Willot, S. Vandendriessche, G. Koeckelberghs, I. Asselberghs, T. Verbiest, M. A. van der Veen J. Phys. Chem. C, 119 (2015) 18513.

6. Appendix

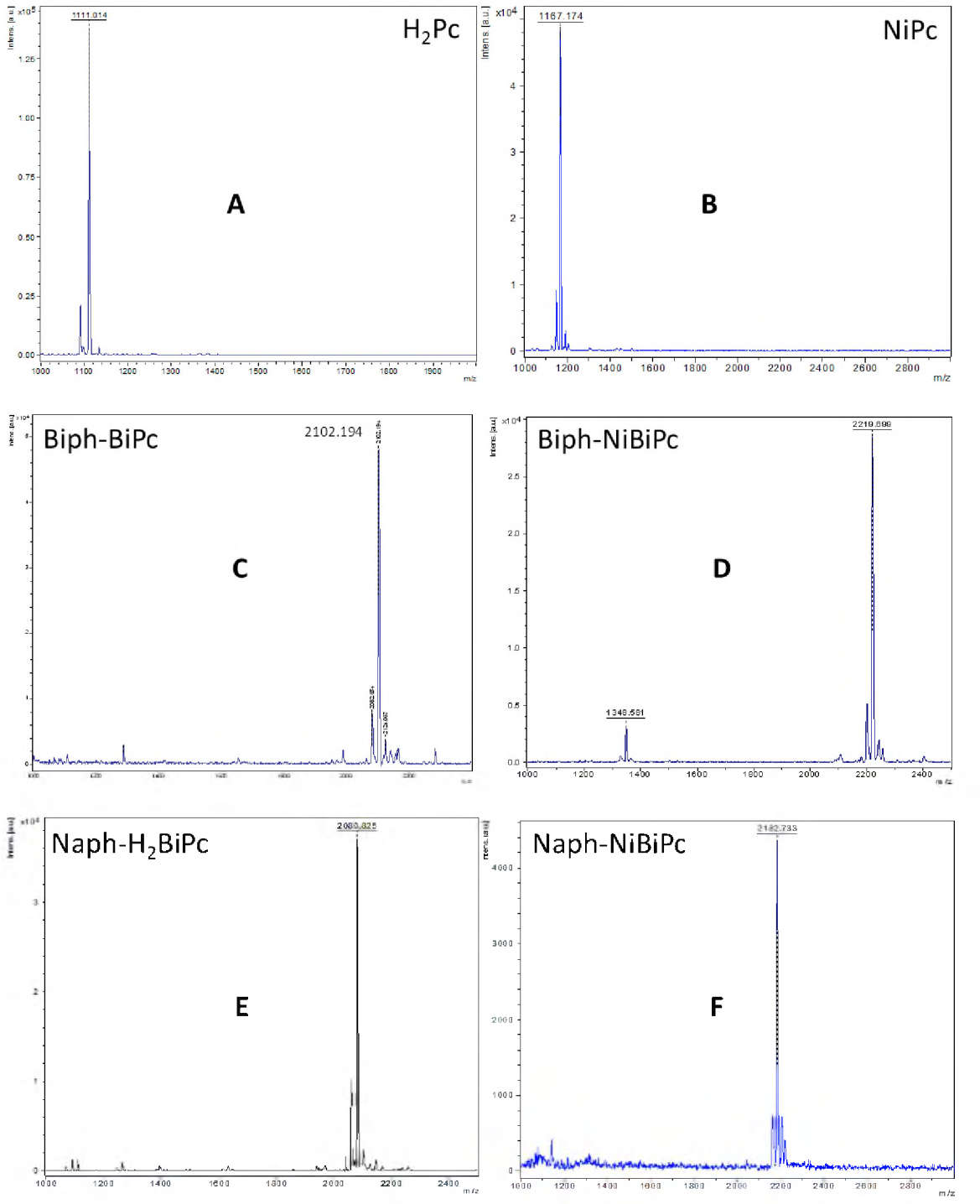

Figure 6.1: MS of H_2Pc **(A)**, NiPc **(B)**, Biph-H_2BiPc **(C)**, Biph-NiBiPc **(D)**, Naph-H_2BiPc **(E)** and Naph-NiBiPc **(F)**.

Table 6.1: TD-DFT spectra of the B3LYP optimized geometries of the four positional isomers of the $H_2(OH)_4Pc$ model compound calculated with the B3LYP functional and 6-31G(d) basis sets.

					C_{2v}		
Band[a]	**#[b]**		**Calc[c]**		**Exp[d]**		**Wavefunction=[e]**
--	**1**	---	---	---	---	---	Ground state
Q	**2**	15.8	632	(0.41)	13.9	714	**93% a → -a; 4% s → -s;** 3% H–6 ($2a_{2u}$) → -s; …
Q	**3**	16.0	626	(0.47)	14.6	683	**96% a → -s;** 3% H–6 ($2a_{2u}$) → -a; **2% s → -a;** …
B1	**9**	25.8	388	(0.14)	25.0	~400	**46% s → -s;** 24% H–3 ($1e_g$) → -a; …
B1	**15**	27.5	364	(0.01)			**74% s → -a;** …
B2	**17**	29.0	345	(0.26)	28.6	~350	38% H–8 ($2a_{1u}$) → -a; 38% H–6 ($2a_{2u}$) → -s; …
B2	**18**	29.2	342	(0.15)			38% H–8 ($2a_{1u}$) → -s; 36% H–6 ($2a_{2u}$) → -s; …
					C_{4h}		
Band[a]	**#[b]**		**Calc[c]**		**Exp[d]**		**Wavefunction=[e]**
--	**1**	---	---	---	---	---	Ground state
Q	**2**	15.8	632	(0.42)	13.9	719	**61% a → -a; 33% a → -s; 3% s → -s;** …
Q	**3**	16.0	624	(0.47)	14.6	689	**63% a → -s; 32% a → -a;** …
B1	**9**	25.9	386	(0.20)	25.0	~400	**70% s → -s;** 24% H–2 ($1b_{1u}$) → -a; …
B1	**15**	27.5	364	(0.01)			**77% s → -a;** …
B2	**17**	29.0	344	(0.27)	28.6	~350	53% H–7 ($2a_{1u}$) → -a; 41% H–6 ($2a_{2u}$) → -s; …
B2	**18**	29.3	342	(0.11)			56% H–7 ($2a_{1u}$) → -s; 39% H–6 ($2a_{2u}$) → -s; …
					C_s		
Band[a]	**#[b]**		**Calc[c]**		**Exp[d]**		**Wavefunction=[e]**
--	**1**	---	---	---	---	---	Ground state
Q	**2**	15.8	632	(0.41)	13.9	718	**92% a → -a; 4% s → -s;** 3% H–6 ($2a_{2u}$)

							→ -s; …
Q	**3**	16.0	626	(0.48)	14.5	688	**95% a** → **-s;** 3% H–6 ($2a_{2u}$) → -a; **2% s** → **-a;** …
B1	**9**	25.9	386	(0.19)	25.0	~400	**68% s** → **-s;** …
B1	**15**	27.4	364	(0.02)			**73% s** → **-a;** …
B2	**17**	29.0	345	(0.24)	28.6	~350	53% H–8 ($2a_{1u}$) → -a; 40% H–6 ($2a_{2u}$) → -s; …
B2	**18**	29.2	342	(0.10)			56% H–8 ($2a_{1u}$) → -s; 38% H–6 ($2a_{2u}$) → -s; …

				D_{2h}			
Band[a]	**#**[b]		**Calc**[c]		**Exp**[d]		**Wavefunction=**[e]
--	**1**	---	---	---	---	---	Ground state
Q	**2**	15.8	634	(0.40)	14.0	715	**79% a** → **-a; 15% a** → **-s; 4% s** → **-s;** 2% H–6 ($2a_{2u}$) → -s; …
Q	**3**	16.0	626	(0.49)	14.5	687	**81% a** → **-s; 15% a** → **-a; 2% s** → **-a;** 2% H–6 ($2a_{2u}$) → -a; …
B1	**9**	25.8	388	(0.23)	25.0	~400	**64% s** → **-s;** 13% H–2 ($1b_{1u}$) → -a; …
B1	**15**	27.3	366	(0.01)			**78% s** → **-a;** …
B2	**17**	29.0	345	(0.24)	28.6	~350	54% H–7 ($2a_{1u}$) → -a; 37% H–6 ($2a_{2u}$) → -s; …
B2	**19**	29.2	343	(0.10)			56% H–7 ($2a_{1u}$) → -s; 37% H–6 ($2a_{2u}$) → -s; …

a − Band assignment described in the text. b − The number of the state assigned in terms of ascending energy within the TD-DFT calculation. c − Calculated band energies (10^3 cm^{-1}), wavelengths (nm) and oscillator strengths in parentheses (f). d − Observed energies (10^3 cm^{-1}) and wavelengths (nm) in **Figure3.8**. e − The wave functions based on the eigenvectors predicted by TD-DFT. One-electron transitions associated with Michl's perimeter model [131-135] are highlighted in bold. H and L refer to the HOMO and LUMO, respectively. When the H and L nomenclature is used the symmetry label for the corresponding MO in the π-systems of D_{4h} MPc complexes is provided in parentheses where applicable.

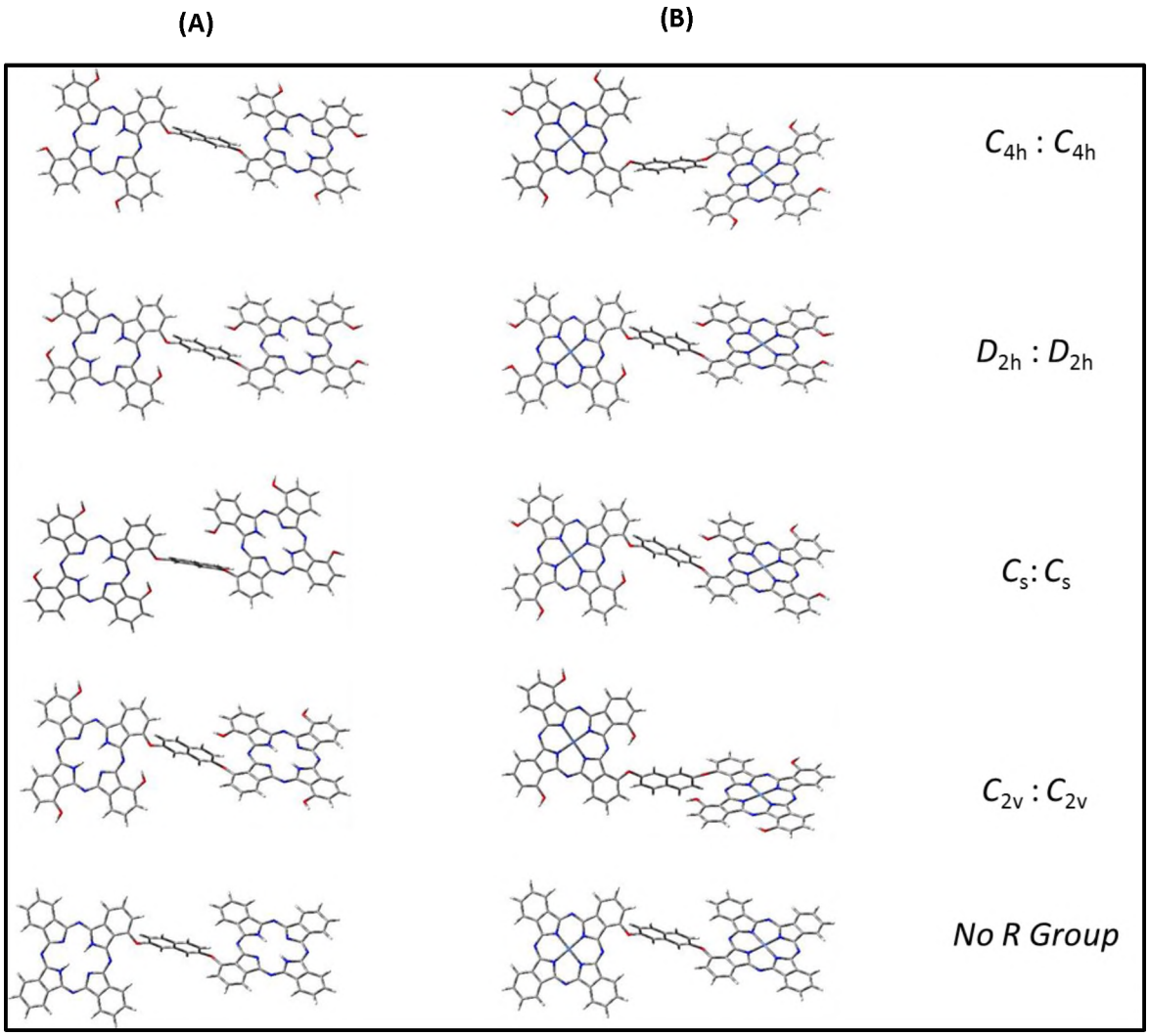

Figure 6.2: Optimised isomeric structures of Naph-H_2BiPc (A) and Naph-NiBiPc (B) with OH groups.

Table 6.2: TD-DFT spectra of the B3LYP optimized geometries of the model BiPc complexes calculated with the B3LYP functional and SDD basis sets.

Naphthyl H_2BiPc							
Band[a]	#[b]		**Calc[c]**		**Exp[d]**		**Wavefunction=[e]**
--	**1**	---	---	---	---	---	Ground state
Q	**3**	14.8	676	(0.84)	14.0	716	**82% a → -s; 3% a → -s; 11% a → -a**
	4	15.1	660	(0.21)			**77% a → -a, 10% a→ -s; 6% a → -a**
Q	**5**	15.3	653	(0.26)	15.6	687	**89% a → -s, 3% a → -s;** 2% H-5 ($_{eg}$) → -s
	6	15.6	640	(0.49)			**88% a → -a; 5% a → -a;** 2% H-7 (1_{a2u}) → -a
B1	**11**	21.1	473	(0.10)	25.0	~400	81% H-5 (e_g) → -s; **5% s → -s;** 4% H-5 (e_g) → -s; …
	12	23.6	423	(0.15)			20% H-9 (1_{a1u}) → -a; 22% (e_g) → -a; 5% H-5 (e_g) → a; …
	19	24.8	402	(0.11)	24.5	~350	44% H-9 (1_{a1u}) → -a, …
B2	**24**	24.9	402	(0.04)			51% H-7 (1_{a2u})
Naphthyl Nickel BiPc							
Band[a]	#[b]		**Calc[c]**		**Exp[d]**		**Wavefunction=[e]**
--	**1**	---	---	---	---	---	Ground state
Q	**8**	15.9	630	(0.84)	**14.5**	**688**	**79% a → -s; 8% a → -a; 7% a → -s;** 3% H-8 (1_{a2u}) → -a
	11	16.2	619	(0.18)			**62% a → -s; 24% a → -a; 4% a → -s;…**
Q	**12**	16.2	616	(0.26)			**83% a → -a; 9% a → -s; …**
	13	16.3	612	(0.45)			**88% a → -a; 3% a → -s; …**
B1	**29,32**	23.7	422	(0.02)	33.3	~300	36% H-10 (1_{a1u}) → -s; 24% s → -a; 15% H-10 (1_{a1u})→ -a; …
B2	**37,38**	25.0	404	(0.07)			32% H-8 (1_{a2u}) → -s; 24% H-8 (1_{a2u}) → -a; …
Biphenyl H_2BiPc							
Band[a]	#[b]		**Calc[c]**		**Exp[d]**		**Wavefunction=[e]**
--	**1**	---	---	---	---	---	Ground state
Q	**2**	12.8	783	(0.26)	14.0	716	**63% a → -s**
	3	13.0	766	(0.44)			**64% a → -s**
Q	**5**	13.8	723	(0.32)	14.5	688	**70% a → -a; 7% s → -s; …**
	7	15.1	664	(0.31)			**71% a → -a; 6% H-10 ($2e_g$) → -s; …**
B1	**13**	21.6	464	(0.09)	25.0	~400	63% H-5 (e_g) → -s; 3% s → -a; 13% H-10 ($2e_g$)→ -a; …
	15	21.9	456	(0.05)			58% H-5 (e_g) → -s; 19% s → -a; 9% s → -a …
B2	**23**	23.3	430	(0.11)	28.6	~350	40% H-10 ($2e_g$) → -s; 22% H-10 → -s; …
	26	23.9	418	(0.04)			26% H-12 → -s; 16% H-12 → -s; …
Biphenyl Nickel BiPc							
Band[a]	#[b]		**Calc[c]**		**Exp[d]**		**Wavefunction=[e]**

--	**1**	---	---	---	---	---	Ground state
Q	**3**	16.0	623	(0.47)	14.5	690	**47% a → -s; 11% a → -a; …**
	4	16.1	619	(0.65)			**62% a → -a; 27% a → -s; 4% a → -a;…**
Q	**5**	16.3	612	(0.12)			**53% a → -s; 24% a → -a; …**
	6	16.3	612	(0.49)			**57% a → -a; 36% a → -s; 3% a → -s …**
B1	**36,38**	25.4	393	(0.06)	33.3	~300	52% H-7 (a_{2u}) → -s; 6% H-7 (a_{2u}) → -s; …
B2	**39,40**	25.4	393	(0.12)			76% H-5 (e_g) → -a; 10% s → -a; …

a − Band assignment described in the text. b − The number of the state assigned in terms of ascending energy within the TD-DFT calculation. c − Calculated band energies (10^3 cm^{-1}), wavelengths (nm) and oscillator strengths in parentheses (f). d − Observed energies (10^3 cm^{-1}) and wavelengths (nm) in **Figure 3.18**. e − The wave functions based on the eigenvectors predicted by TD-DFT. One-electron transitions associated with Michl's perimeter model[121-135] are highlighted in bold. H and L refer to the HOMO and LUMO, respectively. When the H and L nomenclature is used the symmetry label for the corresponding MO in the π-systems of D_{4h} MPc complexes is provided in parentheses where applicable.

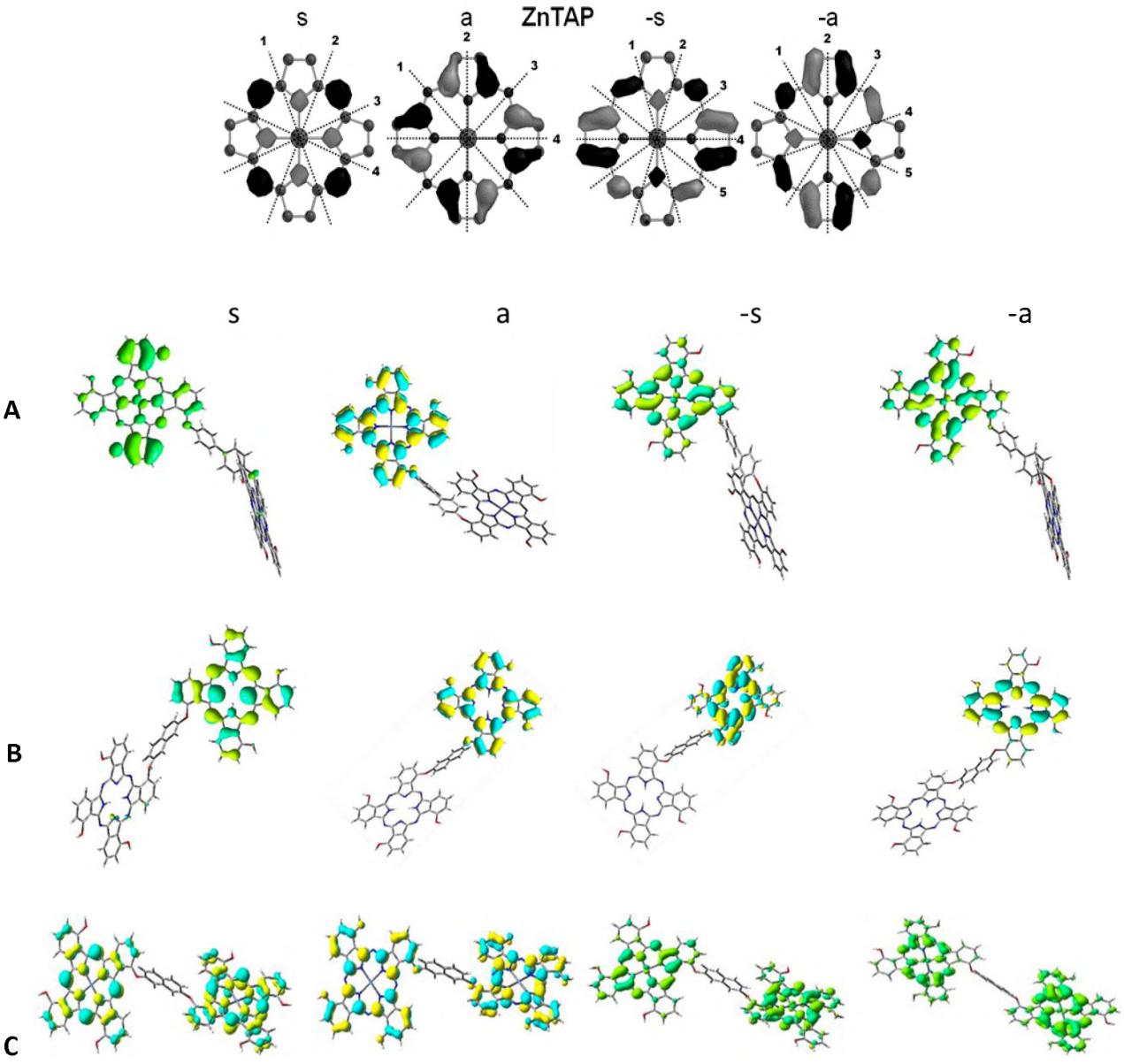

Figure 6.3: Nodal patterns of Biph-NiBiPc, Naph-H_2BiPc and Naph-NiBiPc.

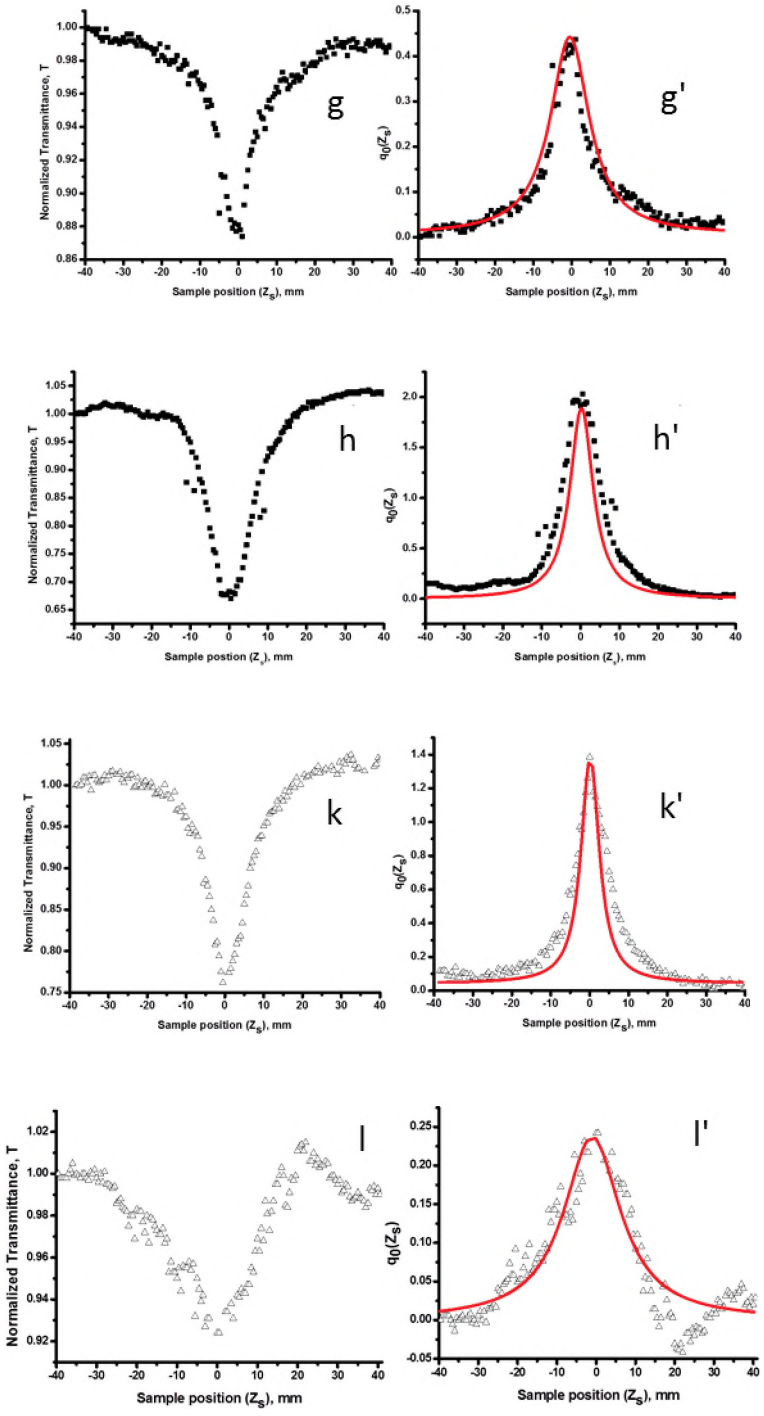

Figure 6.4: *Z*-scan and nonlinear fit curves for Biph-H_2BiPc-2 (g, g'), Biph-NiBiPc-2 (h, h') Naph-H_2BiPc-2 (k, k') and Naph-NiBiPc-2 NiBiPc (l, l') in THF solution.

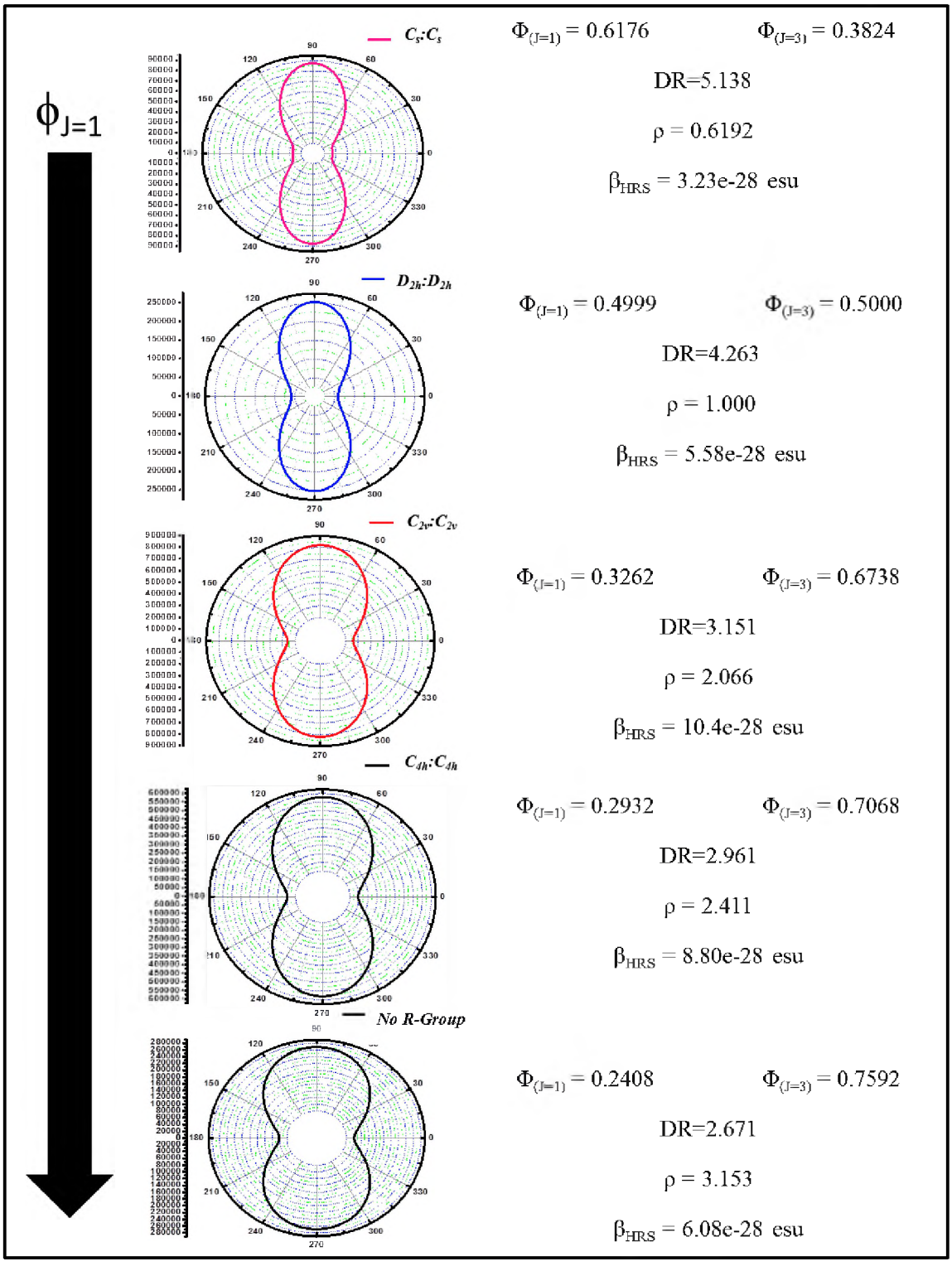

Scheme 6.1: Harmonic light intensity as a function of the polarization angle ψ by polar representation of the Biph-NiBiPcs.

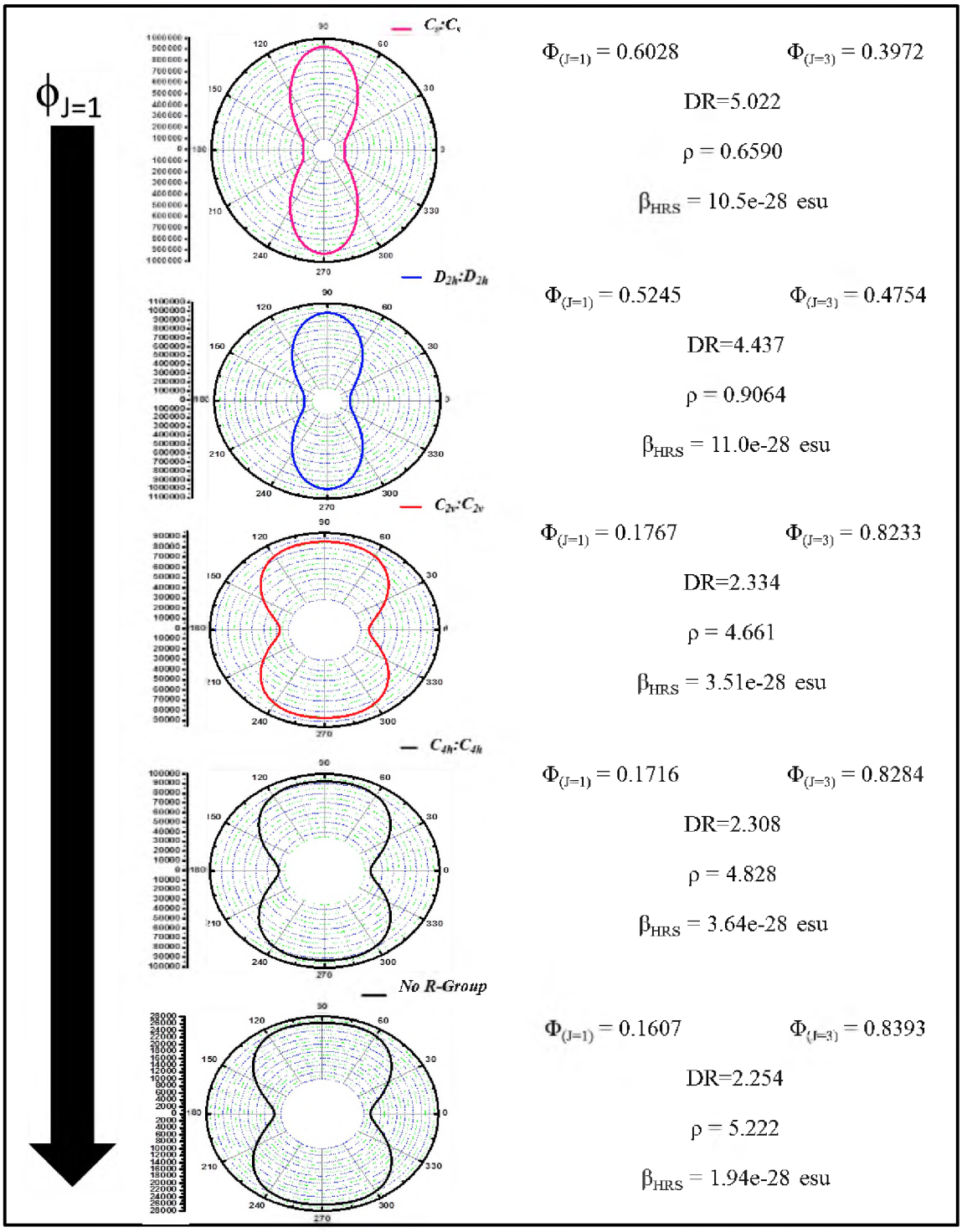

Scheme 6.2: Harmonic light intensity as a function of the polarization angle ψ by polar representation of the Naph-H_2BiPc.

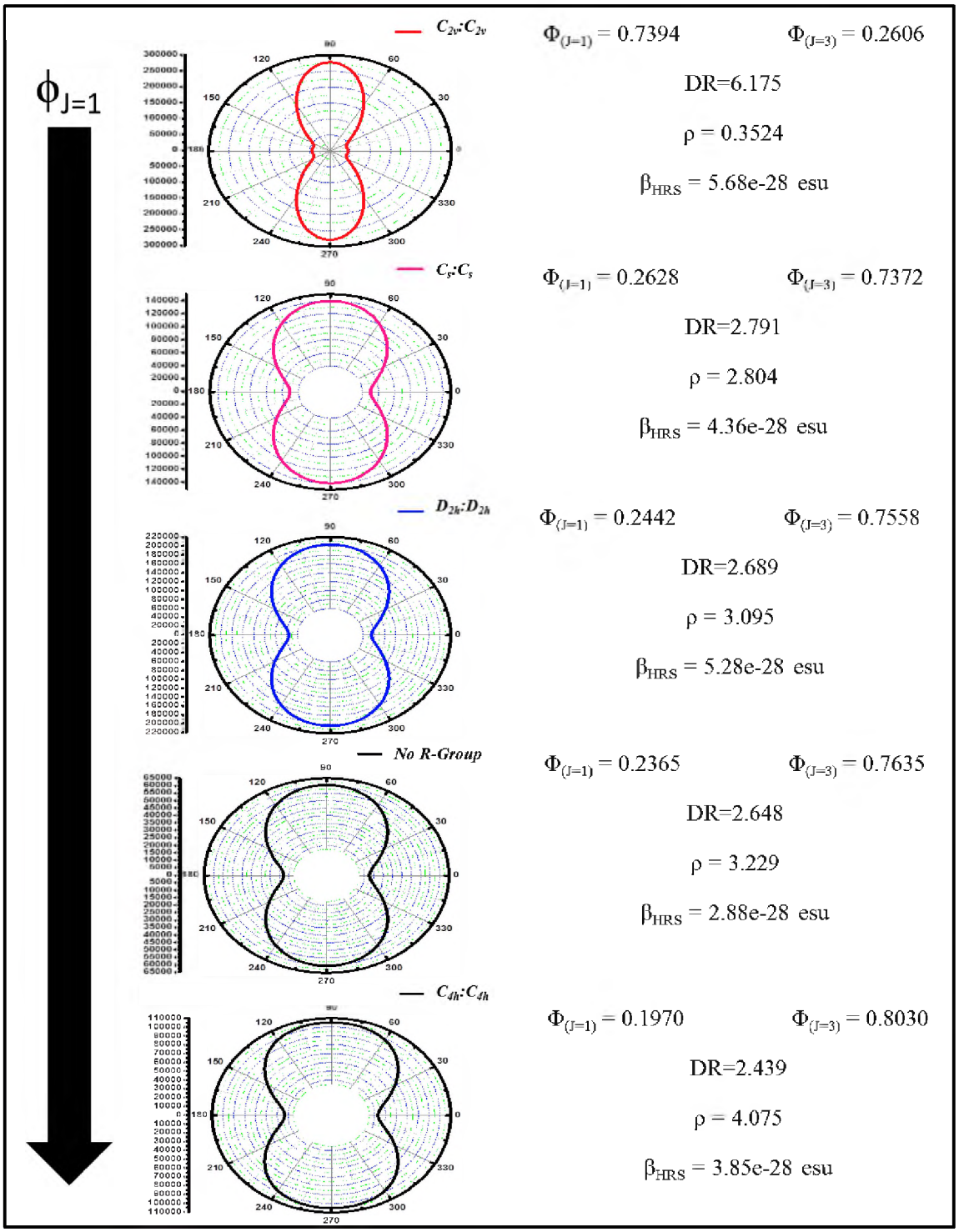

Scheme 6.3: Harmonic light intensity as a function of the polarization angle ψ by polar representation of the Naph-NiBiPcs.